UNIVERSITÀ DEGLI STUDI DI TRIESTE

XXIX CICLO DEL DOTTORATO DI RICERCA IN

NANOTECNOLOGIE

INVESTIGATION OF NANOSCALE PROPERTIES OF GRAPHENE-BASED INTERFACES FOR POSSIBLE APPLICATION IN CATALYSIS

Settore scientifico-disciplinare: FIS/03

DOTTORANDA
Naila JABEEN

COORDINATORE
Prof. ssa Lucia PASQUATO

SUPERVISORE DI TESI
Prof. Alessandro BARALDI

ANNO ACCADEMICO 2015/2016

Abstract

The focus of my research activity during three years of PhD has been on the nanoscale properties of graphene-based interfaces to grow metal or metal oxide clusters for possible application in catalysis. Graphene has emerged as most promising material since its first isolation in 2004, by A. Geim and K. Novoselov and triggered an exponentially rising interest in this topic which grew over the last decade due to the uniqueness of its properties. The most striking feature of graphene stems from its electronic band structure giving rise the high mobility of electrons plus other excellent properties like thermal and mechanical stability thus making it an attractive material for its application in catalysis.

The first part of this thesis work is devoted to investigate the growth processes of graphene on transition metal surfaces and study the interaction mechanism between graphene and the metal substrates. The primary objective of this research activity is to find the suitable metal substrate for graphene growth giving us almost free-standing graphene to study properties of metal clusters.

In recent years, great progress have been achieved in the field of supported transition metal oxide nanoclusters due to its promising application in the field clean and renewable energy sources. In this respect, the second part of this thesis work focuses on the employment of graphene/Ir(111) interface, where the moiré patterns will act as template for self-assembly of metal oxide clusters. We grew high-quality, thermally stable graphene-supported Co oxide clusters on graphene/Ir(111) interface. We studied the chemical state of the Co clusters prepared on graphene /Ir(111) using spectroscopic techniques (HR-XPS) and secondly, to understand the growth mechanism and cluster size and distribution using Low Energy Electron Microscopy. Graphene's unmatched electron mobility was further exploited with TiO_2 for inhibition of electron-hole recombination. We studied the reaction of titanium

surface with oxygen above and at the interface of graphene by following in-situ the evolution of the surface atoms using core-level photoemission spectroscopy with synchrotron radiation and demonstrate the co-existence of sub-oxide moieties along with titania. We successfully tested one of the interfaces for photocatalytic hydrogen production and found that titania-graphene is 20 times more active than titania without graphene.

Beside this, I was also involved in the investigation about the use of coronene as precursor, not only for epitaxial Gr growth, but also for the production of carbon nanoflakes which could have potential applications, especially in photocatalysis, energy conversion, and sensing. This part of the thesis is devoted to a detailed understanding of the dissociation mechanism of large molecule like coronene ($C_{24}H_{12}$) adsorbed on Ir(111) using a variety of experimental techniques, (HR-XPS, NEXAFS and ARPES).

The last part of my thesis work is dedicated to CO adsorption on Rh-nanoclusters grown on the Gr/Ir(111) interface. The natural corrugation of Gr grown on Ir(111) enables the deposited clusters to arrange themselves into extended, periodic superstructures by adsorbing at the minimum–energy sites. By means of core level photoemission and DFT calculations (carried out by theoretician at UCL), we found that the CO molecules tend to absorb at the basal cluster edges where the Rh atoms have low coordination number. We also found that at low coverages CO molecules adsorb in on top sites while at higher coverages the bridge-edges of Rh nanoclusters are the places where the adsorption of CO is preferred. This kind of studies can be exploited to the design new graphene-based materials with improve fundamental properties at nanoscale for their application in field of catalysis.

Contents

Chapter 1

Introduction

Graphene (Gr) is a two dimensional sheet of sp^2 bonded carbon based crystal as it occurs naturally in graphite. Since its first isolation in 2004, intense research on the properties of graphene was initiated using both exfoliated [1] and epitaxial [2] graphene. This work, which awarded Geim and Novoselov with Nobel prize in 2010, triggered huge interest towards this topic due to the uniqueness of graphene. The impetus in graphene research is firstly related to its structure, atomically thin layer of carbon atoms in a planar honeycomb configuration with high crystallographic quality and, when isolated from its environment, is considered free standing. The most prominent features of graphene are rooted in its electronic band structure, that can be analytically calculated in the tight binding approximation [3, 4]. The assumption is simple: the unit cell is formed by two non-equivalent atoms, and one electron per atom contributing to the π-band [3]. The π-band is of particular interest, as in free standing form the occupied (π) and unoccupied (π^*) bands touch at Fermi level E_f at the K and K$^{'}$-points of the first Brillouin zone, the so called Dirac points [5] (see Fig. 1.1). As the density of states is zero at E_f, Gr is often referred to as a 'zero gap semiconductor'. The bands show a linear dispersion around E_f so that the dispersion resembles two touching cones. They are referred to as Dirac cones and are the electronic signature feature of graphene. The behaviour close to the Fermi energy has profound effect on the physical properties of Gr, showing an anomalous quantum Hall effect [6, 7] and ballistic transport charge mobility [8, 9]. The high mobility of electron in graphene plus other excellent properties such as high thermal stability [10] and outstanding mechanical properties [11], make it an interesting material for a

number of applications like Gr based electronics [5], fuel cell [12], spintronics devices [13], and ultracapacitors [14]. Moreover, the use of Gr for transparent conducting electrodes [15, 16], to realize photosensitive transistors [17] and chemical sensors [18] is envisioned. As a consequence of exploding interest in graphene, many efforts have

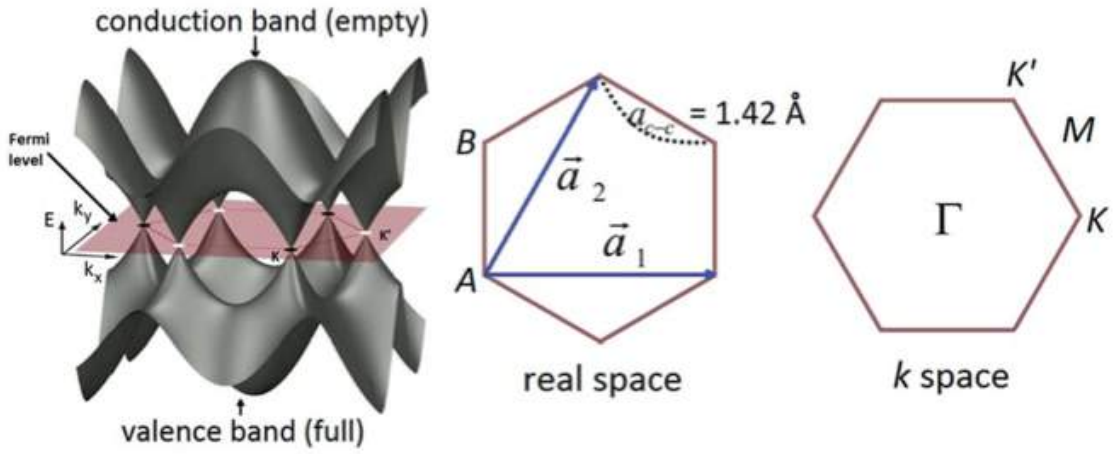

Figure 1.1: The band structure of graphene.The conduction and valence bands cross at the Dirac points K and K′-points. Adapted from [19]

been devoted to develop suitable techniques for the large scale production of high quality monolayer sheets. However, the first isolation method employed by Geim and Novoselov is not suitable for technological applications. Even though it is simple and cheap in fact the single layer thick samples are no more than an occasional occurrence among thicker ones. Therefore this method is not reliable for mass production due to its non-uniformity and lack of controllable growth parameters. Exploitation of a supporting substrate for high quality graphene turned out to be a rewarding choice for the growth of large area crystals with an enhanced stability. These growth method involves

- carbon segregation from bulk [20] by high temperature treatment.
- decomposition of carbon containing molecular precursors [21, 22] on catalytic substrates.

The most reliable method for high quality Gr growth is by means of thermal decomposition of a molecular precursor on transition metals. Two main recipes have been developed:

- Graphene can be grown on transition metal surfaces by means of Chemical Vapor Deposition (CVD) [23] of carbon containing molecules, usually hydrocarbons. The hot substrate catalyze the molecular breaking and the proper surface symmetry favours the carbon atoms in a honeycomb structure rearrangement.

- Temperature Programmed Growth (TPG) [23], the exposure to the molecular atmosphere takes place with the sample at room temperature, then the gas flow is interrupted and the sample temperature is raised.

The main advantage of these procedures is that the molecular dissociation occurs selectively on the bare metallic surfaces, not on the already formed Gr patches. Therefore the growth is self-limiting, thus avoiding the formation of multi-layers. For this reason epitaxy appears to be the route of choice for fabrication of large Gr sheets.

The aim of this thesis was to investigate the nanoscale properties of Gr-based interfaces which could find applications in catalysis. A good understanding of the interactions between graphene and substrates is very important to grow small metallic or oxide clusters at their interface. These small clusters, comprising a few hundred atoms, behave as a distinct state of matter, differing in many aspects from bulk matter of the same material and can be used for technological applications in the field of catalysis

In this scenario, if Gr was grown on the strongly interacting metal substrate, then these metal surfaces will also interact strongly with clusters grown on top of Gr which makes them lose their individual character. For this reason, a deeper understanding of graphene structural, chemical and physical properties, together with its interactions on different substrates and different chemical species, is needed. The interaction between epitaxial graphene and transition metal (TM) substrates is highly dependent upon the choice of TM substrate. It is also well known that, due to the lattice mismatch with the substrate, Gr can form large periodicity superstructures, called moiré pattern [24, 25]. Further, these interaction with the substrate can cause corrugations, with weakly interacting regions of Gr far from the surface and strongly interacting regions close to the surface [22, 26]. These interactions between Gr-metal surfaces causes modifications of the properties that make it unique, mainly because of charge transfer, rehybridization and changes to its band structure [27, 28, 29]. So, it is highly desirable to find a suitable metal substrate for Gr-growth giving us almost

a free-standing graphene for the investigation of cluster properties in surface science experiments.

After the introduction and the discussion of experimental techniques, the third chapter of my thesis has been devoted to describe the interaction of graphene on different metal substrates. In order to find suitable metal substrates for Gr-growth, we investigated the growth of graphene ranging from highly interacting metals, such as Ru [24], to less interacting metals *i.e.* Ir [30]. The ultimate goal of the experiment was therefore two-fold: on one hand we wanted to distinguish the contribution arising from the geometrical and chemical properties of the surface on the interaction between graphene and metals and therefore to understand the nature of this interaction, which would make it possible to tailor the properties of supported graphene to suit well for the needs of the surfaces and interfaces in catalysis; on the other we wanted to verify the possibility of using high resolution core level photoelectron spectroscopy as an experimental technique capable to probe the properties of differently interacting graphene-metal interfaces. This has been achieved through the intercalation of a variety of metallic species at the interface between graphene and its substrate: intercalation, in fact, modifies the chemical properties and electronic structure of the substrate while preserving its geometry, provided the intercalated layer is of monoatomic thickness. Intercalation is also a promising technique to overcome the main limitation of the CVD growth method, *i.e.* the impossibility to grow graphene directly on some metal surfaces. In those cases, graphene has to be transferred from one surface to the other through a mechanical or chemical process, which could potentially introduces defects and contaminants. Moreover, through intercalation we can substitute the interlayer material between Gr and the substrate while preserving the high quality of CVD graphene. Our experimental findings were completed by a set of theoretical simulations carried out by the group of Prof. Alfè from the University College London. This study further investigates the possibilities for the synthesis of innovative interfaces between whatever metal and high quality layer of graphene. Eventually we conclude that the most suitable TM-substrate to study the properties of clusters on graphene is the Gr/Ir(111) interface, due to the corrugation of the carbon layer and its very weak interaction with the substrate.

The outstanding structural and electronic properties of graphene are important tools to design smarter and more efficient graphene-based photocatalysts. The unique characteristic of Gr on Ir(111) system have been exploited in the fourth chapter. In fact the Gr/Ir(111) interface provide a versatile template for the growth of cluster lattices of unmatched quality [31]. An efficient catalytic material is often supported [32], but the reactivity of the catalyst can be influenced by their support. Graphene supported on lattice-mismatch metal substrates is considered an interesting support for clusters to be used in electrochemistry or photochemistry. Moiré patterns act as template for self-assembly of metal clusters, the perfection of cluster lattice strongly depending on the metal supporting the Gr-film [26]. So the Gr/Ir(111) is the perfect choice for cluster production with exceptional order and narrow size distribution, which makes it an attractive candidate for application in catalysis. The clusters of transition metal oxides have received much attention as photocatalyst, electrocatalyst and interlayer materials in energy conversion devices, especially because of their stability, controllable band gap and charge carrier properties [33].

In this respect the fourth chapter is devoted to investigate the nanoclusters of transition metal oxides specifically low cost which could potentially form the basis of clean and renewable source of energy. For example, CoO nanoparticles can decompose pure water under visible-light irradiation without any co-catalysts or sacrificial reagents [34]. Owing to quantum confinement, typical nanostructured materials presents a larger bandgaps than the corresponding bulk materials. As a result, the absolute potentials of conduction and valence-band edges have to be adjusted. Surface states or morphology of nanostructures can also affect the band-edge positions of the material [35]. As shown in the energy diagram in Fig. 1.2, a qualitative difference exists between nanocrystals and micropowders in their band-edge positions with regard to water redox potentials [34]. This is also in good agreement with previous theoretical calculations: the edge position of the conduction band of CoO micropowders is located below the hydrogen-evolution potential, which indicates why the powders are not photocatalytically active for water splitting. This band alignment of CoO nanocrystals with water redox potentials explains why nanocrystals have significantly different photocatalytic activity with respect to those of micropowders and satisfies the necessary requirement for overall water splitting

[34].

For these reasons a highly active water-splitting particulate system requires an intimate integration of a suitable candidate with separate hydrogen and oxygen-evolution co-catalysts [36, 37]. Such structures can reduce the water-splitting back-reaction and take advantage of the unique catalytic and optical properties of individual components of the system [34]. To obtain the best possible positions with respect to water redox potentials, we grew high-quality, thermally stable graphene-supported Co-oxide clusters on Gr/Ir(111) interface. We studied the relationship between their structural and chemical properties since they can have attractive applications as catalytic material in energy harvesting and storage devices. Our goal

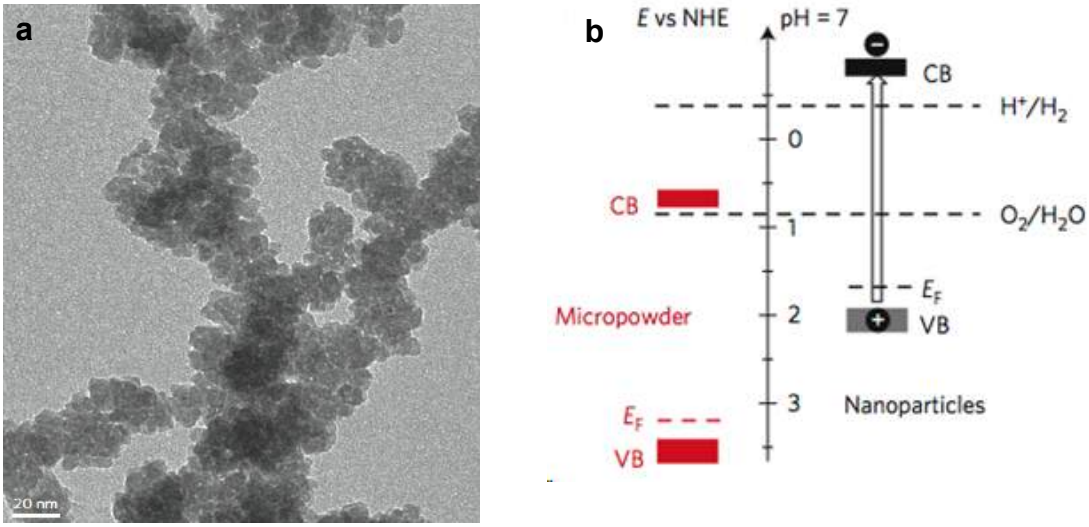

Figure 1.2: (a) Transmission electron micrograph of CoO nanoparticles; (b) Band positions of CoO nanocrystals and micropowders. Adapted from [34].

was two-fold: firstly, to explore the chemical state (form its metallic state up to full oxide state) of the Co clusters prepared on Graphene/Ir(111) using spectroscopic techniques (High-Resolution XPS) and secondly, to understand the growth mechanism and cluster distribution using Low Energy Electron Microscopy (LEEM). LEEM, in fact, allows direct, real-space imaging of the sample morphology over large surface areas (up to several tens of micrometers), with a lateral resolution of 10 nm and exceptional structural and surface sensitivity. These measurements showed that, in fact we produced highly dispersed small and stable clusters on Gr/Ir(111) interface which could have application as a catalytic material in renewable energy production.

Beside Co-oxide growth on Gr/Ir(111) interface, we also focused on detailed understanding of fundamental aspects of Gr-Titania interfaces in this chapter. This knowledge can have potential impact on several technological applications, including solar cells, photocatalysis for H_2 production [38, 39] and heterogeneous catalysis [40]. We believe that these studies can help to improve materials properties and device performances. The interaction of water with TiO_2 for hydrogen production as a catalytic material is a key prospect for conversion of solar energy to chemical energy [39]. TiO_2 alone has low activity towards photocatalytic water splitting due to the electron-hole recombination, therefore carefully designed systems are needed in order to effectively separate the photo generated electrons and holes. Graphene can provide unmatched electron mobility which improves both, charge transfer plus inhibit electron-hole recombination. To exploit all these properties we have grown high-quality and thermally stable graphene-titania interfaces. We adopted the strategy of growing titania clusters and thin films above the corrugated graphene layer prepared on Ir(111), at the interface and in both configurations. A detailed description of titania clusters, intercalation and oxide formation was successfully determined by following in-situ the evolution of the surface atoms using core-level photoemission spectroscopy with synchrotron radiation. This study allows us to understand the reaction of titanium surface with oxygen above and at the interface of graphene and demonstrate the co-existence of sub-oxide moieties along with titania. The Gr sheets can anchor TiO_2 nanoclusters thus allowing charge transfer within the Gr-Titania interface. This sandwich architecture can be used to design more efficient metal-oxide graphene based photocatalyst in which Gr will act as a buffer layer to enhance the photocatalytic reactivity through charge separation. This system was successfully tested for photocatalytic measurements. The titania-Gr interface is 20 times more active than titania without Gr for photocatalytic hydrogen generation. So, Gr is playing its role as buffer layer toward clean H_2 production with improved electron-hole separation.

Since Gr isolation, research has broaden to a wider set of graphene related systems in order to exploit its electronic properties also in the field of nano-catalysis. For this, Gr nanoribbons and nanographene proved to be very effective [41]. As discussed earlier, band gap problems in Gr can be overcome by exploiting quantum

confinement effects, which allow for modification of the band gap by adjusting the width and type of edge terminations. The large number of available precursors is the key for the growth of Gr nanoribbons and nanoflakes via polymerization reactions using a bottom-up approach [42, 43, 44]. The fifth chapter of my thesis is devoted to the description of the dehydrogenation mechanism of coronene on Ir(111), up to the formation of dome-shaped Gr-nanoflakes using a combined experimental and theoretical study. The coronene molecules adsorbed on Ir(111) undergo major conformational changes during dissociation process, which brings molecules from a flat, slightly upward pointing bowl shape to graphene through a series of exotic configurations. By exploiting this reaction mechanism, we contemplate the possibilities of creating controlled arrangements of Gr nanoislands and functionalizing them by encapsulating single adatoms below the carbon dome. These systems provides opportunities for the development of the state-of-the-art new materials in the field of catalysis where the configuration (tilting, bending, or curling) of a molecule plays a key role in its reactivity. For example, chemoselective hydrogenation of α, β -unsaturated carbonyl compounds to form unsaturated alcohols [45]. This chemoselective hydrogenation otherwise requires a suitable catalyst to trigger the kinetics of the reaction, however tilted configuration of C=C brings change in the chemistry of molecule, thus inhibiting its further reaction [45]. So, such molecular configurations are key to success of many other catalytic systems of fundamental interest and practical importance, and could be similarly investigated.

One of the most fascinating aspects of the nanoclusters for the scientific community working in nanotechnolgy is that these systems represent an intermediate state of matter between single atoms and bulk materials. Because of their small size nanoclusters often present high reactivity and for this reason can find application in heterogeneous catalysis, such as in the case of Au [40] and Pt [46]. An increased catalytic activity of these system is frequently interpreted in terms of low atomic coordination number (C_N) with high density of corner and edges atoms [47]. Previous findings of our research group [48], have shown how it is possible to achieve a controllable morphology and structural order of Rh clusters grown on Gr/Ir(111) morié superstructure. This studies showed how the cluster size influences the properties of surface atom just by small changes at interatomic distances. It has

been proved that the smaller clusters are morphologically disordered and lack a clear layered structures while on other hand larger clusters formed of several tens of atoms form regular truncated octahedral structures with (111) and (100) nanofacets [49]. Starting from this knowledge, we studied the adsorption of CO on these Rh nanoclusters in last chapter and relate them with what previously known in literature for Rh(111) [50, 51] and Rh(100) [52]. The situation is more complex, although it is still possible to identify some similar trends of CO adsorption on Rh single crystals in low coverages range [50, 51, 52]. It is important to notice that the Gr is largely unaffected by CO adsorption on the supported Rh nanoclusters. This finding implies that CO does not dissociate at temperature important for catalysis. In order to clarify these issues and to get an atomistic insight into the mechanisms of CO adsorption on the Rh nanoclusters, a series of DFT calculations have been carried out by our theoretician colleagues at the UCL. It is now experimentally plus theoretically determined that CO molecules tend to adsorb at the basal cluster edges where Rh atoms have a lower coordination number. Top sites are preferred at low coverages while at higher coverages CO molecules also tend to adsorb in bridge-edge sites. Only at very high coverages the CO molecules get adsorbed on the nanoclusters facets.

Bibliography

[1] K. S. Novoselov, A. K. Geim, S. V. Morozov, D. Jiang, Y. Zhang, S. V. Dubonos, , I. V. Grigorieva, and A. A. Firsov. *Electric field effect in atomically thin carbon films.* Science, 306:666–669, 2004.

[2] C. Berger , Z. Song , T. Li, X. Li , A. Y. Ogbazghi, R. Feng, Z. Dai, A. Marchenkov, E. H. Conrad, P. N. First, and Y. A. de Heer. *Ultra-thin epitaxial graphite: 2D electron gas properties and a route toward graphene-based nanoelectronics.* Journal of Physical Chemistry B, 108:19912, 2004.

[3] P. R. Wallace. *The Band Theory of Graphite.* Physics Reviews, 71:622, 1947.

[4] C. Bena, and G. Montambaux. *Remarks on the tight-binding model of graphene.* New Journal of Physics, 11:095003, 2009.

[5] A. H. Castro, N. Neto, M. R. Peres, K. S. Novoselov, and A. K. Geim. *The Electronic Properties of Graphene.* Reviews of Modern Physics, 81:109, 2009.

[6] V. P. Gusynin, and S. G. Sharapov. *Unconventional integer quantum Hall effect in graphene.* Physics Review Letters, 95(14):146801, 2005.

[7] Y. Zhang, Y. W. Tan, H. L. Stormer, and Ph. Kim. *Experimental observation of the quantum Hall effect and Berry's phase in graphene.* Nature, 438(7065):201–204, 2005.

[8] A. S. Mayorov, R. V. Gorbachev, S. V. Morozov, L. Britnell, R. Jalil, L. A. Ponomarenko, P. Blake, K. S. Novoselov, K. Watanabe, T. Taniguchi, and A. K. Geim. *Micrometer-scale ballistic transport in encapsulated graphene at room temperature.* Nano Letters, 11(6):2396–2399, 2011.

[9] X. Du, I. Skachko, A. Barker, and E. Y. Andrei. *Approaching ballistic transport in suspended graphene.* Nature Nanotechnology, 3(8):491–495, 2008.

[10] A. A. Balandin, S. Ghosh, W. Bao, I. Calizo, D. Teweldebrhan, F. Miao, and C. N. Lau. *Superior thermal conductivity of single-layer graphene.* Nano Letters, 8(3):902–907, 2008.

[11] C. Lee, X. Wei, J. W. Kysar, and J. Hone. *Measurement of the elastic properties and intrinsic strength of monolayer graphene.* Science, 321(5887):385–388, 2008.

[12] L. Qu, Y. Liu, J. B. Baek, and L. Dai. *Nitrogen-doped graphene as efficient metal-free electrocatalyst for oxygen reduction in fuel cells.* ACS Nano, 4(3):1321–1326, 2010.

[13] W. Han, R. K. Kawakami, M. Gmitra, and J. Fabian. *Graphene spintronics.* Nature Nanotechnology, 9(10):794–807, 2014.

[14] M. D. Stoller, S. Park, Y. Zhu , J. An, and R. S. Ruoff. *Graphene-Based Ultracapacitors.* Nano Letters, 8:3498, 2008.

[15] A. Reina, X. Jia, J. Ho, D. Nezich, H. Son, V. Bulovic, M. S. Dresselhaus, and J. Kong. *Large Area, Few-Layer Graphene Films on Arbitrary Substrates by Chemical Vapor Deposition.* Nano Letters, 9 (1):30, 2009.

[16] K. S. Kim, Y. Zhao, H. Jang, S. Y. Lee, J. M. Kim, K. S. Kim, J. H. Ahn , P. Kim, J. Y. Choi, and B. H. Hong. *Large-scale pattern growth of graphene films for stretchable transparent electrodes.* Nature, 457:706, 2009.

[17] F. Xia, T. Mueller, R. Golizadeh-Mojarad, M. Freitag, Y. M. Lin, J. Tsang, V. Perebeinos, and P. Avouris. *Photocurrent Imaging and Efficient Photon Detection in a Graphene Transistor.* Nano Letters, 9:1039, 2009.

[18] Y. Dan, Y. Lu, N. J. Kybert, Z. Luo, and A. T. Johnson. *Intrinsic Response of Graphene Vapor Sensors.* Nano Letters, 9:1472, 2009.

[19] E. Y. Andrei, G. Li, and X. Du. *Electronic properties of graphene: a perspective from scanning tunneling microscopy and magnetotransport.* Reports on Progress in Physics, 75:056501, 2012.

[20] N. Liu, L. Fu, B. Dai, K.Yan, X. Liu, R. Zhao , Y. Zhang, and Z. Liu. *Universal segregation growth approach to wafer-size graphene from non-noble metals.* Nano Letters, 11:297–303, 2011.

[21] I. Pletikosic, M. Kralj, P. Pervan, R. Brako, J. Coraux, A. T. N'Diaye , C. Busse, and T. Michely. *Dirac Cones and Minigaps for Graphene on Ir(111).* Physical Review Letters, 102:1–4, 2009.

[22] A. B. Preobrajenski, M. L. Ng, A. S. Vinogradov, and N. Mårtensson. *Controlling graphene corrugation on lattice-mismatched substrates.* Physical Review B, 78:073401, 2008.

[23] J. Coraux, A. T. N'Diaye,M. Engler, C. Busse, D. Wall, N. Buckanie, F. J. Meyer zu Heringdorf, R. van Gastel, B. Poelsema, and T. Michely. *Growth of graphene on Ir(111).* New Journal of Physics, 11:023006, 2009.

[24] P. W. Sutter, J. I. Flege, and E. A. Sutter. *Epitaxial graphene on ruthenium.* Nature Materials, 7(5):406–411, 2008.

[25] C. Busse, P. Lazić R. Djemour, J. Coraux, T. Gerber, N. Atodiresei, V. Caciuc, R. Brako, A. T. N'Diaye, S. Blügel, J. Zegenhagen, and T. Michely. *Graphene on Ir(111): physisorption with chemical modulation.* Physical Review Letters, 107(3):036101, 2011.

[26] M. Batzill. *The Surface Science of Graphene: Metal Interfaces, CVD Synthesis, Nanoribbons, Chemical Modifications, and Defects.* Surface Science Reports, 67:83, 2012.

[27] G. Giovannetti, P. Khomyakov, G. Brocks, V. Karpan, J. Van Den Brink, and P. Kelly. *Doping graphene with metal contacts.* Physical Review Letters, 101(2):026803, 2008.

[28] A. Varykhalov, M. Scholz, T. Kim, and O. Rader. *Effect of noble-metal contacts on doping and band gap of graphene.* Physical Review B, 82(12):121101, 2010.

[29] B. Schultz, C. Jaye, P. Lysaght, D. Fische, D. Prendergast, and S. Banerjee. *On chemical bonding and electronic structure of graphene–metal contacts.* Chemical Science, 4(1):494–502, 2013.

[30] A. T. N'Diaye, J. Coraux, T. N. Plasa, C. Busse, and T. Michely. *Structure of epitaxial graphene on Ir(111).* New Journal of Physics, 10:043033, 2008.

[31] A. T. N'Diaye, T. Gerber, C. Busse, J. Myslivecek, J. Coraux, T. Michely. *A Versatile Fabrication Method for Cluster Superlattices.* New Journal of Physics, 11:103045, 2009.

[32] C. R. Henry. *Surface Studies of Supported Model Catalysts.* Surface Science Reports, 31:231, 1998.

[33] M. C. Torker, and E. A. Carter. *Transition Metal Oxide Alloys as potential solar Energy Conversion Materials.* Journal of Material Chemistry A, 1:2474-2484, 2013.

[34] L. Liao, Q. Zhang, Z. Su, Z. Zhao, Y. Wang, Y. Li, X. Lu, D.Wei, G. Feng, Q. Yu, X. Cai, J. Zhao, Z. Ren, H. Fang, F. Robles-Hernandez, S. Baldelli, and J. Bao. *Efficient solar water-splitting using a nanocrystalline CoO photocatalyst.* Nature Nanotechnology, 9:69-73, 2014.

[35] J. Jasieniak, M. Califano, and S. E. Watkins. *Size-dependent valence and conduction band-edge energies of semiconductor nanocrystals.* ACS Nano, 5:5888–5902, 2011.

[36] X. Chen, S. H. Shen, L. J. Guo, and S. S. Mao. *Semiconductor-based photocatalytic hydrogen generation.* Chemical Reviews, 110:6503–6570, 2010.

[37] A. Kudo, and Y. Miseki. *Heterogeneous photocatalyst materials for water splitting.* Chemical Society Reviews, 38:253–278, 2009.

[38] S. Liu, and Y. J. Xu. *Photo-induced transformation process at gold clusters-semiconductor interface: Implications for the complexity of gold clusters-based photocatalysis.* Scientific Reports, 6:22742, 2016.

[39] M. Ni, M. K. H. Leung, D. Y. C. Leung, and K. Sumathy. *A review and recent developments in photocatalytic water-splitting using TiO_2 for hydrogen production.* Renewable and Sustainable Energy Reviews, 11:401, 2007.

[40] C. T. Campbell. *The active site in nanoparticle gold catalysis.* Science, 306:234, 2004.

[41] Y. W. Son, M. L. Cohen, and S. G. Louie. *Energy gaps in graphene nanoribbons.* Physical Review Letters, 97(21):216803, 2006.

[42] L. Talirz, H. Söde, J. Cai, P. Ruffieux, S. Blankenburg, R. Jafaar, R. Berger, X. Feng, K. Müllen, D. Passerone, R. Fasel, and C. A. Pignedoli. *Termini of bottom-up fabricated graphene nanoribbons.* Journal of the American Chemical Society, 135(6):2060–2063, 2013.

[43] J. Cai, P. Ruffieux, R. Jaafar, M. Bieri, T. Braun, S. Blankenburg, M. Muoth, A. P. Seitsonen, M. Saleh, X. Feng, K. Müllen, and R. Fasel. *Atomically precise bottom-up fabrication of graphene nanoribbons.* Nature, 466(7305):470–473, 2010.

[44] M. Treier, C. A. Pignedoli, T. Laino, R. Rieger, K. Müllen, D. Passerone, and R. Fasel. *Surface-assisted cyclodehydrogenation provides a synthetic route towards easily processable and chemically tailored nanographenes.* Nature Chemistry, 3(1):61–67, 2011.

[45] M. E. Chiu, D. J. Watson, G. Kyriakou, M. S. Tikhov, and R. M. Lambert. *Tilt the Molecule and Change the Chemistry: Mechanism of S-Promoted Chemoselective Catalytic Hydrogenation of Crotonaldehyde on Cu(111).* Angewandte Chemie, 118:7692–7696, 2006.

[46] S. Vajda, M. J. Pellin, J. P. Greeley, C. L. Marshall, L. A. Curtiss, G. A. Ballentine, J. W. Elam, S. Catillon-Mucherie, P. C. Redfern, F. Mehmood, and P. Zapol. *Subnanometre platinum clusters as highly active and selective catalysts for the oxidative dehydrogenation of propane.* Nature Materials, 8:213, 2009.

[47] S. Rusponi, T. Cren, N. Weiss, M. Epple, P. Buluschek, L. Claude, and H. Brune. *The remarkable difference between surface and step atoms in the magnetic anisotropy of two-dimensional nanostructures.* Nature Materials, 2:546, 2003.

[48] A. Cavallin, M. Pozzo, C. Africh, A. Baraldi, E. Vesselli, C. Dri, G. Comelli, R. Larciprete, P. Lacovig, S. Lizzit, and D. Alfè. *Local electronic structure and density of edge and facet atoms at Rh nano-clusters self-assembled on a graphene template.* ACS Nano, 6:3034, 2012.

[49] G. Wulff. Zur Frage der Geschwindigkeit des Wachsthums und der Auflosung der Krystallflachen. Zeitschrift für Krystallographie und Mineralogie, 34:449, 1901.

[50] A. Beutler, E. Lundgren, R. Nyholm, J. N. Andersen, B. Setlik, and D. Heskett. *On the adsorption sites for CO on the Rh(111) single crystal surface.* Surface Science, 371:381, 1997.

[51] A. Beutler, E. Lundgren, R. Nyholm, J. N. Andersen, B. J. Setlik, and D. Heskett. *Coverage and temperature-dependent site occupancy of carbon monoxide on Rh(111) studied by high-resolution core-level photoemission.* Surface Science, 396:117, 1998.

[52] F. Strisland, A. Ramstad, T. Ramsvik, and A. Borg. *CO adsorption on the Rh(100) surface studied by high resolution photoelectron spectroscopy.* Surface Science, 415:1020, 1998.

Chapter 2

Experimental techniques and setups

This chapter gives a short introduction to the principles of the experimental techniques exploited to carry on my doctoral research activity, together with the basic description of the experimental facilities and instrumentation being used to acquire the data presented. I describe briefly the preliminary considerations on surface science studies, experimental conditions and workstations, sample preparation and analysis methods used in the present work. All the experimental techniques, I have used during my PhD research activity, require Ultra High Vacuum (UHV) conditions with a base pressure of the order of 10^{-10} - 10^{-11} mbar. An UHV environment, in surface science experiments plays major role: firstly, make it possible to prepare atomically clean surfaces and maintain it for the duration of the experiment. If we assume that the sticking probability of contaminants in a vacuum environment is 1, then it will take a few seconds to cover a surface at a background pressure of 10^{-6} mbar [1]. Secondly, good pressure conditions are also needed when working with low energy electrons (typically from 40 to 300 eV) based techniques, in order to minimizes the scattering effects due to the residual gas molecules. Such a low pressure can be achieved through a combination of special materials, good pumping speed and baking of the experimental chamber, in order to induce desorption of water along with other contaminants from the inner walls of the chamber.

2.1 Sample preparation

The metallic surfaces like the one used in this work (Ru(0001) and Ir(111)) were treated through suitable procedures in order to get atomically clean. The cleaning procedure typically consists of sputtering cycles, followed by annealing to high temperature. During sputtering, the sample surface is bombarded by a collimated flux of energetic Ar ions in such a way to remove the contaminants from the very first layers by ion impact, resulting in a rough and disordered surface. This can be amended by annealing to high temperature to restore surface long-range order. The cleaning procedure is repeated until no contaminations can be detected using XPS technique (detection limit being 0.1 % ML).

The experimental data presented and discussed in this thesis were acquired at different experimental end-stations, equipped with a multi-stage pumping system, the instrumentation typically required to clean and prepare the sample and a gas line for gas inlet into the chamber. In order to fully understand the systems presented in this thesis, several aspects need to be addressed. For example, the core level photoemission spectroscopy along with absorption spectroscopy and angle resolved photoemission spectroscopy were used to probe electronic configuration to investigate the chemical composition of the systems. On the other hand, electron based microscopic and diffraction techniques allow us to access surface structure and morphology. In some of experimental data, the experiments were complemented by DFT theoretical simulations. The main technique used to characterize the different nanoclusters from its metallic state to full oxidation state was achieved by photoelectron spectroscopy both using lab based source (in Surface Science Laboratory at Elettra) and synchrotron radiation (SuperESCA beamline of Elettra). The following sections will briefly introduce the experimental techniques that were used in this work.

2.2 The Surface Science Laboratory

The Surface Science Laboratory (SSL) is jointly established by the Department of Physics of the University of Trieste and Elettra Sincrotrone Trieste. In SSL we prepared all the samples and optimized the conditions before taking them to beamline

and also for photocatalytic measurements. The experimental chamber is equipped

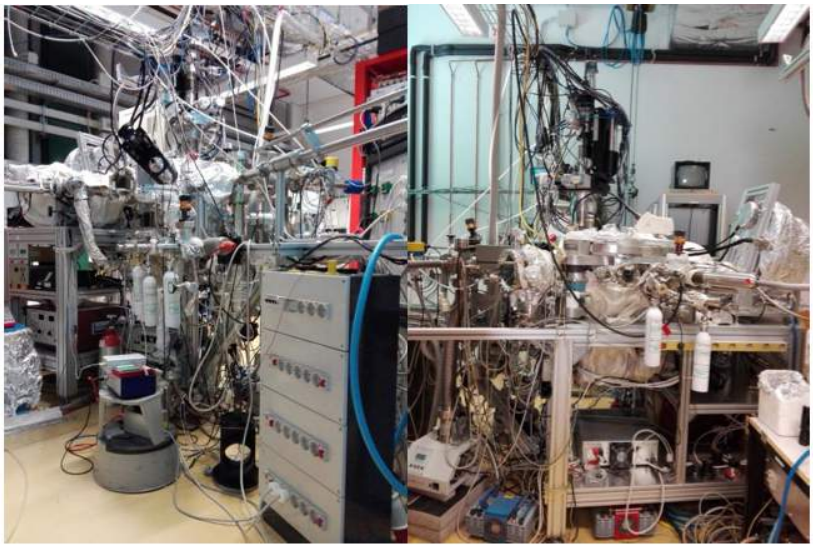

Figure 2.1: The experimental chamber of the Surface Science Laboratory at Elettra.

with a variety of instruments primarily devoted to low energy electron diffraction, temperature programmed desorption and photoemission experiments. Low energy electron diffraction is carried out with a VG rear view electron optical system and the diffraction patterns are collected with a CCD camera. SPA-LEED measurements are performed using another instrument and a custom written acquisition software. The experimental chamber (as shown in Fig. 2.1) is also equipped with two conventional monochromatic X-ray sources, *Mg-Kα* and *Al-Kα* for photoemission experiments. The *Mg-Kα* X-ray source ($h\nu$=1253.6 eV, and ΔE = 0.9 eV) and the monochromatic *Mg-Kα* source ($h\nu$=1486.6 eV, and ΔE = 0.4 eV) are used in combination with an hemispherical electron energy analyzer (mean radius 150 mm). Further, a residual gas analyzer for Temperature Programmed Desorption measurements is also available with the particular sample mounting. Beside this, the UHV chamber has a five degree of freedom manipulator (three translational axes, polar and azimuthal rotation) mounted on automated flange, that allow sample movement via a software interface. So, different instruments can be mounted on the radially distributed flanges of the chamber.

2.3 Photoelectron spectroscopy

Photoelectron spectroscopy is an experimental technique based on photoelectric effect that takes place when a photon with a sufficient energy interacts with matter, probing the occupied electronic levels. This process, which was discovered experimentally by Hertz in 1887 [2], takes place when a material is exposed to electromagnatic radiation and emits electrons (photoelectrons). In 1905 [3] Einstein explained the effect by treating light as massless particles (photons) with a precise energy and by proposing that a minimum energy is required to make an electron escape from a solid. This threshold energy depends on the material and is given by

$$E_{min} = h\upsilon_{min} = \Phi \tag{2.1}$$

where h is Plank's constant, υ is the frequency of the incident photons and Φ is the work function for the given material.

Kai Siegbahn and his co-workers in Uppsala developed the technique in 1960's, today known as photoelectron spectroscopy [4]. Due to its chemical specificity, it was originally named as Electron Spectroscopy for Chemical Analysis (ESCA). This technique provides information on the atomic composition of a sample as well as the chemical states and electronic structure of the observed atoms. Since the introduction of soft X-ray synchrotron radiation sources, PES has become one of the major techniques for studying surfaces, interfaces and thin films [5].

2.3.1 The principles of photoelectron spectroscopy

When a sample is irradiated by light, photons can interact and transfer energy to electrons, so that if the energy is greater than work function of the material the electrons may leave the surface through a process illustrated in Fig. 2.2. Since the total energy is conserved, the process can be described as follow:

$$E_i + h\upsilon = E_f + E_{kin} \tag{2.2}$$

where $h\upsilon$ is the energy of the incoming photons, E_i and E_f are the initial and final states of energy and E_{kin} is the kinetic energy of the emitted photoelectrons. The binding energy (BE) of the electron E_B is given by the difference between the total

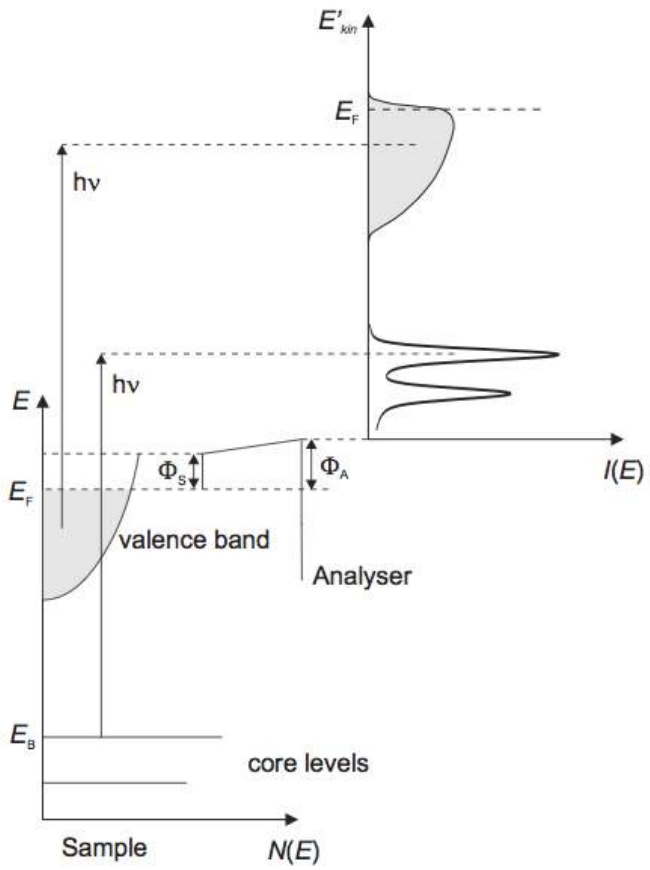

Figure 2.2: Illustration of the photoelectron spectroscopy principle. Adapted from [6].

energy of the initial and final states.

$$E_B = E_f - E_i = hv - E_{kin} \tag{2.3}$$

If the energy of the incoming photons is hv>E_B+Φ_S where Φ_S is the work function of the sample then the electrons with BE E_B can be excited above the vacuum level. In the photoemission process, the kinetic energy of photoelectron is measured and then the binding energy is calculated. This requires fixing a proper energy reference. In all the spectra reported in this thesis, the binding energies are referenced with respect to the Fermi level. So, the BE can be calculated through the kinetic energy of the photoelectrons measured by means of an electron energy analyzer.

$$E_B = hv - E'_{kin} - \Phi_A \tag{2.4}$$

Here, E'_{kin} is the kinetic energy of the photoelectron measured by analyzer and Φ_A is the work function of the analyzer. In order to properly reference binding energy scale to the Fermi level, it is sufficient to know the work function of electron analyzer.

2.3.2 Core level binding energies and core level shifts

Core levels are localized electronic states that don't participate in chemical bonding [7]. Photoelectron spectroscopy is an ideal tool to characterize materials due to the specific E_B of each element. The electron emitted from different chemical environment will have slightly different energy and core level peaks in the PE spectrum will appear with slightly different binding energies. These shifts are reflected in the so called chemical shifts [8]. The core level shifts (CLS) can provide information on how atoms are chemically bonded in a system. Moreover, this can be used as fingerprints to identify atoms or molecules in different chemical environment. This can be related also to the reduced coordination of the surface atoms of the material. The magnitude and the direction of the surface core level shift depend upon the difference in cohesive energies between initial and final states of the bulk and surface atoms due to the different coordination. Both the initial and final state effects contribute to the observed binding energy as it can be seen in Eq. 2.3. For complete analysis of the core level shifts, as those studied in this thesis, it is important to include final state effects in the theoretical calculations since they impact significantly the measured binding energy [7].

2.3.3 Surface sensitivity of photoelectron spectroscopy

Photoelectron spectroscopy (PES) is a highly surface sensitive technique because of the short inelastic mean free path (IMFP) of electrons in solids with an energy in the range of 10-1000 eV. The surface sensitivity can be further increased, either by changing angle between sample and the analyser or by changing kinetic energy that can be optimized with respect to the mean free path through the right choice of the photon energy [7]. The universal curve for the IMFP of the electron for a broad range of kinetic energies is reported in Fig. 2.3. It shows a clear minimum between 50 and 100 eV with the IMFP less than 10 Å; this means that the photoelectrons in that energy range mostly originate from the first few layers of the solid and thus makes photoelectron spectroscopy a unique tool for investigating electronic structure of thin films and solid surfaces and requires extremely well prepared, clean surfaces whose properties have to be maintained during the measurement. The shape of universal

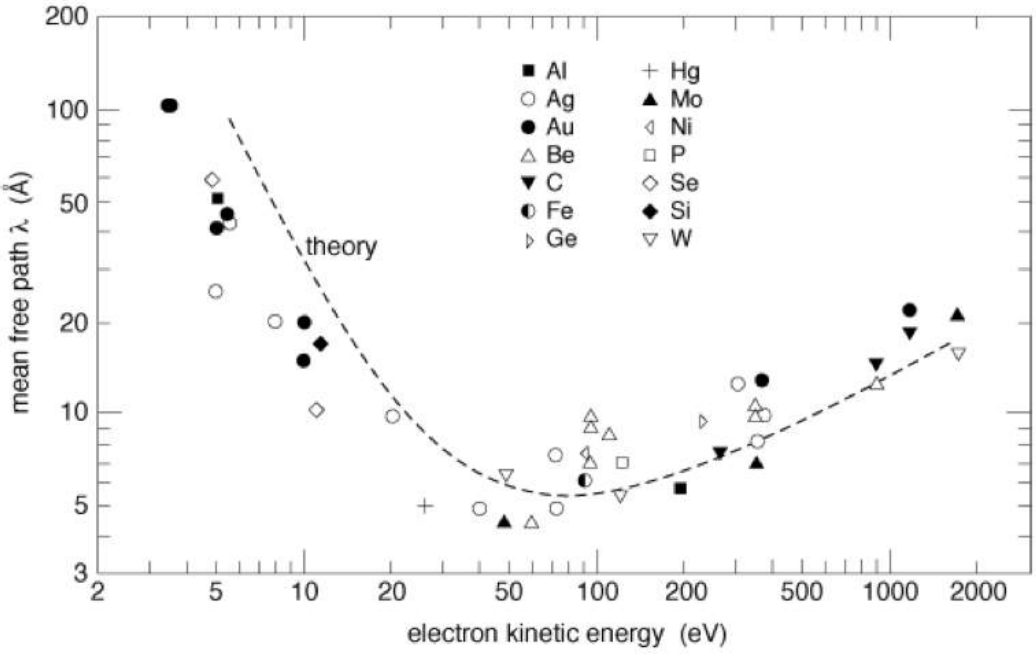

Figure 2.3: Universal curve of electron inelastic mean free path. Adopted from [9].

curve shows a rapid drop at 5-15 eV is due to the plasmon excitations, and at higher energies, the rise in the IMFP is related to the decrease of cross section for plasmon excitations, while the single particle excitations are below 5 eV.

The intensity of photoemission signal is related to the cross section which is defined as the probability per unit time for exciting a system from an initial state to a final state with a flux of 1 photon $cm^{-2}\ s^{-1}$ [10]. Figure 2.4 shows, as an example, the variation of the photoionization cross section for some of the core level analyzed in this thesis work, as a function of the incident photon energy. In fact, this offers the possibility to maximize (or minimize) the sensitivity to a specific core level under investigation, by simply tuning the photon energy. This figure points out one of the main advantages of using synchrotron radiation, *i.e.* the photon energy tunability. Soft X-ray techniques based on photoemission can be classified depending upon (i) photon energy and (ii) the electronic states of interest to be investigated. The photoelectron process is the same and division is purely based on the range of excitation energies used. Soft X-rays in the 100 to 1500 eV range typically used to probe core levels, and photoelectron spectroscopy in this case is referred as X-ray Photoelectron Spectroscopy (XPS). In order to maximize the cross-section, the optimal photon energy range is the ultraviolet (3-50 eV), so that, in this case, we talk

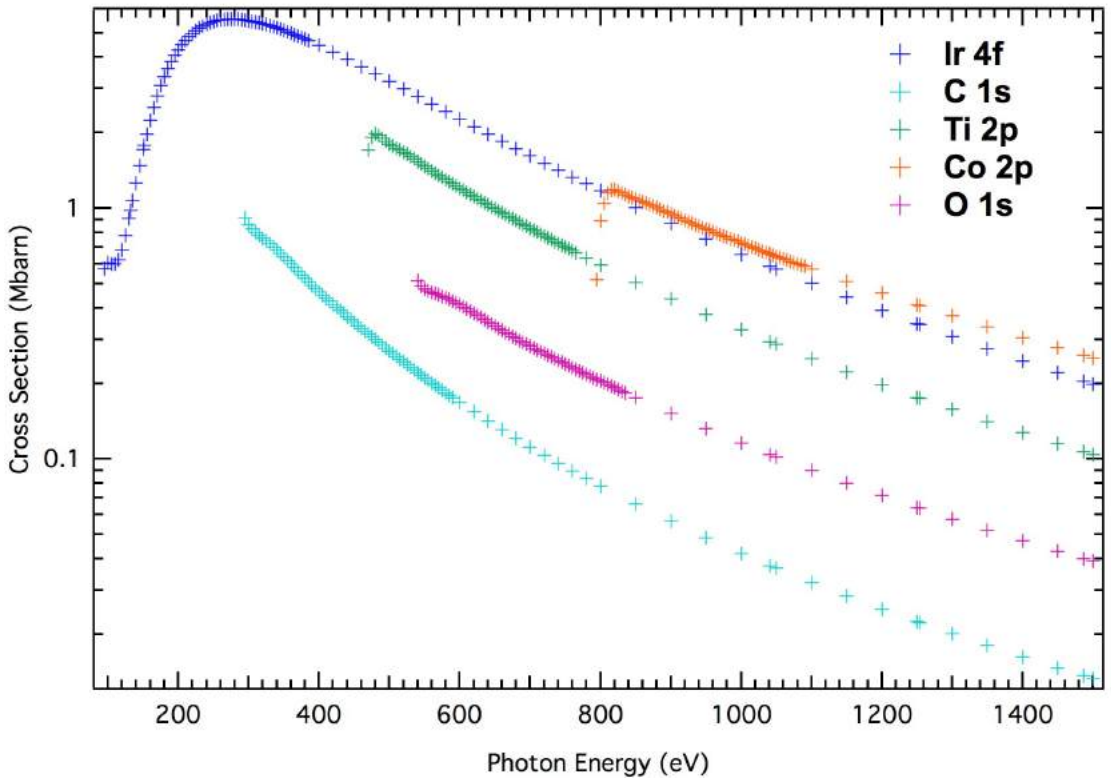

Figure 2.4: Photoemission cross-section for the Ir 4f, C 1s, Ti 2p, Co 2p, and O 1s core levels as a function of the incoming photon energy [11].

about Ultraviolet Photoelectron Spectroscopy (UPS). Here we can only probe the occupied states and can really extract information only about the valence band edge position. Moreover, by performing angle resolved photoelectron spectroscopy, where both energy and angular momentum are recorded, the band structure formed by the valence electrons can be mapped out.

2.3.4 Core level line shape spectral analysis

In order to get the detailed information from XPS spectra, a proper theoretical model is needed to fit the data. The most commonly employed model is the one formulated by Doniach and Sunjic [12], applicable to the metallic samples and highly conductive semiconductors. In a photoemission experiment the BE of the core electron in its ground state cannot be directly probed, since the measured BE incorporates both initial and final state effects. The finite core-hole lifetime and exponential decay probability for the core-hole relaxation gives the Lorentzian contribution to the line

shape, characterize by Full Width Half Maximum(FWHM) γ.

$$I_L(E) = I_0 \frac{\gamma^2}{(E - E_0)^2 + \gamma^2} \tag{2.5}$$

where I_0 is the intensity of the peak at $E = E_0$. During the photoemission process, additional electrons may be excited resulting in a partial energy loss for the photoelectrons. This kinetic energy lose, appearing as an asymmetric tail at high binding energy, was accounted by Doniach Sunjic trough a modified Lorentzian, in which they combine finite lifetime with electron-hole pair production as follows:

$$I_{DS}(E) = I_0 \frac{\Gamma(1-\alpha)\gamma}{\left[(E - E_0)^2 + \gamma^2\right]^{(1-\alpha)/2}} cos\left[\frac{\pi\alpha}{2} + (1-\alpha) tan^{-1}\left(\frac{E - E_0}{\gamma}\right)\right] \tag{2.6}$$

where α is the asymmetry parameter (if α = 0 then I_{DS}= I_L). The Gaussian broadening basically contains the resolution, the vibrational and the inhomogeneous contribution. The first effect is due to the non perfect monochromaticity of the photon beam and to the limited resolving power of the electron energy analyser, which pose an upper bound to the overall experimental energy resolution. The vibrational broadening is produced by the excitation of low energy vibrational modes both in the initial and in the final state. Finally, an inhomogeneous broadening may originate from the presence of unresolved core level shifted components in the spectrum. These to gather contributes to the Gaussian broadening, which can be described by

$$I_G(E) = \frac{I_0}{\sigma\sqrt{2}} exp\left(-\frac{(E - E_0)^2}{2\sigma^2}\right) \tag{2.7}$$

where σ is the Gaussian FWHM.

The photoemission spectrum also includes a background caused by inelastically scattered electrons. This background is either Shirley type or linear, depending on the specific spectrum. The background subtracted spectrum is calculate using formalism described in [13]

$$S_i(E) \propto \int_E^\infty d\acute{E}(I(E^{'}) - S_{i-1}(E^{'}) \tag{2.8}$$

where $I(E)$ is the experimental photoemission intensity, $S_i(E)$ is the Shirley intensity at the $i - th$ iterations. The calculation usually converges after 4-5 iterations and parameters were included in the fitting procedure.

2.4 X-ray absorption spectroscopy

X-ray Absorption Spectroscopy (XAS) is another experimental technique that take advantage of the tunability of synchrotron radiation: it probes the unoccupied states in a sample in the presence of a core hole. In a X-ray absorption process, photon is

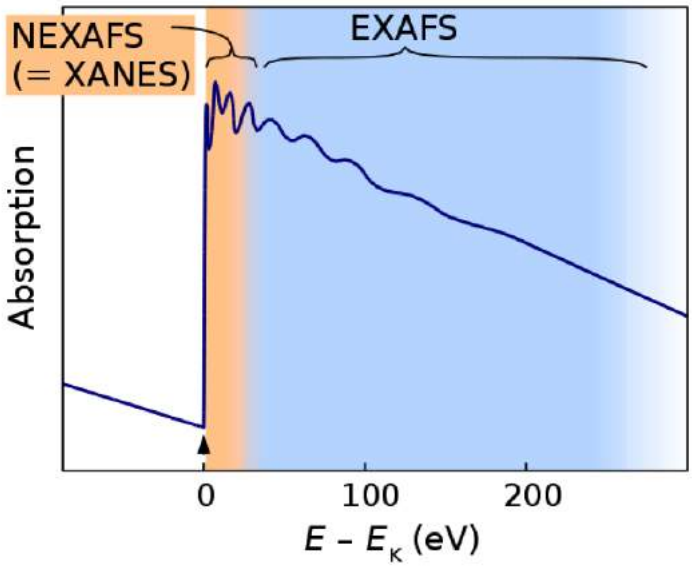

Figure 2.5: Schematic of a typical X-ray absorption spectrum.

absorbed by a core level electron which is excited into an unoccupied state above the Fermi level, leaving the atom in a highly excited neutral state. A spectrum is obtained by scanning the photon energy across an absorption edge. The absorption spectra thus contains several peaks which correspond to different resonances that occurs during the excitation of an electron from one shell to an unoccupied valence state above the Fermi level. These resonances are associated with the absorption threshold depending upon the atomic shell from which the electron is excited, accordingly they are referred as K, L, M....edges. The K-edge consists of a single edge as it corresponds to the excitation from 1s electrons, on other hand higher absorption threshold are a superpositions of edges, *i.e.* L-edge the excitations are from $2s, 2p_{1/2}$ and $2p_{3/2}$ levels, resulting in L1, L2 and L3 edges.

The XAS process is highly photon energy dependent and a peak in the XAS spectrum will be observed when the photon energy exactly matches the energy difference between the core excited final state and the ground state, given that the transitions are allowed by dipole selection rules. Fig. 2.5 presents two interesting

regions, Extended X-ray Absorption Fine Structure (EXAFS), extending from 50 eV up to few hundreds of eV, while on the other hand Near Edge X-ray Absorption Fine Structure (NEXAFS), or X-Ray Absorption Fine Structure (XANES), extends up to about 50 eV beyond the threshold. NEXAFS probes intramolecular transitions from deep core shell (usually the K shell) into the unoccupied molecular orbitals close to the vacuum level. This technique was developed in 1980 [14], used to solve the structure of molecules bonded to solid surfaces. The NEXAFS resonances are schematically

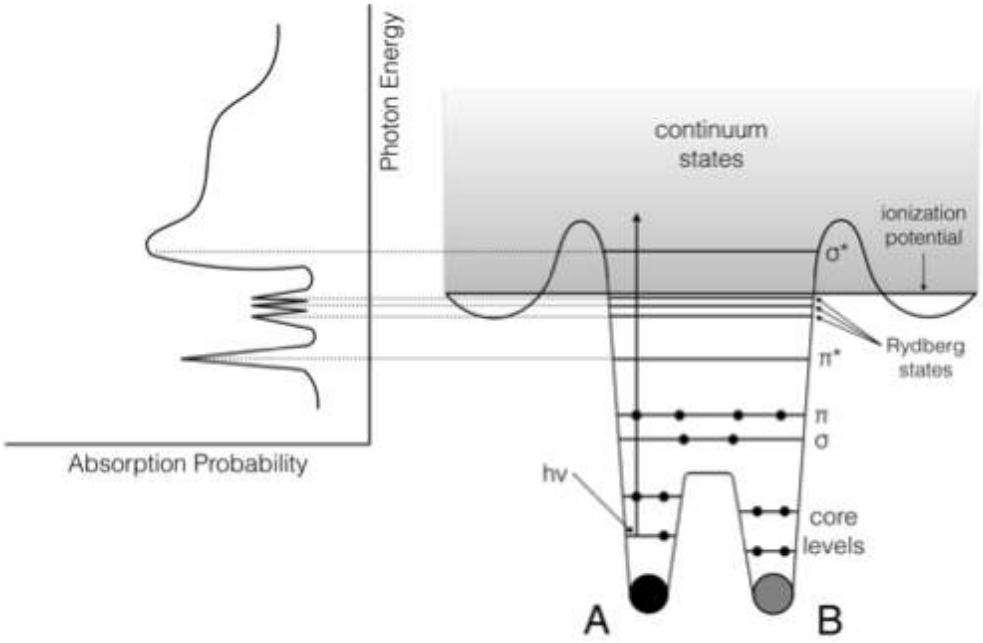

Figure 2.6: Schematic of the K-edge absorption spectrum (left) and potential (right) for a diatomic (A,B) molecule. π and σ resonances arise from the excitation of atomic 1s core level electrons to empty molecular orbital. The other resonances are due to transitions to Rydberg final states. Adapted from [15].

shown in Fig. 2.6 for a diatomic molecule. Resonant transitions occur only if the energy of the incoming photons matches exactly the energy difference between initial occupied states and an unoccupied state. By exploiting the polarized characteristic of synchrotron radiation NEXAFS allows to probe orientation of molecules along with their electronic structure. As in our case the light is linearly polarized and the photo-absorption cross section can be written as:

$$\sigma \propto |\epsilon \langle \Psi_f | \nabla | \Psi_i \rangle|^2 \rho_f(E) \tag{2.9}$$

where ϵ is the polarization vector of the incoming radiation and $\rho_f(E)$ is the density

of final states. For 1s initial state and a directional orbital final state, the matrix elements $\langle \Psi_f | \nabla | \Psi_i \rangle$ points in the direction Ω of the final state orbital. Eventually, absorption cross section can be written as:

$$\sigma \propto |\epsilon \langle \Psi_f | \nabla | \Psi_{1s} \rangle|^2 \propto |\epsilon \Omega|^2 \propto \cos^2 \delta \tag{2.10}$$

where δ is the angle between ϵ and Ω [15]. Gr is characterized by unoccupied in plane σ^* bonds and perpendicular to them are the out of plane π^* bonds. From above equation, it is clear that modulation of the σ^* and π^* resonances induced by a linearly polarized light, is therefore opposite. When the electric field polarization is in plane, the 1s to σ^* resonance intensity is maximum, while the 1s to π^* transition is inhibited. On the other-hand, when the electric field polarization is perpendicular to the plane, only π^* resonances can be measured. When a photon is absorbed it can promote the excitation of one electron to an unoccupied state, leaving behind a core hole. This hole is subsequently filled by an electron either with the emission of a fluorescent photon or by the emission of an Auger electron [16]. Different modes can be used when detecting the secondary electrons:

- Total yield, which means that all electrons (including both Auger and photo-electrons) at all kinetic energies are collected.
- Partial yield, where a retarding voltage in front of the XAS detector is used to cut off the low kinetic energy electrons.
- Auger yield, where a single Auger line is measured by adjusting the energy analyzer to accept electrons only in a selected energy window.

The surface sensitivity of XAS is determined by the mean free path of the emitted electrons, as well as by how many inelastically scattered electrons (with lower kinetic energy) are allowed to reach the detector. Total yield measurements are therefore more bulk sensitive, while partial and Auger electron yield (AEY) are more surface sensitive [14]. The NEXAFS measurements presented in this thesis work were acquired always using the AEY approach.

2.5 Synchrotron radiation

Elettra is a third generation synchrotron facility located in Trieste-Italy, which is optimized for the VUV and soft X-ray range. Synchrotron radiation facilities have the ability to produce tunable radiation of high intensity and brilliance. The basic principle of synchrotron radiation is that if the charged particles move at relativistic speed in a curved trajectory, they will emit a highly collimated photon beam in the tangential direction [17]. The electron bunches are generated in a small LINAC

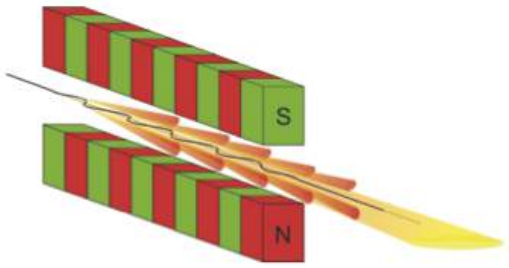

Figure 2.7: Schematic illustration of the radiation emitted by the periodic magnetic structure in an undulator. The figure is taken from [18].

(LINear ACcelerator). They start off from a ceramic disc that is heated to very high temperature. An electric field of up to 80 kV draws out the electrons that are then accelerated through two radio-frequency structures that make up the LINAC. The electrons exiting the LINAC are then transported to the inner side of the storage ring by a transfer line (a series of deflection and focussing magnets). Both the LINAC and transfer line are below ground so as not to interfere with beamlines in the experimental hall. The storage ring is filled by a multi-turn injection process whereby pulses of electrons are gradually feed into the ring ten times a second until the desired current is achieved. Refilling the ring to high currents takes 45 minutes. The storage rings consist of many straight sections, separated by bending magnets, which usually host insertion devices (undulators and wigglers). The bending magnets cause the electrons to move in a curved trajectory, undulators and wigglers consist of periodic magnetic structures forcing the electrons to experience oscillations as they move through insertion devices. The schematic illustration of an undulator is reported in Fig. 2.7, which consists of two periodic arrays of permanent magnetic poles that forces the incoming electrons to follow a wiggling trajectory, in such a way

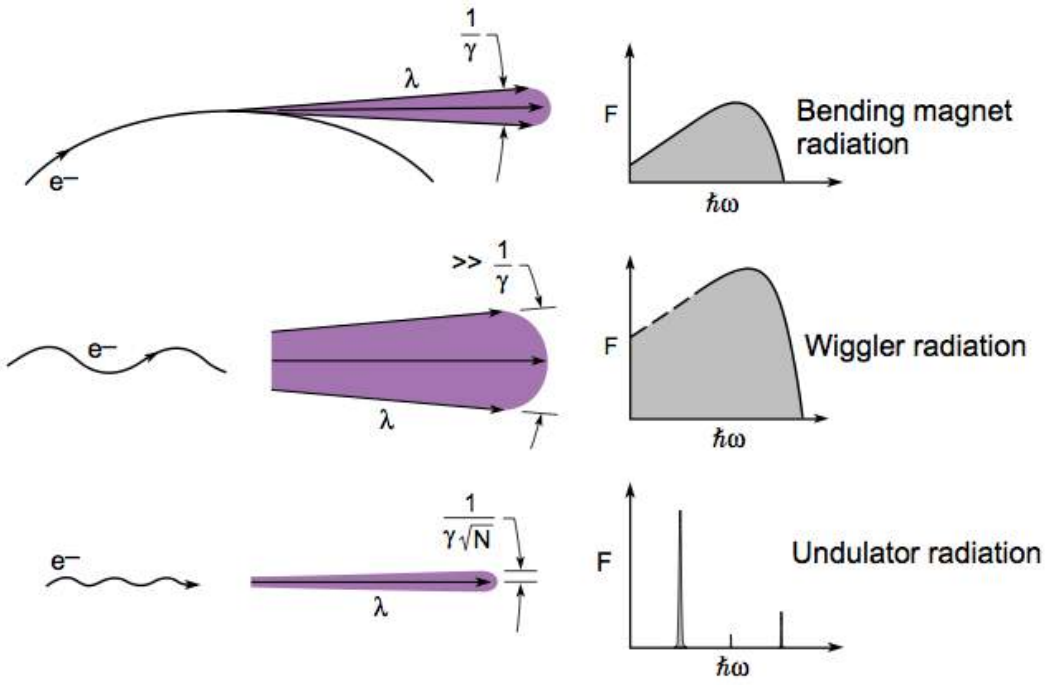

Figure 2.8: The radiation cone and radiation spectrum from bending magnets, wigglers and undulators. The width of the radiation cone is determined by γ, which is given by the electron energy (E_e) in the storage ring, $\gamma = \frac{E_e}{mc^2}$=1957. E_e and N, which is the numbers of periods in the magnetic structure. The figure is taken from [19]

to irradiate. The main difference between an undulator and a wiggler is the strength of the magnetic field, and therefore also the amplitude of the electron oscillations. The wavelength of the radiation emitted from an undulator can be tuned by changing the gap between the magnets in the periodic structure. The wigglers are a strong magnetic field version of undulators where radiation is not added in phase, resulting in a broader radiation cone in both space and angle. The radiation cone and the spectrum for bending magnets, wigglers and undulators is reported in Fig. 2.8. The radiation spectrum from a wiggler is similar to a bending magnet, except that it is shifted to higher energies and the total radiated power is much higher [19].

The radiation produced is directed into beamlines where the desired energy can be selected using a grating monochromator. The monochromatized light is focused onto the sample in the experimental station. In order to avoid energy losses due to collisions between electrons and molecules, since soft X- ray radiation (typically in the energy range of 30–1500 eV) is strongly absorbed by air, both the storage ring, the beamlines and the end stations have to be under vacuum [20]. The

main advantages of using synchrotron radiation with respect to a conventional X-ray source are manifold: tunability, wide range of photon energies are accessible by adjusting the undulator gap; brilliance *i.e.* a low divergence high photon flux within a narrow bandwidth and a high degree of polarization of photon beam.

2.6 The SuperESCA beamline at Elettra

This is the first beamline operating since 1993 at Elettra [21], optimized for photo-electron spectroscopy measurements with soft X-rays. The light beam produced by

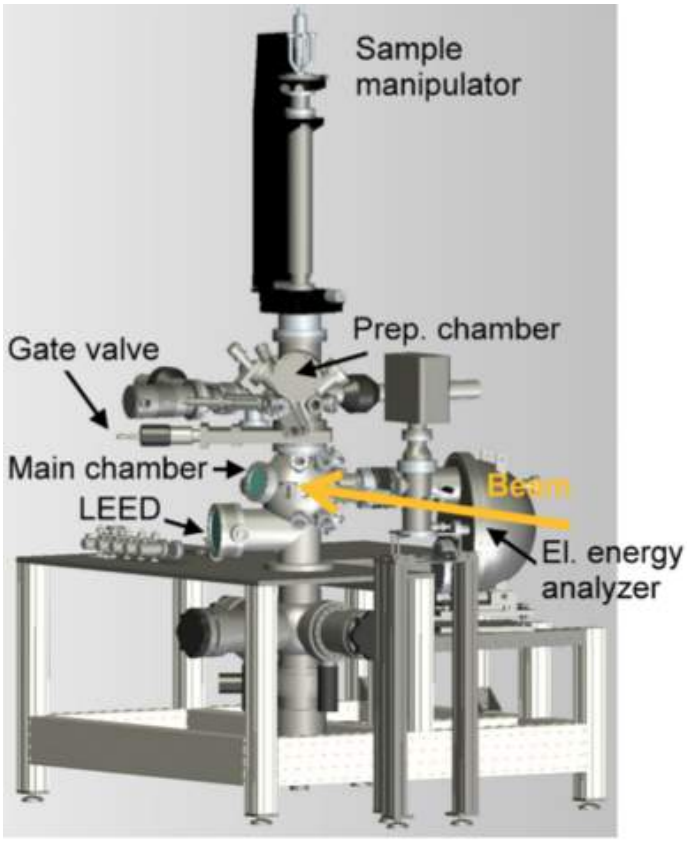

Figure 2.9: The end station of the SuperESCA beamline at Elettra.

the undulator is first pre-focused in the sagittal plane into the entrance slit, then monochromatized and, eventually, re-focused by an ellipsoidal mirror into the center of the experimental chamber. The radiation source is a two sections 46 mm-period high brilliance undulator with 98 periods, that produces linearly polarized radiation in the energy range 90-1500 eV. The highest attainable resolving power ($E/\Delta E$) of the monochromator is of the order of 10^4 for $h\nu \leq 400$ eV. The experimental end station

consists of two UHV chambers separated by a gate valve. A stainless steel chamber above is used for sample cleaning and preparation. The second chamber below is made of μ-metal[1] and is dedicated to the experimental measurements. A picture of the experimental setup is shown in Fig. 2.9. This end station can be equipped with two different manipulators during experiments. The first one provides four degrees of freedom (corresponding to the x, y, and z axes, and to the polar angle Θ) with a liquid He cryostat which allows to vary the sample temperature in the 20-1500 K range has been used in most of the experiment discussed in this thesis. The second one, is a modified manipulator with 5 degrees of freedom: 3 translational (x, y, and z) and 2 rotational (polar (Θ) and azimuthal (Φ)) axis. This manipulator is equipped with a liquid N_2 cryostat and an electron bombardment heating system which allows a sample temperature in the 120-1250 K range. This manipulator is specifically designed for XPD investigations where the photoemission intensity is measured as a function of the emission angle and this is possible with fully motorized rotational movements. The chamber is further equipped with a series of evaporators, a quadrupole mass spectrometer, a LEED system, and a SPECS Phoibos electron analyzer with a mean radius of 150 mm, equipped with a custom made delay line detector [22].

The hemispherical electron analyzer consists of two hemispherical electrodes (of radius R_1 and R_2 respectively) held at a proper voltage (see Fig. 2.10). The potential difference (V_2 - V_1) between the two hemispheres is expressed by equation below:

$$V_2 - V_1 = V_0(\frac{R_2}{R_1} - \frac{R_1}{R_2}) \tag{2.11}$$

This is used to calculate the potentials to be applied to the hemispheres in order to select electrons with energy E_0=$|e|V_0$, usually be called as pass energy. The analyzer is focusing in both directions, the electrons impinging entrance slit even with a small angle, will be focused at exit slit and thus can be revealed by the detector. The analyzer of SuperESCA beamline can be tuned either in "medium area" mode ($\pm 8^\circ$ acceptance angle) or in "wide angular mode" up to ($\pm 13^\circ$ acceptance angle). The energy resolution of the instrument depends upon the geometrical parameters of the analyzer, on the angular divergence of the electron beam and on the selected pass

[1]This alloy is used to screen external magnetic field due to its high magnetic permeability.

energy:

$$\Delta E = E_0(\frac{\omega}{2R_0} + \frac{\alpha^2}{4}) \tag{2.12}$$

ω in the equation is the width of the slit and α is the impinging angle of the electron beam at the entrance slit. The technical problems related to the dimensions of the analyzer set an upper bound to the values of R_0 which are actually achievable. The electrostatic lenses in front of the analyzer perform a double function: they collect the incoming photoelectrons from a large solid angle and focus them into the entrance slit of the analyzer, and at the same time, they slow down the electrons to the required kinetic energy E_0, which improve the resolution. Though, at low pass energy, the electron transmission probability of the system is damped, so that a compromise is actually required between a high energy resolution and a good signal-to-noise ratio.

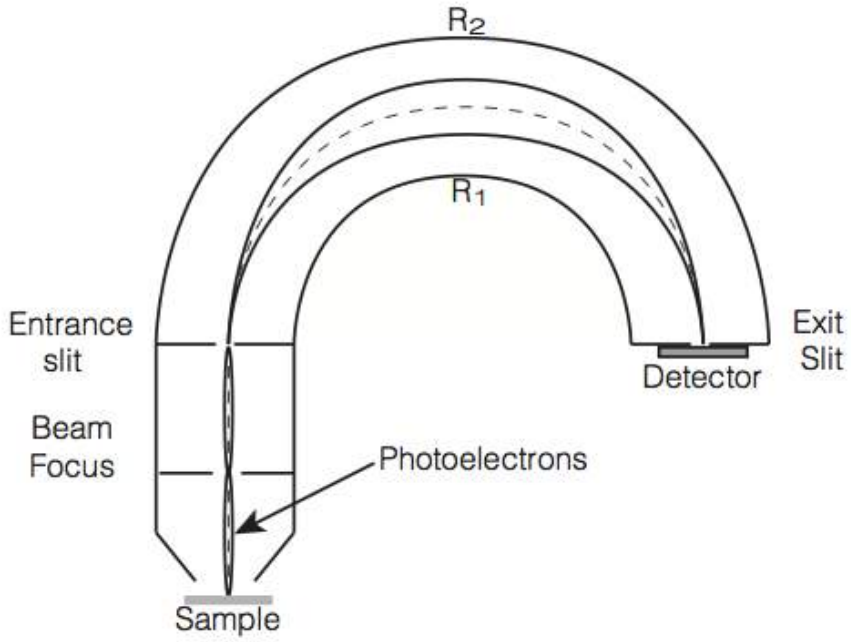

Figure 2.10: Illustration of a typical hemispherical electron energy analyzer.

The electrons that reach the exit slit at SuperESCA are collected by a microchannel plate based detection system and a delay line. When a spectrum is acquired in sweep (or scanning) mode, the voltages of the two hemispheres V_1 and V_2, and the pass energy, are held fixed and at the same time, the voltage applied to the electrostatic lenses is swept in such a way that each channel counts electrons with the selected kinetic energy for an interval equal to the given time window. Further,

to reduce the acquisition time per spectrum, the so called snapshot (or fixed) mode is alternatively applied at the SuperESCA beamline. This procedure exploits the relation between the kinetic energy of a photoelectron and its position inside the detector. If the energy range covered by the detector is wide enough, and if the photoemission signal collected by a large number of channels is sufficiently strong, it is possible to acquire the photoemission spectrum in one single shot, with an acquisition time of about 100 ms per spectrum.

2.7 The BaDElPh beamline at Elettra

The Band Dispersion and Electron-Phonon coupling (BaDElPh) beamline provides photons in the energy range 4.6-40 eV with high flux, high resolving power and horizontal-vertical linear polarization. The beamline performs primarily high resolution angle-resolved photoemission spectroscopy (ARPES) experiments in the low photon energy range. Photon energy lower than 15 eV provides enhanced bulk sen-

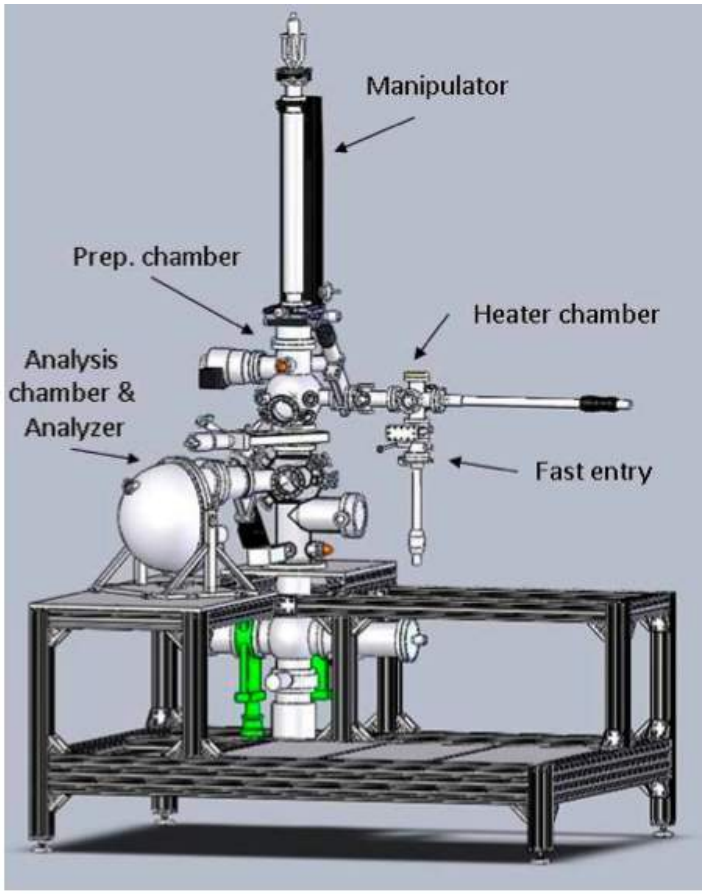

Figure 2.11: The experimental chamber of the BaDElPh beamline at Elettra.

sitivity with highest momentum and energy resolution and is also useful in tuning matrix elements which vary rapidly at low energy. At low photon energy photoemission is affected by the kinematic constrain deriving from energy and momentum conservation, and the *k*-dependent structure of the final states. For some initial state there is no final state that can be reached at a given photon energy and the intensity vanishes. Working at high photon energies the electron is excited in a continuum of high-energy states; a final state is always available and the photoemission process can take place (with intensity still dependent on matrix elements). A schematic picture of the BaDElPh end station is reported in Fig. 2.11. It consists of three UHV chambers: the heating, the preparation and the analysis chamber. The experimental chamber houses the electron energy analyzer, a SPECS Phoibos 150 with 2D-CCD detector system (the analyzer can be tuned either in "low angle dispersion" mode ($\pm 7^\circ$ acceptance angle) or in "wide angular dispersion" mode up to ($\pm 13^\circ$ acceptance angle), a UV source (He) due to the other branchline, beam is not available all the time, a conventional X-ray source (Al & Mg), a low energy electron diffraction (LEED) optics, and a residual gas analyzer (RGA). It is also equipped with a 5 degree of freedom fully motorized manipulator along with liquid He cryostat. The electron detector is made up by a set of multichannel plates used to amplify the signal. After this amplification stage, the electrons are collected by a phosphorous screen. The image generated on the screen is recorded by a high resolution CCD camera. The use of a 2D detector offers the possibility of simultaneous acquisition of the energy as well as the angular distributions of the photoelectrons. This is achieved by probing both the dispersive plane and the non dispersive plane of the analyzer (see Fig. 2.12). In the dispersion plane of the analyzer, that is the plane containing the focusing lenses and the detector, the electron energy can be measured in the range given by the pass energy. On the other hand, the polar plane angle dispersion is detected in the orthogonal plane which gives maximum angular acceptance of about 26°. This setup gives overall angular resolution of about 0.1°, with 5 meV maximum energy resolution.

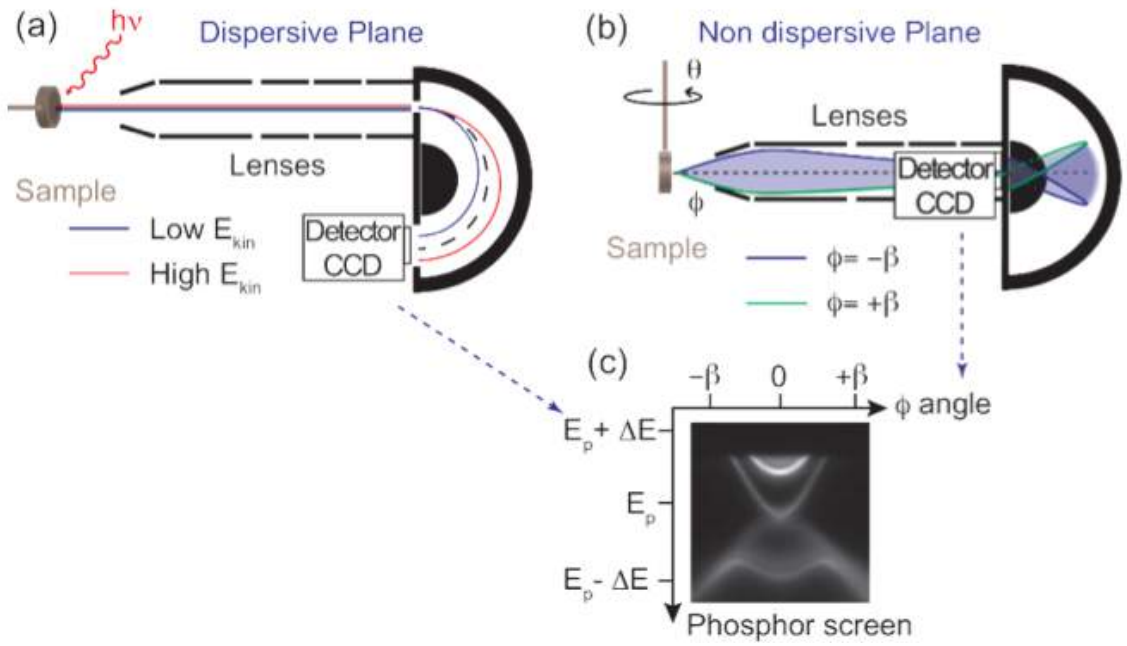

Figure 2.12: Scheme of the detection planes of an hemispherical electron analyzer. (a) Definition of the dispersive plane of the analyzer with the orbits of the higher (lower) kinetic energy electrons in red (blue). (b) Definition of the non-dispersive plane of the analyzer with the orbits of the electron emitted at an angle $+\beta(-\beta)$ in green (blue). (c) Sample image of an acquired spectrum.

2.8 The Nanospectroscopy beamline at Elettra

The Nanospectroscopy beamline has been designed to deliver high photon flux density at the microscope focus in order to increase the beamline efficiency. Two undulators with a period of 10 cm, phased by a modulator electromagnet, are used as a source; they provide elliptical polarized radiation as well as vertical and horizontal polarization in special cases. The beamline employs a high throughput monochromator based on the variable line spacing grating scheme, covering the energy range from 40 to 1000 eV and one spherical grating for low energies. Two bendable elliptical mirrors arranged in Kirkpatrick-Baez configuration, give a micron-sized illumination spot which is matching well with working conditions, i.e. field of view between 2 μm and 10 μm. The beamline is equipped with LEEM apparatus with a lateral resolution of few tens of nanometer. This instrument can be used to acquire photoemission electron microscopy (PEEM) data as well as μ-ARPES and μ-XPS spectra when the electron source of the microscope is replaced by the incoming X-ray synchrotron

radiation. These techniques can combine the spatial resolution of electron microscopy and the chemical sensitivity of photoelectrons spectroscopy, opening new possibilities for the local characterization of the samples. The instrumental chamber, as shown in Fig. 2.13, consists of a preparation chamber connected to the main experimental chamber by a valve, which is used for sample cleaning and preparation. Different gases can be introduced directly into the main chamber through leak valves and several evaporators can also be mounted.

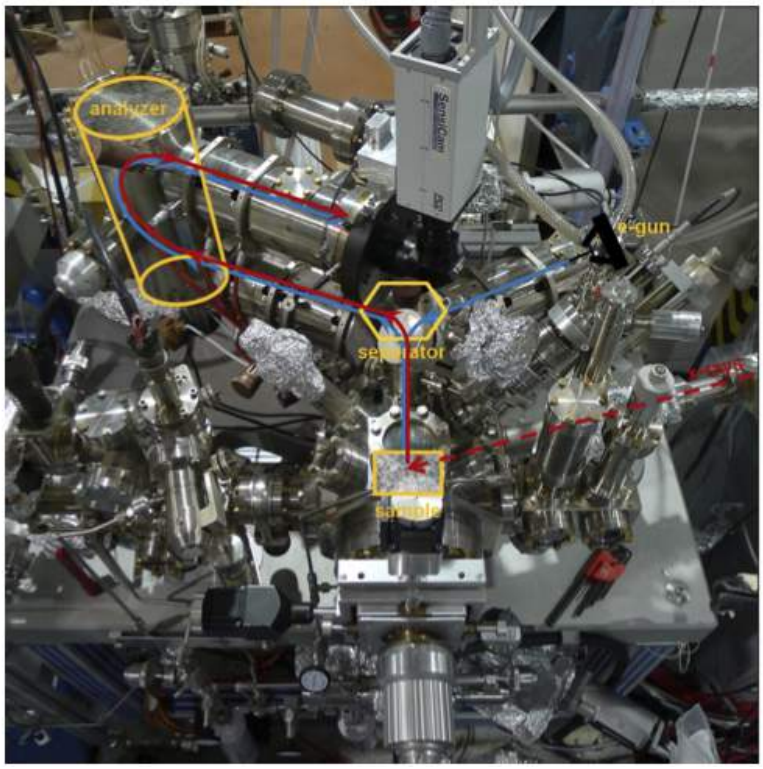

Figure 2.13: The experimental chamber of the Nanospectroscopy beamline at Elettra.

2.8.1 Low Electron Energy Microscopy

Part of the thesis work was carried out using advanced microscopy methods giving access to the surface morphology, structure and composition. Low energy electron microscopy (LEEM) at Nanospectroscopy beamline of Elettra was used.

LEEM is a cathode lens microscopy technique which probes surfaces and interfaces with elastic backscattering of low energy electrons, in which sample acts as the cathode by emitting electrons in the objective lens of the microscope. LEEM is a surface sensitivity technique where the photon energy is kept constant; and is chosen

to maximize both photoemission cross section and surface sensitivity to the surface emitters. This technique also provides a unique property to probe also deeper layers and interfaces by working with low energy electrons down to few eV, which have a mean penetrating depth of several nanometers. So the electrons with such low energy range have high reflectivity which, combined with the non scanning imaging mechanism, is translated into a short image acquisition time and real time imaging capability.

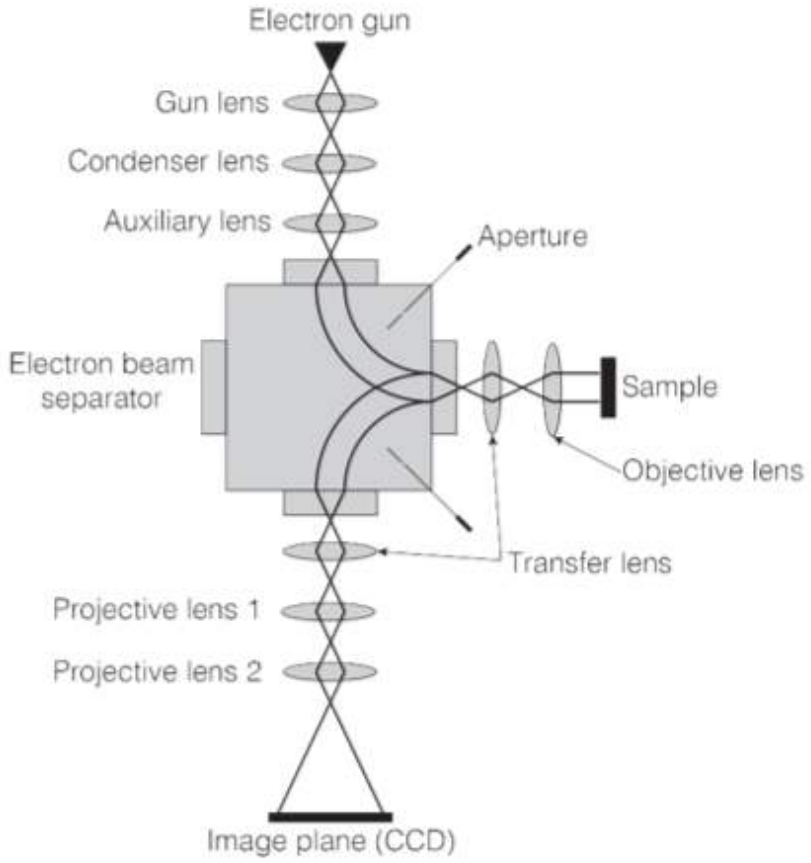

Figure 2.14: The LEEM system scheme.

The basic scheme of LEEM system is shown in Fig. 2.14. The electrons are emitted from the cathode and accelerated to an energy of several keV (typically 18 keV). There are a set of electromagnetic lenses for the alignment of the beam to the axis of objective lens, perpendicular to the surface, and to focus it in the crossover of the back focal plane of objective lens. The beam separator deflects electrons from their original trajectory allowing them to reach the surface at normal incident. Before

reaching the sample the electrons are decelerated to low kinetic energy. The kinetic energy range is generally tuned in the range from few to few hundreds eV. The voltage offset between the e-gun and the sample is called the start voltage. It defines the kinetic energy of the electrons arriving at the sample, and different values give different mechanism of contrast (like work function). The work function contrast is originated at the total reflection threshold at very low start voltages: where the electrons have barely enough energy to overcome surface barrier (usually it happens at 0-2 eV for most of the materials). The electrons interact with the surface and are elastically backscattered. The reflected electrons are then re-accelerated through the objective lens, flowing in the opposite direction. The objective provides a magnified image of the specimen in the beam separator which is further magnified by several additional lenses in the imaging column of the instrument. The image is projected onto an imaging detector with micro-channel plate and phosphorous screen, and finally acquired by a computer controlled CCD camera. The LEEM instrument can be used as LEED by changing the settings of the lenses in the imaging column. The LEED patterns can be obtained as an image of the diffraction plan; alternatively, a real space image can be obtained by inserting a contrast aperture in the diffraction plane and selecting one of the diffracted beams. This aperture, placed along the beam path inside the illumination column, enables the selection of field of view, *i.e.* the width of the surface region to be imaged. In this way the microscope will operate in LEED mode and it is possible to collect the micro-spot low energy diffraction (μ-LEED) patterns of specific regions of the sample.

The most frequently used contrast method in the LEEM is the diffraction contrast. The backscattering intensities and their energy dependence may vary considerably depending on surface structures. LEEM images can be produced using either zero or first order diffraction beams, but also fractional can be used. The diffraction beams are selected by means of a contrast aperture which is inserted in the one of the diffraction planes encountered along the imaging column of the microscope. The most commonly used LEEM image mode is contracted using the zero order diffraction beams. This is called bright-field (BF) mode; here the contrast is due to the difference in the electron reflectivity of different surface phases and structures. Bright field is the standard mode of operation with the best spatial resolution. The

BF contrast are being generated due to the height difference between terraces on the surface which leads to a phase difference in the backscattered waves. Defocussing can also convert such phase difference into an amplitude difference. In the dark-field (DF) LEEM, higher or fractional order diffraction spots are used to image the surface. The DF mode allows a direct measurement of the lateral extent of a given surface phase and allows to separate the contributions of rotationally inequivalent domains and over layers which are indistinguishable at normal incidence, where they don't produce contrast. This method basically exploits the interference of waves that are backscattered at the surface and at the interface of a thin film, resulting in maxima and minima in the backscattered intensity depending upon the local film thickness.

2.9 Low energy electron diffraction

Low energy electron diffraction is rooted in the fact that electrons have particle duality as suggested by Louis de Broglie in 1924. The possibility that electrons could diffract from crystalline solids was experimentally confirmed by Davission and Germer in 1927 [23]. Even today this technique is one of the most powerful tool to investigate ordered surfaces. In LEED low energy electrons (20-300 eV) are

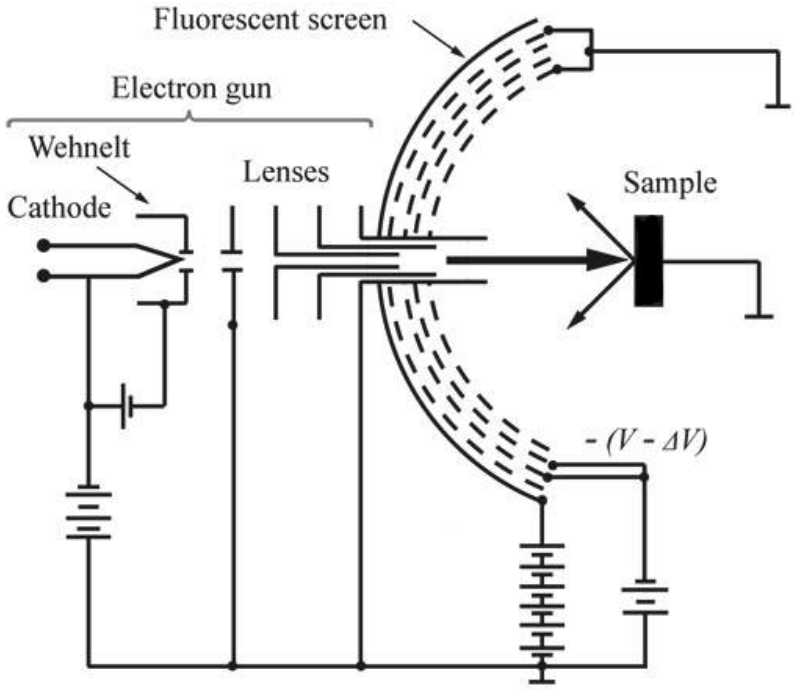

Figure 2.15: Schematic illustration of a typical LEED apparatus.

used, yielding wavelength around 1 Å which is in the same order of magnitude as the periodicity of the atomic lattice, a requirement for forming diffraction patterns. The surface sensitivity is due to the short mean free path of low energy electrons, typically around 10 Å for 100 eV electrons. The I-V measurements of the diffracted spots provide structural information on average bond angles, nearest neighbour distances and translational symmetry. Moreover, the sharpness of the diffraction pattern reflects the long range order of the surface, and the presence of defects.

A schematic diagram of a typical LEED system is shown in Fig. 2.15. It consists of an electron gun with a variable accelerating potential which generates a mono-energetic electron beam. The electrons are accelerated and focused by a series of electrostatic lenses before hitting the grounded sample. A hemispherical retarding field energy analyzer, consisting of four hemispherical concentric grids and a fluorescent screen, is used for detecting the electrons. Electrons scattered from the surface travel to the first spherical sector grid, which is at the same potential as the sample providing a field-free region between the sample and the grid. The next two grids are placed at a potential to discard electrons resulting from inelastic scattering events. After being accelerated to about a few keV, the diffracted electrons hit the fluorescent screen, where the diffraction pattern can be observed.

2.10 Photocatalytic activity set-up

The photocatalytic activity was evaluated under simulated sunlight irradiation as shown in Fig. 2.16, using a solar simulator (LOT-Oriel) equipped with a 150 W Xe lamp and an atmospheric edge filter to cut-off UV photons below 300 nm. The beam was focused on the sample and the resulting light intensity was 25 mW cm^{-2} (250–400 nm, UV-A) and 180 mW cm^{-2} (400–1000 nm, Vis-NIR). The incident illumination power is close to twice of a standard AM 1.5 (is a standard filter used in photocatalysis, to simulate the power of sunlight) and is representative of a simple but effective solar concentrator. Photo-catalytic experiments were performed using sensitizers in visible range with head spaced vials (total volume 20 mL). The vial containing sample was filled with 12.5 mL solution with water and methanol 1:1 ratio. The vial was then sealed using appropriate rubber septa and the air was removed bubbling

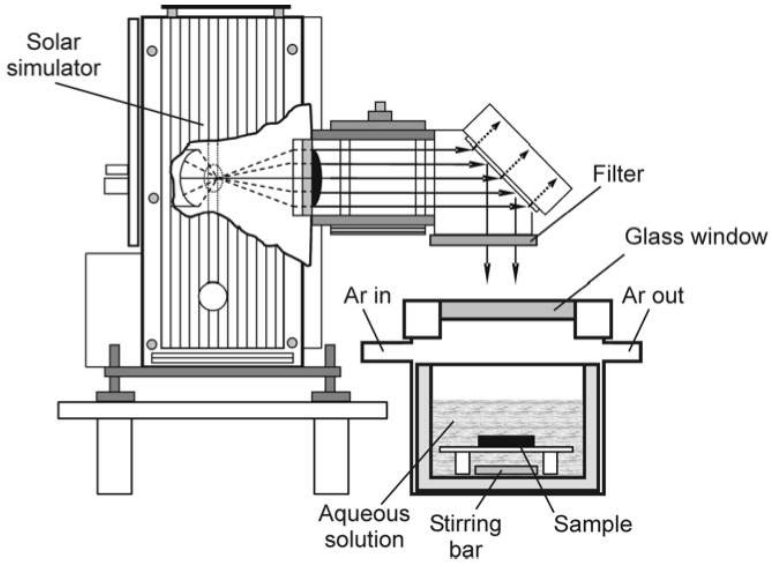

Figure 2.16: Schematic representation of the reactor used for photocatalytic experiments.

Ar for 30 minutes. After this equilibrium period, the vial was irradiated using the system shown in Fig. 2.16. The analysis of the reaction products was performed injecting 50 μL of the gas phase into a gas chromatograph (Agilent 7890). The Thermal Conductivity Detector (TCD) was used for the quantification of H_2, using a MoISIEVE 5A column with Ar as carrier. This is a chemical specific detector and senses the changes in thermal conductivity of column effluent (discharged product) and compares it to a reference flow of carrier gas. The thermal conductivity of most of the compounds is less than the common carrier gases like helium or argon. When an analyte elutes, the thermal conductivity of the column effluents is reduced, thus producing a delectable signal.

Bibliography

[1] D. P. Woodruff, and T. A. Delchar. *Modern techniques of Surface Science.* 2nd edition, Cambridge University Press, Cambridge, 1994.

[2] H. Hertz. Ann. Physik, 267:983, 1887.

[3] A. Einstein. Ann. Physik, 322:132, 1905.

[4] K. Siegbah, C. Nordling, A. Fahlmann, R. Nordberg, K. Hamin, J. Hedman, G. Johansson, T. Bergmark, S. Karlsson, I. Lindgren, and B. Lingberg. *ESCA: atomic, molecular and solid state structure studied by means of electron spectroscopy.* Almqvist and Wiksells, Uppsala, 1967.

[5] H. Lüth. *Solid Surfaces, Interfaces and Thin Films.* Springer, 2001.

[6] F. Reinert, and S. Hüfner. *Photoemission spectroscopy—from early days to recent applications.* New Journal of Physics, 7:97, 2005.

[7] S. Hüfner. *Photoelectron Spectroscopy: Principles and Applications.* Springer, 2003.

[8] C. S. Fadley, S. B. M. Hagstrom, M. P. Klein, and D. A. Shirley. *Chemical Effects on Core-Electron Binding Energies in Iodine and Europium.* The Journal of Chemical Physics, 48(8):3779–3794, 1968.

[9] A. Zangwill. *Physics at Surfaces.* Cambridge University Press, 1988.

[10] C. S. Fadley. *Basic Concepts of X-ray Photoelectron Spectroscopy in Electron Spectroscopy. Theory, Techniques, and Applications.* C. R. Brundle and A. D. Baker editions, vol. II:1–156, Pergamon Press, 1978.

[11] J. J. Yeh. *Atomic Calculation of Photoionization Cross-Sections and Asymmetry Parameters.* Gordon and Breach Science Publishers, Langhorne, PE (USA), 1993.

[12] S. Doniach and M. Šunjic. *Many-electron singularity in X-ray photoemission and X-ray line spectra from metals.* Journal of Physics C: Solid State Physics, 3(2):285, 1970.

[13] J. Végh. *The Shirley background revised. Journal of Electron Spectroscopy and Related Phenomena.* 151(3):159–164, 2006.

[14] J. Stöhr. *NEXAFS spectroscopy,* volume 25. Springer Science & Business Media, 2013.

[15] G. Hähner. *Near edge X-ray absorption fine structure spectroscopy as a tool to probe electronic and structural properties of thin organic films and liquids.* Chemical Society Reviews, 35(12):1244–1255, 2006.

[16] H. Winick, and S. Doniach. *Synchrotron radiation research.* Springer Science & Business Media, 2012.

[17] A. Hofmann. *The physics of synchrotron radiation.* Cambridge University Press, New York, Volume, 13, 2004.

[18] Homepage of HASYLAB at DESY, http://hasylab.desy.de.

[19] Lecture notes in *Synchrotron Radiation for Materials Science Applications.* University of California, Berkeley, http://www.coe.berkeley.edu/AST/ srms.

[20] D. Attwood. *Soft X-Rays and Extreme Ultraviolet Radiation.* Cambridge University Press, 1999.

[21] A. Abrami, M. Barnaba, L. Battistello, A. Bianco, B. Brena, G. Cautero, Q. H. Chen, D. Cocco, G. Comelli, S. Contrino, F. DeBona, S. Di Fonzo, C. Fava, P. Finetti, P. Furlan, A. Galimberti, A. Gambitta, D. Giuressi, R. Godnig, W. Jark, S. Lizzit, F. Mazzolini, P. Melpignano, L. Olivi, G. Paolucci, R. Pugliese, S. N. Qian, R. Rosei, G. Sandrin, A. Savoia, R. Sergo, G. Sostero, R. Tommasini, M. Tudor, D. Vivoda, F. Q. Wei, and F. Zanini. *SuperESCA: First beamline operating at Elettra.* Review of Scientific Instruments, 66(2):1618–1620, 1995.

[22] G. Cautero, R. Sergo, L. Stebel, P. Lacovig, P. Pittana, M. Predonzani, and S. Carrato. *A two-dimensional detector for pump-and-probe and time resolved experiments.*

Nuclear Instruments and Methods in Physics Research Section A: Accelerators, Spectrometers, Detectors and Associated Equipment, 595(2):447–459, 2008.

[23] C. Davisson, and L. H. Germer. *Diffraction of Electrons by a Crystal of Nickel.* Physical Review, 30:705, 1927.

Chapter 3

Tunning the graphene-metal interaction strength by intercalation

The most commonly employed method for the Gr growth on transition metals surfaces is the chemical vapor deposition. In this method the source of C-atoms are the gas phase hydrocarbon precursors provided to the substrate (transition metal, TM). These hydrocarbon precursor, then form the C adatoms through decomposition on the hot TM substrate, resulting in a single-layer Gr-island. The interaction between epitaxial graphene and the TM surface is highly dependent upon the choice of the substrate. These interactions between Gr-metal surfaces causes modifications of its properties that make it unique, mainly because of charge transfer process, rehybridization and changes to its band structure [1, 2, 3].

A good understanding of the interactions occurring at interfaces between graphene and metals is therefore required to grow metal or oxide clusters which can find possible application in field of catalysis. The metallic surfaces where graphene can be grown or deposited, can be classified depending on the degree of interaction they establish with it [4, 5, 6]. Some show a weak, van der Waals-like coupling and are characterized by a graphene–surface separation close to the interlayer distance of graphite (around 3 Å), such as Ir(111) [6] and Pt(111) [7]. The others, instead, display a much stronger interaction, such as Ru(0001) [8, 9, 10] and Re(0001) [11, 12, 13]: in these cases, the graphene–surface distance is reduced, the nearest carbon atoms lying at approximately 2 Å from the metallic surface. One possibility is related to the lattice mismatch between graphene and that of the underlying surface which induces

a different degree of re-hybridization on different C atoms, and is known to drive the formation of moiré superstructures of epitaxial graphene on transition metals [14]. The geometry of the metallic surface not only causes strain on graphene as its lattice parameter adapts to that of the substrate, but could also influence its electronic configuration. In this respect if we have grown Gr on the strongly interacting metal substrate, then these metal surfaces could also interact strongly with metallic clusters grown on top of Gr, which makes them lose their individual character. For this reason, a deeper understanding of graphene structural, chemical and physical properties, together with its interactions on different substrates and different chemical species would be very important. So, it is highly desirable to find a suitable metal substrate for Gr-growth giving us almost a free-standing graphene for the investigation of supported cluster properties.

The main focus of the combined experimental and theoretical investigation presented in this chapter was to distinguish the contributions arising from the geometrical (lattice mismatch) and chemical (elemental composition of the substrate) properties of the surface on the interaction between graphene and metals [15]. We have achieved this by systematic intercalation of different metallic species at graphene–metal interfaces, following the scheme reported in Fig. 3.1.

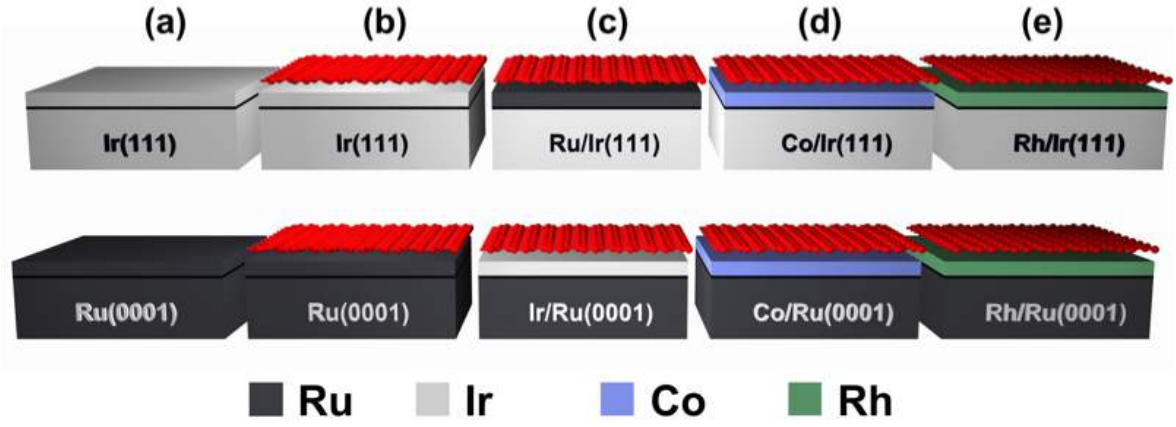

Figure 3.1: Schematic outline of the experimental procedure followed in this investigation. (a) Pristine Ir(111) (top row) and Ru(0001) (bottom row) surfaces. (b) Graphene growth on the two substrates. (c-e) Intercalation of different metallic species (Ru, Ir, Co and Rh) at the Gr/metal interfaces.

The intercalation process, in fact, modifies the chemical composition of the first surface layer while preserving the symmetry and the lattice constant of the

substrate, provided the intercalated layer is of monoatomic thickness. In order to make an extensive comparison in a controlled and reproducible way, two different single-crystal close-packed metallic surfaces were used: Ir(111) which known to interacts weakly, while Ru(0001) interacts strongly with graphene. Both substrates have a lattice parameter (2.70 Å for Ru and 2.72 Å for Ir) which is larger than that of graphene (2.46 Å). The chosen intercalated species also reflects a different degree of freedom with graphene when the latter is grown on their hexagonal close-packed surfaces. Beside Ru and Ir, we also employed Rh which shows an intermediate interaction strength with graphene and Co, which is even more strongly interacting than Ru.

3.1 Methods

3.1.1 Experimental

High quality graphene was grown on Ir(111) and Ru(0001) by means of ethylene CVD. For the growth on Ir(111) a temperature programmed growth approach was adopted, consisting of repeated cycles of ethylene adsorption at room temperature up to surface saturation followed by annealing to 1400 K. Instead for Ru(0001), the sample was kept at 1100 K in increasing ethylene pressure (up to 5×10^{-8} mbar) until a single layer Gr was formed. The graphene formed in these two methods is of high quality with low density of defects [16, 17, 18, 19]. Photoemission spectra were measured at the SuperECSA beamline of Elettra in normal emission conditions. The C 1s spectra were measured using a photon energy of 385 eV with an overall experimental resolution of 40 meV. The intercalation was obtained by sublimation from high purity wire while keeping the sample surface at 700 K: this temperature generally allows metal atoms to have enough mobility to diffuse above graphene, reach a suitable site for intercalation (mainly grain boundaries) and diffuse below the surface, while it has been demonstrated that metallic species deposited at ambient temperature usually tend to remain above graphene and form clusters on top of graphene [20, 21, 22]. With the help of LEED measurements it was confirmed that the lattice parameters were not modified by the intercalation, *i.e.* the intercalated layer was pseudomorphic. Almost 1 monolayer (ML) of metal was deposited for each

system and coverage was determined using Eq 3.1 (see detailed discussion on page 52). The evolution of chemical, structural and electronic properties was followed by acquiring the C 1s core-level spectra of graphene. The surface was cleaned after each intercalation step by means of repeated cycles of sputtering, annealing and chemical treatment (oxygen and hydrogen). The surface cleanliness was again verified through photoemission measurements before regrowing graphene using the same procedures.

3.1.2 Theoretical

Theoretical calculations were performed using Density Functional Theory (DFT) by overlaying a Gr sheet over a (12×12) and a (9×9) super cell for Ru(0001) and Ir(111), respectively. The metal surfaces were modeled using a slab with a thickness of 5 layers, with the atoms of the 2 bottom layers kept fixed at their bulk positions, while all the other atoms were allowed to relax. By modifying the chemical species of the topmost metallic layer we were also able to model the systems obtained from the intercalation of metals below graphene. This approach allows to describe systems where a single layer of metal is intercalated below graphene with high accuracy. However, it does not take into account local defects which are unavoidable in real systems, such as vacancies or small 3-dimensional islands composed of two (or more) layers of intercalated metal. The calculations reported in this chapter were done by the group of Prof. Alfè at UCL.

3.2 Characterization of graphene-metal interactions

3.2.1 Experimental results

The high resolution C 1s core level spectrum obtained after graphene growth on Ru(0001), presented in Fig. 3.2 (a), shows two distinct components: a weaker one (S3) at 284.47 eV, and a more intense and narrower one (S1) at 285.13 eV. These are recognized as a sign of lattice mismatch (corrugation) between graphene and metal substrate. These C 1s components arise from non equivalent atomic configurations: the lower BE is mainly generated by the atoms in the upper portion of the carbon layer, and the one at higher BE is generated by atoms closer to the substrate. The

analysis of the C 1s spectra of graphene on Ru(0001), as shown in Fig. 3.3, was complicated by the overlap of the 1s core level of carbon and the $3d_{3/2}$ core level of Ru. It was therefore necessary, to include the Ru $3d_{3/2}$ core level, in the analysis of the C 1s spectrum for determining the line-shape from the $3d_{5/2}$ component.

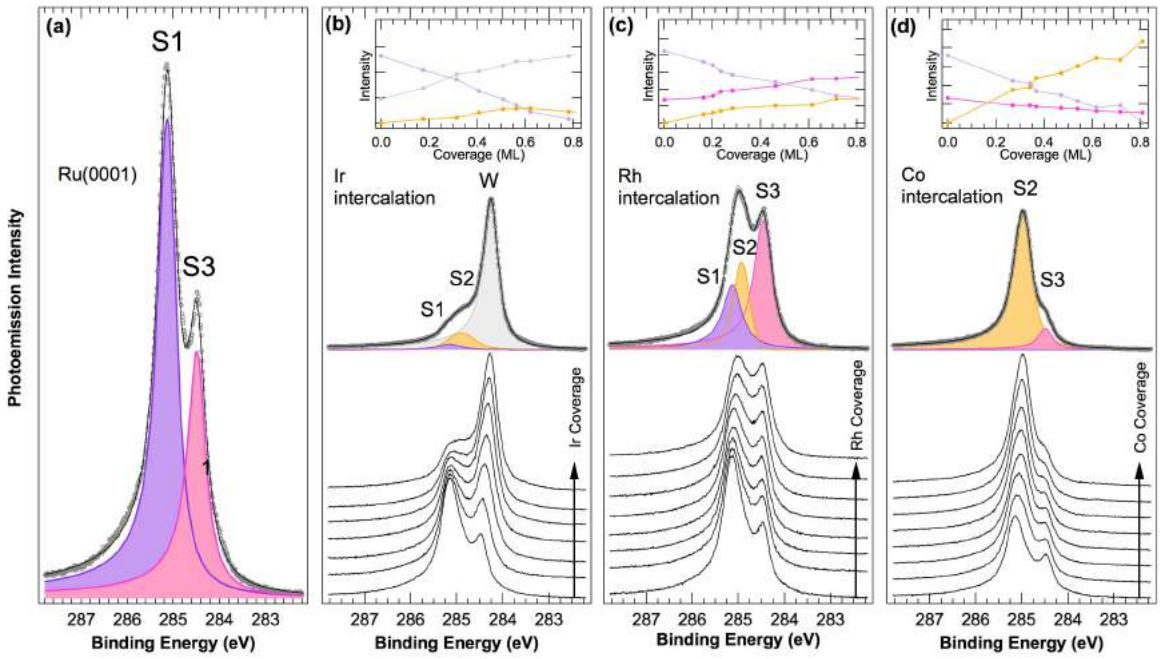

Figure 3.2: C 1s core level spectra of Gr/Ru(0001) during intercalation ($h\nu$=385 eV). (a) Pristine Gr/ Ru(0001). (b-d) Evolution of the C 1s spectrum during intercalation of (b) Ir, (c) Rh and (d) Co. Top graphs show the evolution of the area of all C 1s photoemission components corresponding to non-equivalent C populations at increasing intercalating metal coverages.

Contrary to the Gr/Ru(0001) case, the C 1s core level spectrum obtained after Gr growth on Ir(111) is presented in Fig. 3.4 (a). The spectrum consists of a single narrow component (W) with a FWHM of 270 meV and a BE of 284.12 eV, which is the fingerprint of quasi free standing Gr [4, 18]. The small shoulder visible at higher BE is due to the presence of a small amount of defects in the C network.

We also performed SPA-LEED (transfer width of our SPA-LEED was measured to be larger than 1000 Å [23]) measurements (see Fig. 3.5) to check quality and long range order of the graphene layers synthesized on the two substrates. The diffraction spots are narrow and bright: the absence of additional diffraction spots, besides those arising from Gr, the substrate, and the moiré, clearly exclude the presence of other superstructures or rotational domains. Thus we conclude from the

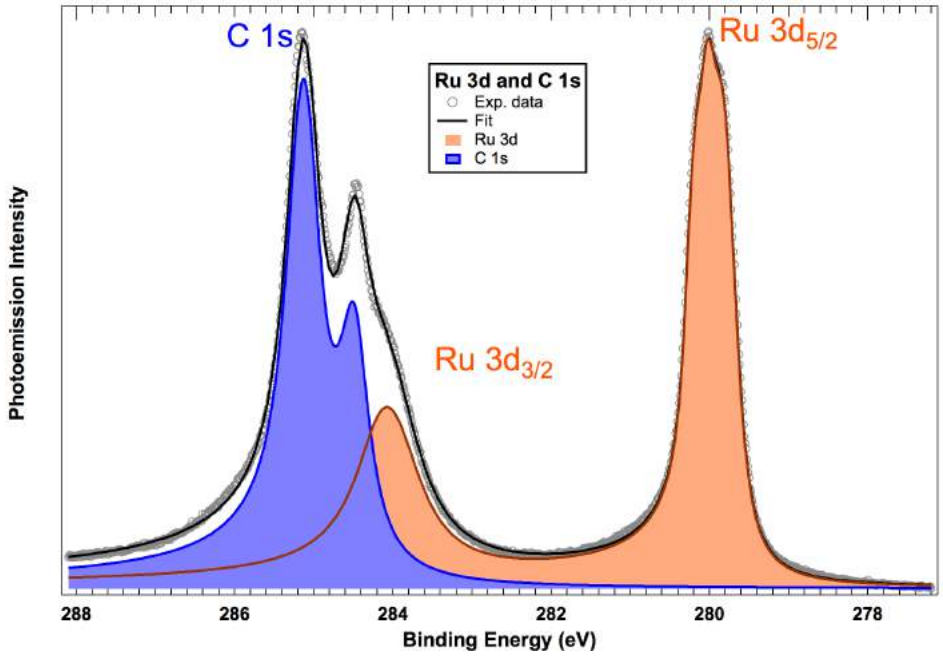

Figure 3.3: Ru 3d and C 1s high resolution photoemission spectrum acquired after Gr growth on Ru(0001) ($h\nu$=385 eV). Experimental data (gray dots) are displayed along with the best fit result (black line). The blue spectrum represents the C 1s core level of Gr, while the orange spectrum corresponds to the Ru 3d level.

analysis of the FWHM of Gr diffraction spots that, in both cases, the average Gr domain size is comparable to the transfer width of the instrument. In order to confirm whether or not the deposited metal had completely intercalated below graphene, we compared the C 1s spectra before and after the metal deposition. In fact, a completely intercalated metal layer is reflected in an intensity loss in the photoemission signal generated by the substrate, due to photoelectron shadowing, whereas the photoemission intensity of graphene remains constant. On other hand, if part of the metal atoms sit above graphene the photoemission intensity of graphene is shadowed as well. However, we did not observe any decrease in the overall C 1s spectral intensity (area under the C 1s lineshape) after Ir, Ru, and Co deposition, which indicates that, for these species, complete intercalation occurs. This was further confirmed by substrate core level spectra (not shown here). Small reduction of the graphene photoelectron intensity was observed only after deposition of Rh, suggesting that a small amount of the deposited Rh does not intercalate at 700 K, but rather form small aggregates above graphene. All the photoemission components of the C 1s core level which appear in any of the systems we analyzed are reported in Table 3.1, together with

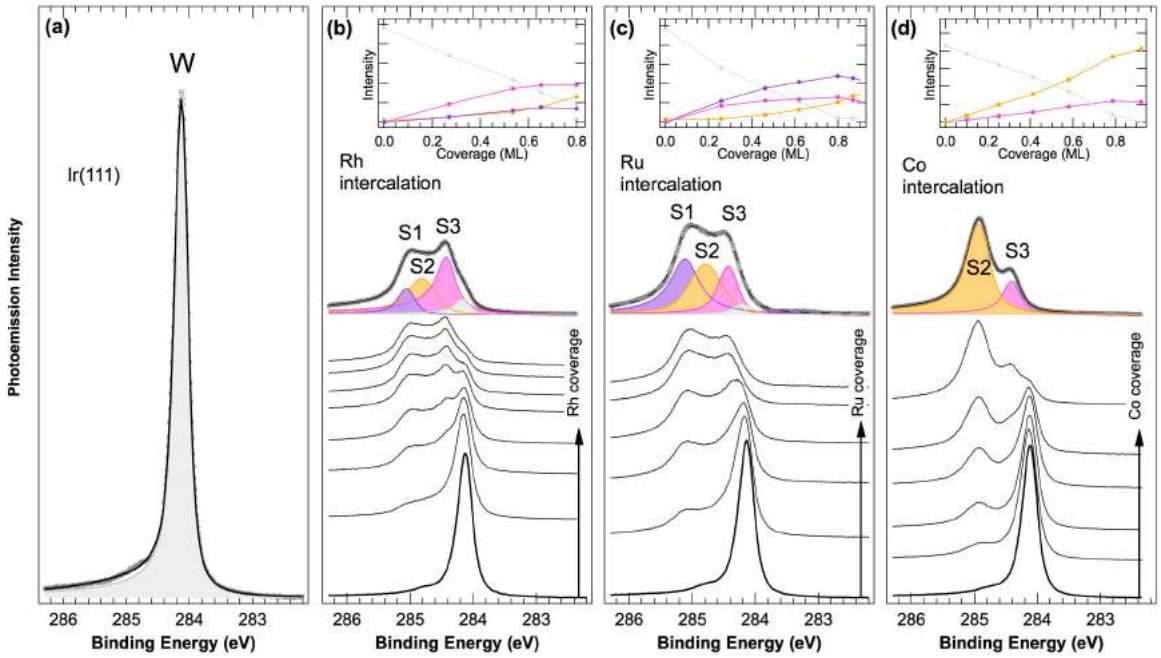

Figure 3.4: C 1s core level spectra of Gr/Ir(111) during intercalation ($h\nu$=385 eV). (a) Pristine Gr/Ir(111). (b-d) Evolution of the C 1s spectrum during intercalation of (b) Ru, (c) Rh and (d) Co. Top graphs show the evolution of the area of all C 1s photoemission components corresponding to non-equivalent C populations at increasing intercalating metal coverages.

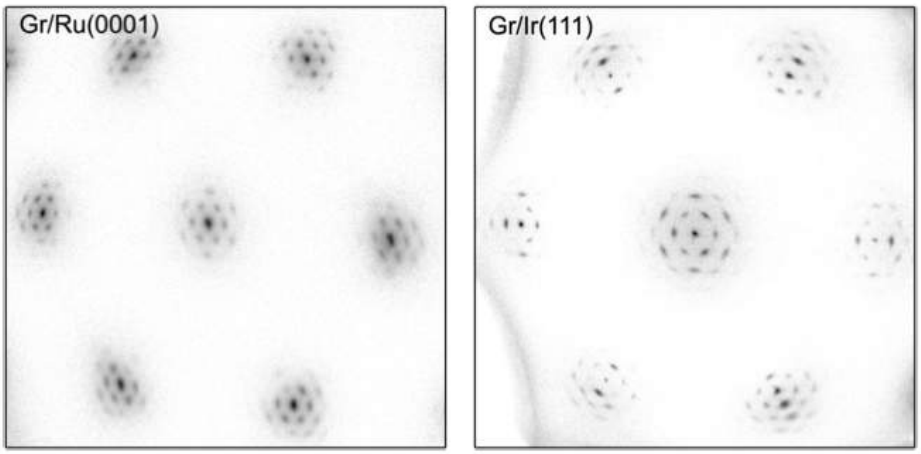

Figure 3.5: SPA-LEED diffraction patterns acquired after Gr synthesis on Ru(0001) (left, E=250 eV) and Ir(111) (right, E=110 eV).

their BEs. The error bars associated to all the systems (in table 3.1) are around 20 meV.

In the series of spectra acquired during each intercalation experiment, it is clear that the C 1s spectrum (Fig. 3.2 (b-d) and 3.4 (b-d)) changes dramatically as the substrate is covered by the intercalated species. In order to accurately analyze

System	S1 (eV)	S2(eV)	S3(eV)	W(eV)
GR/Ru(0001)	**285.13 eV**	-	284.47 eV	-
GR/Ir/Ru(0001)	-	284.89 eV	-	**284.23 eV**
GR/Rh/Ru(0001)	285.13 eV	284.91 eV	**284.47 eV**	-
GR/Co/Ru(0001)	-	**284.97 eV**	284.47 eV	-
GR/Ir(111)	-	-	-	**284.12 eV**
GR/Rh/Ir(111)	285.05 eV	284.83 eV	**284.42 eV**	-
GR/Ru/Ir(111)	**285.10 eV**	284.75 eV	284.41 eV	-
GR/Co/Ir(111)	-	**284.93 eV**	284.40 eV	-

Table 3.1: BE of each component of the C 1s core level photoemission spectrum in all systems studied in this work. The main component in the spectrum of each system is indicated in bold.

the data, we first obtained the line shape parameters (Γ, α, G) from the spectra acquired at the highest coverage of the intercalated species, and assumed that the line shape of each component (Γ, α) was constant throughout all the experiment, whereas the Gaussian parameter G was allowed to change, in order to describe possible contributions due to structural inhomogeneities. In this experiment quartz microbalance (QMB) was not available so the coverage of intercalated species were obtained by looking at the Ir $4f_{7/2}$ and Ru $3d_{5/2}$ spectra. In fact, these core levels show distinct spectral features for bulk and surface atoms, due to the different coordination. As the intercalation proceeds, the intercalated metal cover the substrate surface atoms, thus their local coordination environment becomes more and more bulk like. The intensity of the photoemission component generated by the under-coordinated surface atoms of the substrate I_S can be thus related to the coverage θ. In particular, neglecting border effects (which are only relevant at low coverages), the ratio between the area of this component after and before the intercalation is equal to the amount of surface not yet covered:

$$1 - \theta = \frac{I_S(\theta)}{I_S(\theta = 0)} \tag{3.1}$$

A more accurate estimation of coverage is based on the intensity of the photoelectron signal of the intercalated species I_I, which is proportional to the number of its atoms and therefore linearly increases with coverage. This is only valid as long as a single

layer is forming, as was the case for our experiment. As we are reaching 1 ML of intercalated species, the spectral intensity of the substrate surface atoms decreases and eventually vanishes. The intercalated species coverage can be calculated by following this approach as shown below:

$$\theta = 1 - \frac{I(\theta)}{I_0} \tag{3.2}$$

where $I(\theta)$ is the intensity of the surface spectral component at the coverage θ and I_0 is the initial intensity. Within this approximation we calculated the coverage of the intercalated metal that does not form three dimensional islands, but rather a single epitaxial layer.

For all the graphene/TM/Ir(111) systems (see Fig. 3.4 (b-d)) the W component intensity decreases upon intercalation and almost vanishes for higher coverage. On the other hand, several components appear at higher BE, indicating a stronger degree of interaction between Gr and the substrate. The BE of these components does not depend on the coverage, only the relative intensities being modified throughout the experiment. Specifically, after Rh intercalation, we observe a main component at 284.42 eV (S3) along with two additional components, with lower intensities, at higher BEs (S1–2) (see Table 3.1). It is noticeable that the BE of the S3 peak is quite similar for this system and for the low BE component of graphene grown on Rh(111), thus suggesting that this S3 component could arise at low BE from buckled areas of the graphene sheet after Rh intercalation. The component S1, on the other hand, is close in BE to the high BE component of graphene on Rh(111), and is most likely related to carbon atoms strongly interacting with the substrate. On the contrary the S2 component lying in between most probably arises from atoms in an intermediate configuration between the two and arises one side in case of Gr-Co and on other side may be arises from local defects upon intercalation.

A similar behaviour is observed upon intercalation of Ru on Ir(111) as shown in (Fig. 3.4 (c)), also in this case three components are observed lying between 284.41 and 285.10 eV. These components have BEs close to those found for the Rh intercalation. Their relative intensities, however, are different from the previous case, as the component at higher BE (S1) has a larger (almost double) spectral weight than the low BE one (S3): this could indicate, on average, a stronger interaction with the Ru layer than for the Rh layer. This can be interpreted in terms of a local

covalent bonding between Gr and the Ru & Rh, which proceeds through the orbital hybridization between the C $2p_z$ and the 3d states. The different electronic structures of Ru ($4d^7$ $5s^1$) and Rh ($4d^8$ $5s^1$) supports different Gr–metal binding. Besides the presence of the S2 component, the spectral distribution is quite similar to the one obtained for graphene directly grown on Ru(0001) (Fig. 3.2 (a)). With the Co evaporation on Ir(111), we obtained a large component (S2) at 284.93 eV, and a weaker one (S3) at lower BE (Table 3.1), which indicates a strong interaction with the Co layer. We notice that the C 1s core electrons of graphene (and therefore also its interaction with the substrate) in the intercalation experiments on Ir(111), shows significant changes depending on the chemical composition of the substrate. Specifically, the interaction increases when passing from Ir to Rh, Ru and finally Co, which presents, on average, the strongest interaction with graphene among all the systems being studied.

On the other hand, we observed a very different behaviour for the experiments performed on Ru(0001) depending upon the element being intercalated. For Ir intercalation as shown in (Fig. 3.2 (b)), we notice a weakening of the component S1, which almost completely disappears, while another weak component is present at lower BE (S2). The intensity of component S3, increases until it becomes dominant and its BE moves linearly towards lower values, reaching 284.23 eV at a coverage of 0.8 ML (see Table 3.1). At this point, the spectrum resembles quite a lot the spectrum of graphene grown on Ir(111) and the dominant component is similar to the W component of latter system. This change in BE can be attributed to a smooth modification of the properties of graphene, from few-atom buckling above Ru(0001) towards a completely raised, weakly interacting graphene above the intercalated Ir layer. We believe that the S2 component arises due to the local defects and inhomogeneities in the distribution of the Ir atoms. In case of Rh intercalation on Ru(0001) (Fig. 3.2 (c)) we observe an increase in the low BE component (S3) along with two weaker components (S1–2) at higher BE (Table 3.1). There isn't significant change in the BE of any component, thus indicating that the modifications are limited to a change in populations of weakly and strongly interacting atoms. With Co intercalation on Ru(0001) the higher BE component (S1) is replaced by a new one (S2), at a slightly lower BE (Table 1) as shown in Fig 3.2 (d). These two component (S1 & S2) remain

distinct and at constant binding energy with increasing Co coverage. On the other hand, the low-BE component (S3) decreases: in general the spectral weight moves towards higher BE, indicating a slightly stronger interaction of graphene with Co than with Ru.

In conclusion, we observed that for the two intercalation experiments on Ir(111) and Ru(0001): the C 1s spectrum of graphene (for its interaction with the substrate) varies greatly depending upon the chemical composition of the topmost surface layer. A similar spectral behavior is observed for the same Gr/TM interface, regardless of the substrate composition. Particularly, the graphene/Ir interface appears to be the most weakly interacting among all investigated systems, followed by Rh and Ru, while the Co interactions with graphene is stronger than Ru.

3.2.2 Theoretical results

Figures 3.6 and 3.7 report the DFT computed minimum-energy geometric configuration for all the systems studied in this experiment. The color scale indicates the distance (z) of each carbon atom from the surface plane of the metallic substrate. The metallic substrate itself is actually slightly corrugated when it interacts strongly with graphene. This corrugation, however, is an order of magnitude lower than that of graphene. For this reason, the distance has been referred to the mean vertical position of all atoms composing the metallic surface.

For all the systems, graphene's properties strongly depend on the chemical composition of the topmost layer of the substrate. In particular, where the top most layer consists of Ir (Figs. 3.6 and 3.7 (a)), the distance between graphene and the substrate is larger than 4 Å, and the former has a very small corrugation. This is in contrast with all other systems, where the distribution is much wider, with the nearest atoms closer than 2 Å to the surface and the farthest between 3.4 and 3.9 Å. For all systems, the unit cells of graphene whose atoms are farthest from the surface are those where the centre of the honeycomb lies in an on-top site of the substrate, and therefore both atoms lie in hollow sites. On the other hand, the cells closest to the substrate are those where the centre of the honeycomb lies in bridge sites, and both C atoms lie above a metallic atom.

In particular, for the Gr/Rh/Ru(0001) and Gr/Rh/Ir(111) systems we ob-

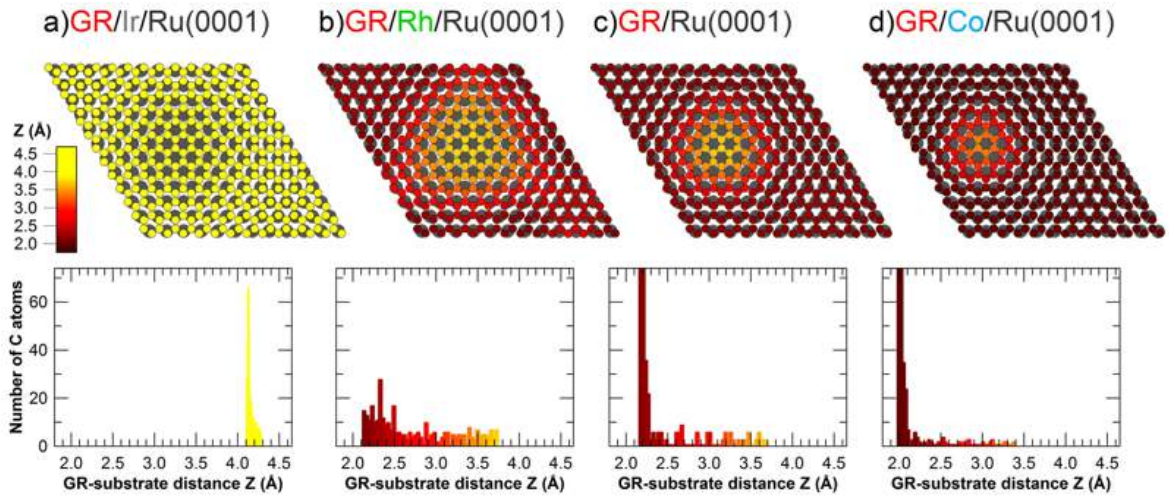

Figure 3.6: DFT results for different Gr/TM/Ru(0001) interfaces. Top panels: geometric configuration of the topmost metallic atoms (large, gray circles) and of the graphene atoms (smaller, colored circles) inside the (12×12) moiré unit cell used for calculations. The color scale indicates the C-to-surface distance (z). Bottom panels: distribution of distance z for all the C atoms in the moiré unit cell.

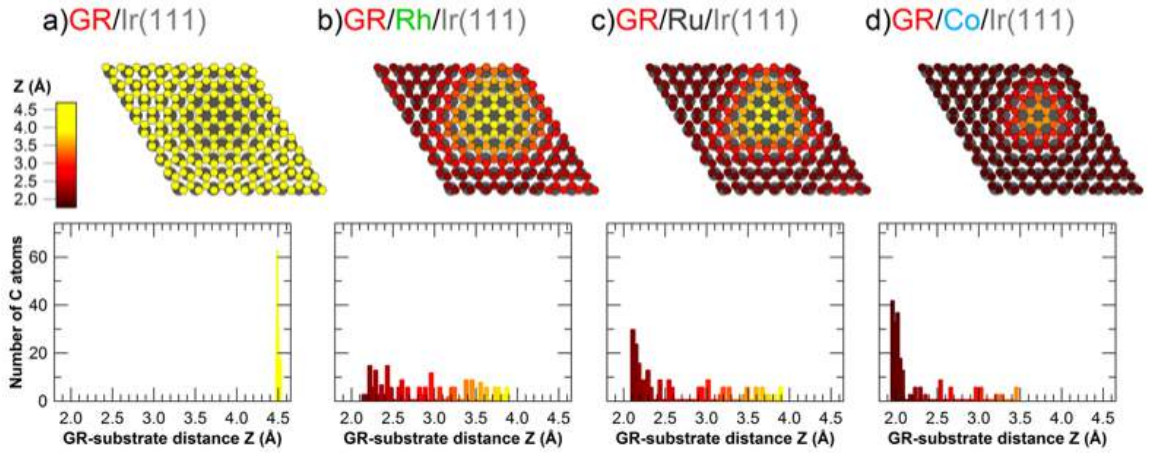

Figure 3.7: DFT results for different Gr/TM/Ir(111) interfaces. Top panels: geometric configuration of the topmost metallic atoms (large, gray circles) and of the graphene atoms (smaller, colored circles) inside the (9×9) moiré unit cell used for calculations. The color scale indicates the C-to-surface distance (z). Bottom panels: distribution of distance z for all the C atoms in the moiré unit cell.

serve a quite uniform distribution in the Gr-surface distance, which ranges from 2.1 to 3.9 Å in the case Gr/Rh/Ru(0001) (Fig. 3.6 (b)), and from 2.1 to 3.7 Å for Gr/Rh/Ir(111) (Fig. 3.7 (b)), suggesting a smooth corrugation of the Gr layer in these cases.

In the case of graphene/Ru interfaces most of the C atoms lie at a small distance from the substrate (between 2.1 and 2.3 Å). The others, which are more than 25% in the case of graphene/Ru(0001) and almost 50% for graphene/Ru/Ir(111), found at a higher distance, up to 3.7 and 3.9 Å respectively (Fig. 3.6 and 3.7 (c)). The higher number of C atoms which lie close to the surface with respect to the Gr/Rh case indicates an average stronger interaction, in agreement to what deduced from the C 1s core level spectra analysis.

Finally, the distribution along z of the C atoms of graphene above a Co layer (Fig. 3.6 and 3.7 (d)) has a very sharp peak at low z values (between 1.9 and 2.1 Å), with only few atoms lying farther than 2.1 Å from the surface (and up to 3.5 Å). This observation supports the hypothesis, based on XPS data, that the average graphene-surface interaction is stronger for Co with respect to the other investigated systems.

The calculated distance distribution for the two graphene/Ru interfaces is in good agreement with experimental values found for Gr grown on Ru(0001) [24]. This is also the case for graphene sitting on intercalated Co on Ir(111), which is in very good agreement with previous experiments on the same system [25]. Further, the z value of about 2 Å found for the majority of atoms in both systems corresponds to the height found for graphene above Co(0001), where Gr matches the lattice of the surface forming a 1×1 commensurate structure [26]. The two graphene/Rh interfaces have the same corrugation as graphene synthesized on pristine Rh(111) [27]. The separation of Gr from Ir for the two graphene/Ir systems appears instead to be overestimated, being even larger than the inter-layer distance of graphite by about 1 Å. This can be attributed to the presence of dispersive forces which are not included in the present calculations [28] and which are probably not negligible in this case.

In order to get insight on the electronic configuration of different Gr/transition metals interfaces we also computed the core level BEs for all C atoms of all the systems. Since such theoretical methods only provide the relative value of the C 1s BEs for non equivalent atoms, we had to align the theoretical BE scale to the experimental one. Firstly, in order to meet this prerequisite, we aligned the center of the calculated BE distribution for graphene/Ir(111) to the actual experimental value,

and then shifted the theoretical BE scale for all systems by the same offset. The graphene/Ir(111) system was chosen because it displays both the narrowest C 1s experimental spectrum and theoretical BE distribution, thus minimizing the error in the alignment.

The C 1s core level BEs for the C atoms inside the moiré unit cell for the investigate systems are computed by DFT and reported in Figs. 3.8 and 3.9. A different behavior of the C 1s BE distribution can be observed for different chemical compositions of the substrate's topmost layer, regardless of its geometry. Graphene lying on top of Ir has a narrow BEs distribution centered at about 284.20 eV for Gr/Ir(111) (Fig. 3.9 (a)) and at about 284.27 eV for the intercalated systems (Fig. 3.8 (a)), in good agreement with what we found in the experimental XPS data which shows a main component (W) at 284.12 and 284.23 eV BE respectively.

On the other hand, the BE distribution is much wider for other investigated system (Rh, Ru, Co). The calculated BEs for the Ru, Rh, and Co interfaces range from about 284.4 eV up to 285.5 eV in some systems like Gr/Ru/Ir(111). What differs among these corrugated systems, however, is the shape of the distribution, which is different depending on the topmost metallic layer. For both Gr/Rh and Gr/Ru system (Figs. 3.8 and 3.9 (b,c)) the C atoms display a narrow distribution with similar BE range. A higher density of C atoms with higher BE is observed for Ru, again suggesting that the interaction of Gr with the substrate is, on average, stronger for Ru with respect to Rh. This is in good agreement with the experimental results. Finally, the BE distribution for C atoms belonging to graphene lying above Co have a sharp peak centred at around 285.20 eV, with only around 15% of the C atoms having a C 1s BE lower than 284.7 eV.

As it can be observed from the graphs in the Figs. 3.8 and 3.9 there is usually a correlation between the distance of each C atom from the underlying surface and its C 1s BE, with the latter decreasing as the former increases. This situation is more complex for graphene/Rh system, where some adjacent atoms, despite being at the same distance (about 2.5 Å) from the substrate, show a large difference (up to 500 meV) in the C 1s BE. In this case, in fact, the energy of each atom is related to the site it occupies on the surface: in particular, the BE is maximum for atoms occupying on-top or bridge sites and minimum for threefold hollow sites. This particular behaviour

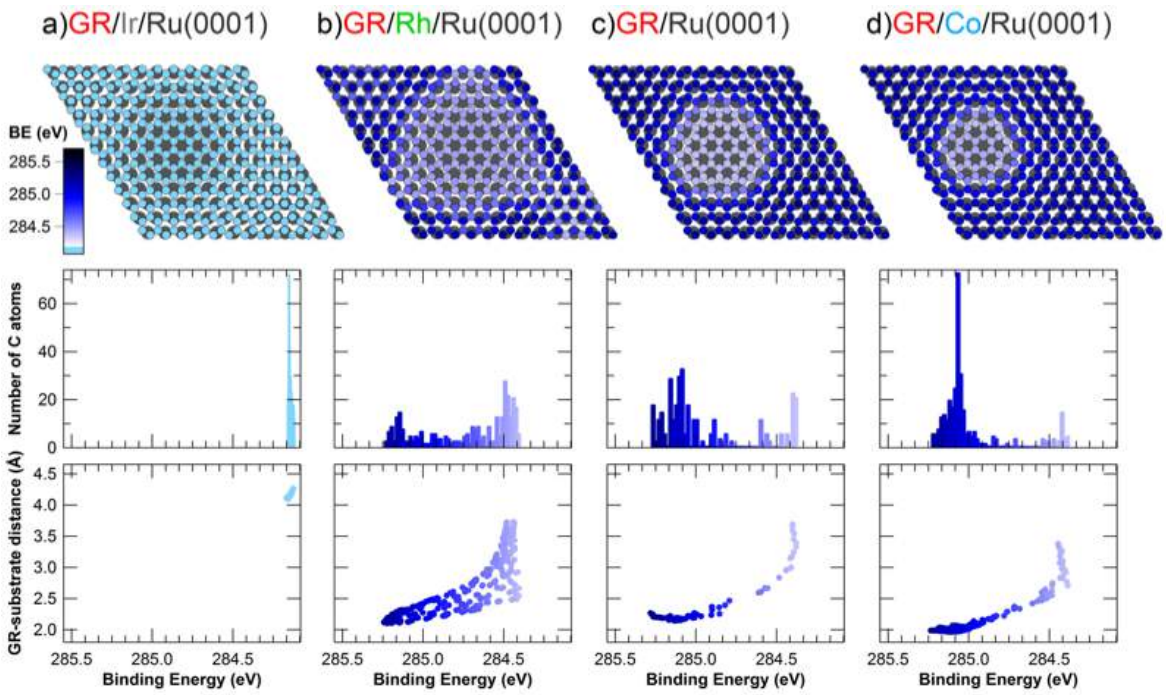

Figure 3.8: DFT results for different Gr/TM/Ru(0001) systems. Top panels: the calculated C 1s core level BE is represented for each C atom (small dots) in the moiré cell using a color scale. The larger, gray circles represent the underlying metallic atoms. Middle panels: Distribution of BEs for all C atoms. Bottom panels: correlation between C 1s BE and separation of each atom from the topmost metallic layer.

has already been observed for epitaxial graphene on Rh(111) and has been explained in terms of hybridization of the π states of graphene with the d bands of Rh [29]. This dependence of the BE on the site is weaker for atoms either too close to the surface (around 2 Å) or too far (above 3 Å).

The similarity between the histograms representing the theoretically calculated C 1s BE distribution and the measured XPS spectra for each of the systems studied in this work underlines the accuracy and validity of the calculations. In order to further confirm the agreement between the experimental C 1s core level spectra and the DFT computed C 1s BEs, we compared the barycenter of each calculated BE distribution with that of the corresponding experimental spectrum. The results are reported in Fig. 3.10, where the experimental and theoretical C 1s barycenter are plotted together versus the calculated d-band center of the topmost metallic layer. In order to achieve this with the best possible accuracy, we calculated it for all the coverages up to a monolayer and then used the value obtained through a

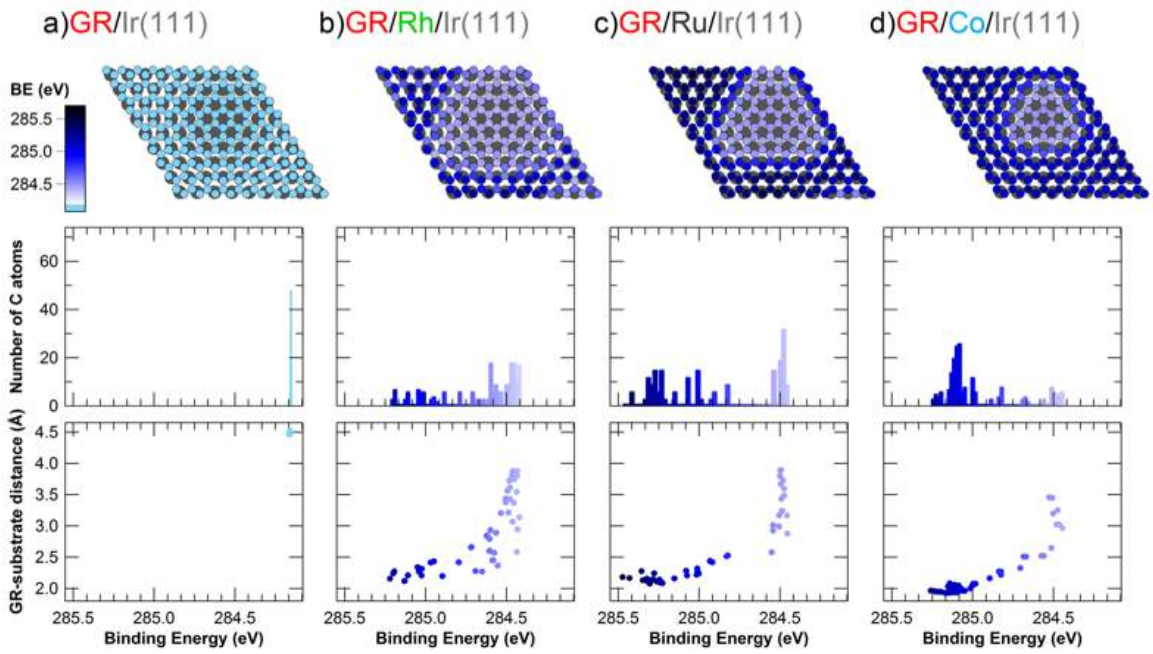

Figure 3.9: DFT results for different Gr/TM/Ir(111) systems. Top panels: the calculated C 1s core level BE is represented for each C atom (small dots) in the moiré cell using a color scale. The larger, gray circles represent the underlying metallic atoms. Middle panels: Distribution of BEs for all C atoms. Bottom panels: correlation between C 1s BE and separation of each atom from the topmost metallic layer.

linear fit. In most systems, the experimental C 1s spectrum barycenter value (round markers) agrees with the calculated ones (square markers), within an uncertainty of 40 meV. The only cases where we found a slightly worse agreement were the Gr/Rh systems and the one obtained by intercalating Ru at the Gr/Ir(111) interface. These systems were characterized by a higher disorder. In particular, in the first two cases, the reason can be ascribed to the fact that a small portion of Rh atoms were not completely intercalated, but most likely formed clusters on the graphene surface. We found a very good agreement between experiment and theory, showed a strong linear relationship between C 1s spectral center of mass and calculated d-band centers. As initially, pointed out by Wang [29] and more recently extensively described by Toyoda [30], the interaction between the d-band of transition metals and graphene potential energy surface strongly influence the adsorption properties of graphene. We know that the core level BEs are affected by final-state contributions that are intrinsic to the photoemission process but their contribution does not obscure this linear relationship. This offers a further proof that core level spectroscopy can be

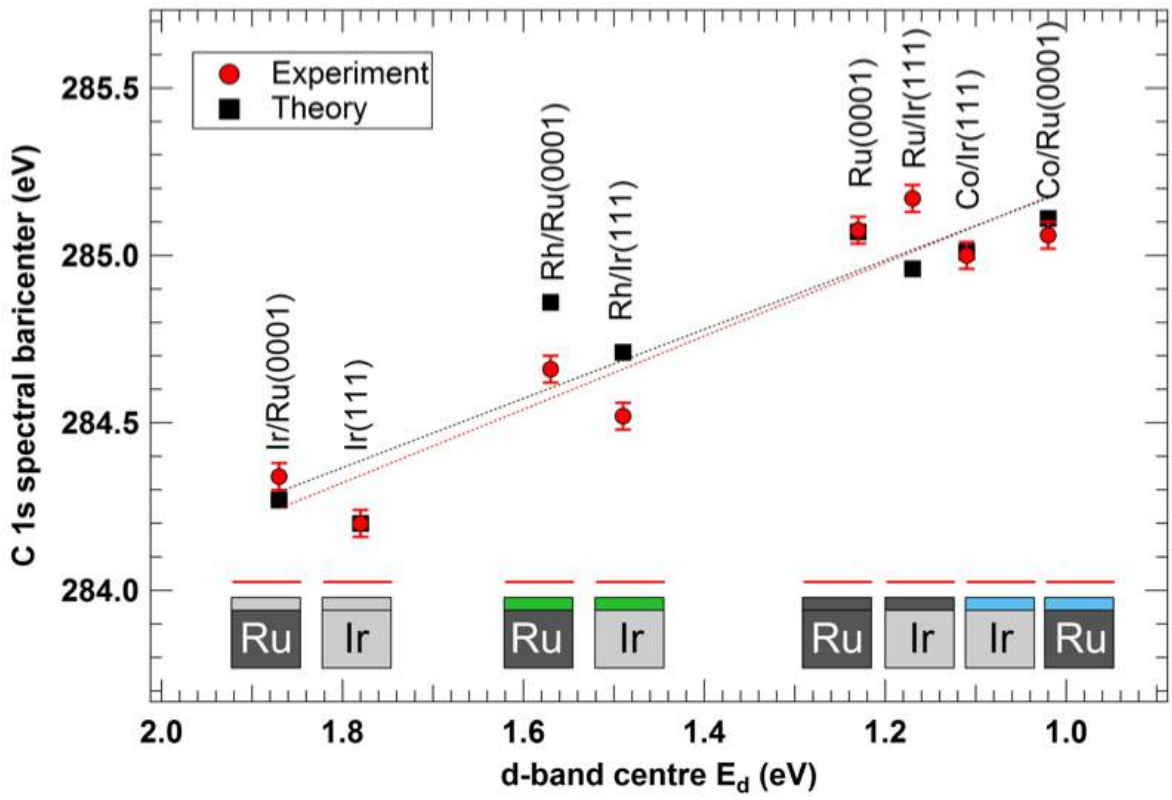

Figure 3.10: Theoretical (black squares) and experimental (red circles) values of the C 1s core-level BE distribution's barycentre of all C atoms in the moiré unit cell, for each system studied in this work, versus the calculated d-band centre of the underlying clean metal surface.

considered a useful experimental descriptor of the interaction strength of graphene with transition metal surfaces.

In order to finalize the characterization of the studied systems, the theoretical simulations also allow us to compute the average distance of each C atom from three nearest neighbors of all studied systems, as shown in Fig. 3.11 and 3.12. This C-C distance distribution inside the moiré cell is one of the parameters influenced by geometry: since the moiré unit cell is preserved in the intercalation process, the average separation between C atoms is larger (by around 0.02 Å) in systems having the moiré unit cell of graphene/Ru(0001) than in systems having the moiré unit cell of graphene/Ir(111).

This nearest neighbor distance could be due to the fact that the interaction of graphene/Ru(0001) induces a strain in the graphene layer in order to form a commensurate moiré lattice. On the other hand, for graphene/Ir(111) the interaction

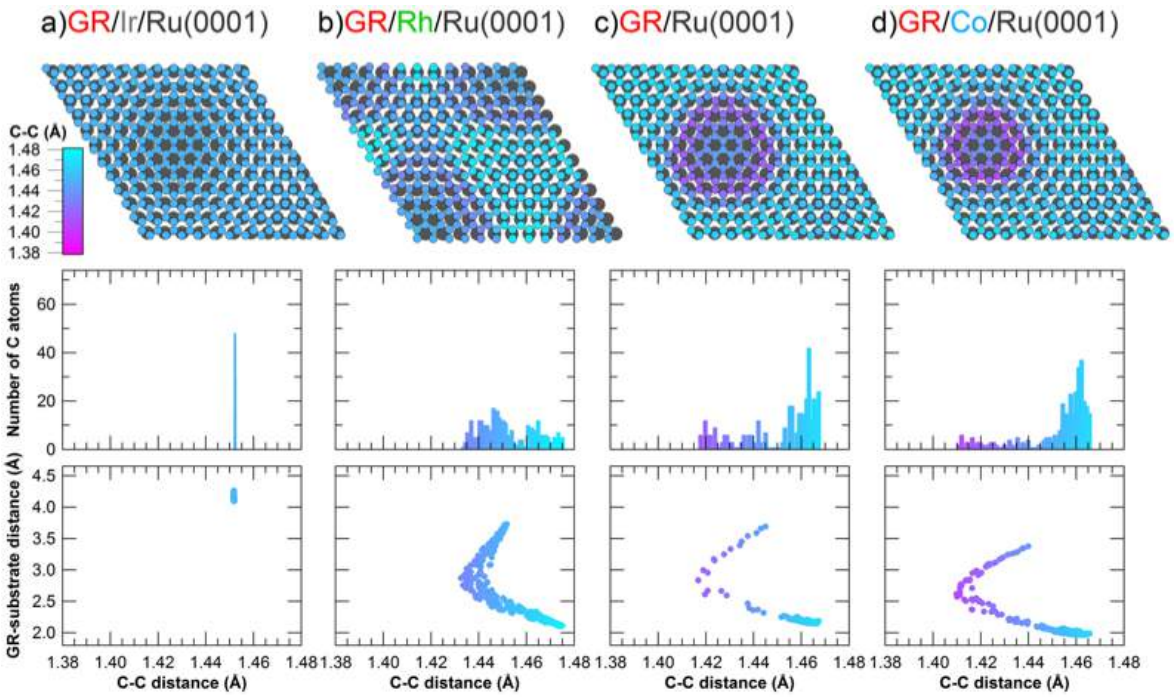

Figure 3.11: DFT results for different Gr/TM/Ru(0001) systems. Top panels: geometric configuration of the topmost metallic atoms (large, gray circles) and of the graphene atoms (smaller, colored circles) inside the moiré cell. The color scale indicates the average distance of each C atom from its three nearest neighbors. Middle panels: Distribution of C-C distances of all C atoms. Bottom panel: correlation between C-C distance and separation of each atom from the topmost metallic layer.

with the substrate is too weak to significantly modify the geometry of graphene. The geometrical arrangement of graphene is preserved upon intercalation, otherwise it would require breaking or a strong rippling of the in plane C-C bonds. Due to these reasons, in all systems modelled of Ru(0001) the distribution of C-C distances is shifted towards higher values with respect to that of the systems modelled on Ir(111). This could induce a small difference in the C 1s BEs for the same chemical composition of topmost layer.

The C-C distance of corrugated systems shows a broader distribution. As it is reported in Fig. 3.11 and 3.12 (b), the C-C distance shows a distribution ranging from 1.41 to 1.45 Å in the case of Ir(111), while for Ru(0001) it ranges form 1.43 to 1.48 Å. The modelled systems for graphene on Ru and Co shows similar C-C distance distribution with sharp peak at higher values. Moreover, the nearest neighbor distance on average is larger than for Ru(0001) based geometries.

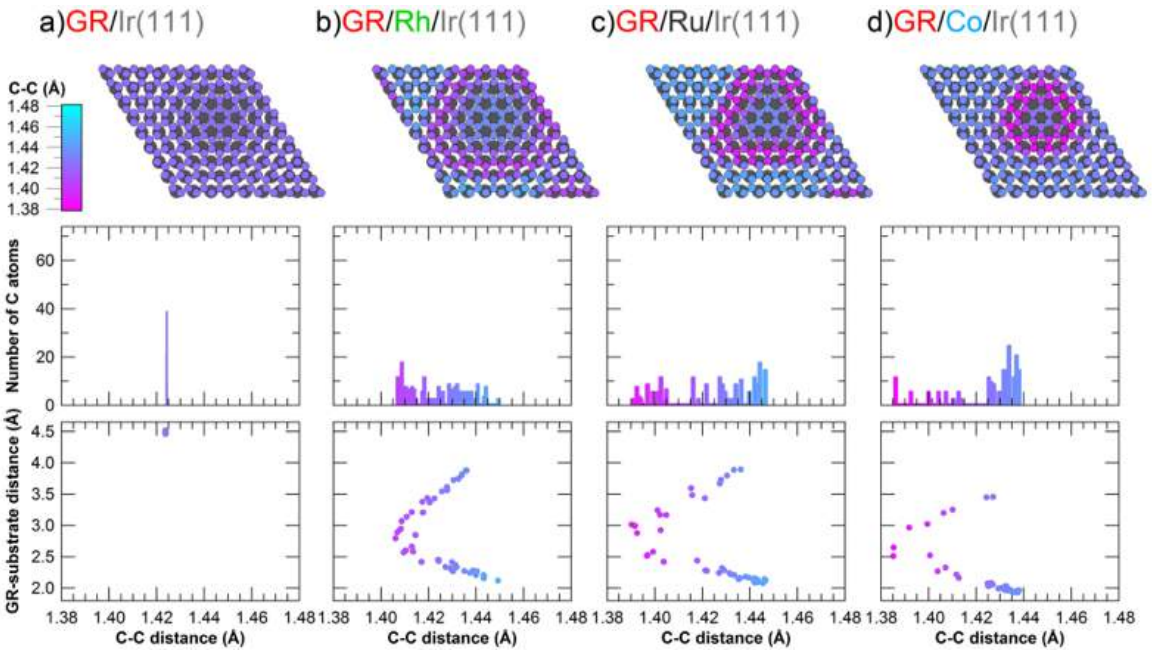

Figure 3.12: DFT results for different Gr/TM/Ir(111) systems. Top panels: geometric configuration of the topmost metallic atoms (large, gray circles) and of the graphene atoms (smaller, colored circles) inside the moiré cell. The color scale indicates the average distance of each C atom from its three nearest neighbors. Middle panels: Distribution of C-C distances of all C atoms. Bottom panel: correlation between C-C distance and separation of each atom from the topmost metallic layer.

The position inside the moiré cell (see Fig. 3.11 and 3.12, top panel) and the distance from the substrate shown in Fig. 3.11 and 3.12, bottom panel were obtained by the studying the correlation between the C-C separation. It can also be seen that the C-C distance is larger in the flat areas on top and also at the bottom of the valleys, while this distance is minimum on the edges of the hills. This effect demonstrates that the interaction between graphene and metal surfaces depends on the hybridization between the π_z orbitals of graphene and the d-band of the substrate [31].

We can conclude that graphene/metal interaction strength is mainly driven by the chemical composition of the interface. It is clear from the comparison of the data obtained in the different intercalation experiments, that there are major differences in the geometric and electronic properties of the graphene layer among systems with a different chemical species at the interface, regardless of the substrate. For instance, the intercalation of Ir on graphene/Ru(0001) leads to a very weakly interacting graphene, as for graphene/Ir(111), while intercalation of Ru below

graphene/Ir(111) leads to stronger interaction with the substrate, resulting in a buckling of the graphene layer. These results provide us ample evidence that the key role in determining the strength of interaction is played by the chemical composition of the substrate. On the other hand, geometry mainly determines the periodicity of the moiré, which is preserved after intercalation. It is particularly obvious if we consider the case of graphene interacting with Co that is flat and commensurate on Co(0001), while buckled in the case of the Co intercalation. Further, the substrate strongly affect the local arrangements of C atoms inducing a different degree of strain depending on the substrate lattice. We have also verified that the C 1s spectral barycentre has a linear relationship with the d-band center position, which is recognized to strongly influence the coupling between graphene and the metal surface. Therefore, we have demonstrated that C 1s core level spectra contain relevant information on graphene/metal interfaces and can be considered a reliable descriptor of interaction strength of the graphene/substrate.

Further, this combined experimental and theoretical studies gives us insight into the Gr/substrate interaction. These results showed that the Ir(111) substrate is very weakly interacting with graphene among all the system studied. Therefore, the most suitable TM-metal substrate to study the properties of clusters on Gr is the Gr/Ir(111) interface, where the clusters would not lose much of their individual character due to the corrugation of carbon layer and its very weak interaction with the substrate. The Ir(111) substrate gives us best template for the growth of well ordered metallic-cluster without changing their intrinsic properties. This study was useful to choose a desirable metal-substrate (Ir(111)) to grow Gr to support the metal or oxide clusters presented in the next chapters.

Bibliography

[1] G. Giovannetti, P. Khomyakov, G. Brocks, V. Karpan, J. Van Den Brink, and P. Kelly. *Doping graphene with metal contacts.* Physical Review Letters, 101(2):026803, 2008.

[2] A. Varykhalov, M. Scholz, T. Kim, and O. Rader. *Effect of noble-metal contacts on doping and band gap of graphene.* Physical Review B, 82(12):121101, 2010.

[3] B. Schultz, C. Jaye, P. Lysaght, D. Fischer, D. Prendergast, and S. Banerje. *On chemical bonding and electronic structure of graphene–metal contacts.* Chemical Science, 4(1):494–502, 2013.

[4] A. Preobrajenski, M. Ng, A. Vinogradov, and N. Mårtensson. *Controlling graphene corrugation on lattice-mismatched substrates.* Physical Review B, 78(7):073401, 2008.

[5] M. Batzill. *The Surfurface Science of graphene: metal interfaces, CVD synthesis, nanoribbons, chemical modifications, and defects.* Surface Science Reports, 67(3-4):83–115, 2012.

[6] C. Busse, P. Lazić, R. Djemour, J. Coraux, T. Gerber, N. Atodiresei, V. Caciuc, R. Brako, A. T. N'Diaye, S. Blügel, J. Zegenhagen, and T. Michely. *Graphene on Ir(111): physisorption with chemical modulation.* Physical Review Letters, 107(3):036101, 2011.

[7] P. Sutter, J. Sadowski, and E. Sutter. *Graphene on Pt(111): growth and substrate interaction.* Physical Review B, 80(24):245411, 2009.

[8] S. Marchini, S. Günther, and J. Wintterlin. *Scanning tunneling microscopy of graphene on Ru(0001).* Physical Review B, 76(7):075429, 2007.

[9] B. Wang, M. L. Bocquet, S. Marchini, S. Günther, and J. Wintterlin. *Chemical origin of a graphene moiré overlayer on Ru(0001).* Physical Chemistry Chemical Physics, 10(24):3530-4, 2008.

[10] D. Alfè, M. Pozzo, E. Miniussi, S. Günther, P. Lacovig, S. Lizzit, R. Larciprete, B. S. Burgos, T. O. Menteş, A. Locatelli and A. Baraldi. *Fine tuning of graphene–metal adhesion by surface alloying.* Scientific Reports, 3:2430, 2013.

[11] E. Miniussi, M. Pozzo, A. Baraldi, E. Vesselli, R. R. Zhan, G. Comelli, T. O. Menteş, M. A. Niño, A. Locatelli, S. Lizzit, and D. Alfè. *Thermal stability of corrugated epitaxial graphene grown on Re(0001).* Physical Review Letters, 106(21):216101, 2011.

[12] E. Miniussi, M. Pozzo, T. O. Menteş, M. A. Ninõ, A. Locatelli, E. Vesselli, G. Comelli, S. Lizzit, D. Alfè, and A. Baraldi. *The competition for graphene formation on Re (0001): a complex interplay between carbon segregation, dissolution and carburisation.* Carbon, 73:389–402, 2014.

[13] J. Wintterlin, and M-L. Bocquet. *Graphene on metal surfaces.* Surface Science, 603(10-12):1841–52, 2009.

[14] O. Bikondoa, G. R. Castro, X. Torrelles, F. Wendler, and W. Moritz. *Surface-induced disorder on the clean $Ni_3Al(111)$ surface.* Physical Review B, 72(19):195430, 2005.

[15] F. Presel, N. Jabeen, M. Pozzo, D. Curcio, L. Omiciuolo, P. Lacovig, S. Lizzit, D. Alfé, and A. Baraldi. *Unravelling the roles of surface chemical composition and geometry for the graphene–metal interaction through C1s core-level spectroscopy.* Carbon, 93:187–198, 2015.

[16] J. Coraux, A. T. N'Diaye, C. Busse, and T. Michely. *Structural coherency of graphene on Ir (111).* Nano Letters, 8(2):565–570, 2008.

[17] A. T. N'Diaye, S. Bleikamp, P. J. Feibelman, and T. Michely. *Two-dimensional Ir cluster lattice on a graphene moiré on Ir(111).* Physical Review Letters, 97(21):215501, 2006.

[18] R. Larciprete, S. Ulstrup, P. Lacovig, M. Dalmiglio, M. Bianchi, F. Mazzola, L. Hornekær, F. Orlando, A. Baraldi, Ph. Hofmann, and S. Lizzit. *Oxygen switching of the epitaxial graphene–metal interaction.* ACS Nano, 6(11):9551–9558, 2012.

[19] S. Günther, S. Danhardt, B. Wang, M. L. Bocquet, S. Schmitt, and J. Wintterlin. *Single terrace growth of graphene on a metal surface.* Nano Letters, 11(5):1895–1900, 2011.

[20] C. Vo-Van, S. Schumacher, J. Coraux, V. Sessi, O. Fruchart, N. Brookes. *Magnetism of cobalt nanoclusters on graphene on iridium.* Applied Physics Letters, 99(14):142504, 2011.

[21] A. Cavallin, M. Pozzo, C. Africh, A. Baraldi, E. Vesselli, C. Dri, G. Comelli, R. Larciprete, P. Lacovig, S. Lizzit, and D. Alfè. *Local electronic structure and density of edge and facet atoms at Rh nanoclusters self-assembled on a graphene template.* ACS Nano, 6(4):3034–43, 2012.

[22] S. Vlaic, A. Kimouche, J. Coraux, B. Santos, A. Locatelli, and N. Rougemaille. *Cobalt intercalation at the graphene/ iridium(1 1 1) interface: influence of rotational domains, wrinkles, and atomic steps.* Applied Physics Letters, 104(10):101602, 2014.

[23] S. Lizzit, A. Baraldi, Ch. Grütter, J. H. Bilgram, and Ph. Hofmann. *The surface phase transition and low-temperature phase of αGa(010) studied by SPA-LEED.* Surface Science, 603(21):3222–3226, 2009.

[24] W. Moritz, B. Wang, M. L. Bocquet, T. Brugger, T. Greber, J. Wintterlin, and S. Günther. *Structure determination of the coincidence phase of graphene on Ru(0001).* Physical Review Letters, 104(13):136102, 2010.

[25] D. Pacilé, S. Lisi, I. Di Bernardo, M. Papagno, L. Ferrari, M. Pisarra, M. Caputo, S. K. Mahatha, P. M. Sheverdyaeva, P. Moras, P. Lacovig, S. Lizzit, A. Baraldi, M. G. Betti, and C. Carbone. *Electronic structure of graphene/Co interfaces.* Physical Review B, 90(19):195446, 2014.

[26] D. Eom, D. Prezzi, K. T. Rim, H. Zhou, M. Lefenfeld, S. Xiao, C. Nuckolls, M. S. Hybertsen, T. F. Heinz, and G. W. Flynn. *Structure and elec- tronic properties of graphene nanoislands on Co(0001).* Nano Letters, 9(8):2844–2848, 2009.

[27] E. Voloshina, and Y. Dedkov. *Graphene on metallic surfaces: problems and perspectives.* Physical Chemistry Chemical Physics, 14(39):13502– 13514, 2012.

[28] I. Hamada, and M. Otani. *Comparative van der Waals density-functional study of graphene on metal surfaces.* Physical Review B, 82(15):153412, 2010.

[29] B. Wang, M. Caffio, C. Bromley, H. Fruchtl, and R. Schaub. *Coupling epitaxy, chemical bonding, and work function at the local scale in transition metal-supported graphene.* ACS Nano, 4(10):5773–5782, 2010.

[30] K. Toyoda, K. Nozawa, N. Matsukawa, and S. Yoshii. *Density functional theoretical study of graphene on transition-metal surfaces: the role of metal d-band in the potential-energy surface.* The Journal of Physical Chemistry C, 117(16):8156–8160, 2013.

[31] B. Hammer, and J. K. Nørskov. *Theoretical surface science and catalysis calculations and concepts.* Advances in Catalysis, 45:71–129, 2000.

Chapter 4

Graphene supported metal oxide-nanoclusters

In recent years, the fabrication, the properties and the technological application of nanometer sized metal clusters have been the focus of intense research in different fields of nanotechnology. One of the major advantages of a nanomaterial can be found in its size: as it decreases down to the nanoscale, quantum-size and surface effects become dominant in changing their physical and chemical properties with respect to bulk materials counterparts [1, 2, 3, 4]. Due to the growing concern about global warming and the depletion of hydrocarbons resources, the development of renewable energy production and storage technologies represents one of the major scientific challenges of the 21^{st} century [5, 6]. A critical element in the pursuit of this quest is the discovery of efficient and cost effective catalysts to use in the electrochemical energy conversion process [5, 6], such as in the oxygen evolution reactions (OER) and in the oxygen reduction reaction (ORR). The synthesis of these new materials is essential to improve the efficiencies of direct solar and electro-catalytic water splitting devices [7, 8], fuel cells and metal air batteries [9, 10]. Due to the high cost of Pt and its declining activity over the period of time, alternative catalysts based on non-precious metals [11, 12] have been extensively investigated.

As already discussed in the introduction of this thesis, a number of studies have shown [13, 14] that the efficiency of such catalysts can be increased by quantum-confinement (for band alignment of Co-oxide nanocluster with water redox potentials) and intimate integration of a suitable support (to reduce water splitting

back reactions) [15, 16]. In this context, epitaxial Gr has emerged in recent years as an excellent candidate for the supported growth of transition metal nanoclusters and for the formation of long-range-ordered superstructures [17, 18, 19, 20, 21, 22]. The moiré lattice formed by Gr on lattice–mismatched transition metals, in fact, has a natural corrugation which enables the deposited clusters to arrange themselves into extended and periodic superlattices. As already reported in Chapter 3, the Gr/Ir(111) system is the right choice because it act as a versatile template for the growth of metallic cluster lattices.

To develop an efficient supported catalyst, it is highly recommended to understand particle size distribution, morphology as well as surfaces and interfaces structure. In this contest, the interest has recently emerged in the catalytic properties of cobalt and cobalt-containing oxides due to the low cost of the raw material with respect to other transition metals and their appealing multifunctional properties of technological interest [23, 24]. Studies have revealed that the activity of Co-oxides in heterogeneous catalysis is highly dependent upon particle size [25, 26], support effects [27] and preparation methods [28, 29]. However, the origins of these effects are not yet fully understood. For a better understanding we need to develop strategies for the production of Co-nanomaterials with desired features, in particular with specific oxidation state, structure, and interaction with the support. In this regards, the first part of this chapter is focused on design and preparation of Co-oxide nanoclusters supported on Gr/Ir(111) with the aim to find possible applications in the field of clean H_2 production.

The second part of this chapter is devoted to the growth and characterization of new Ti-oxide/graphene interfaces. The main reason for studying Ti-oxide is to gain detailed understanding of fundamental aspects of its surfaces and interfaces. We believe that an in depth understanding of the structural and chemical properties can help to improve materials for technological application in the field of catalysis. Indeed, titanium dioxide (TiO_2) is well known since 1970's for its photocatalytic activity for hydrogen production from water [30]. However, pure TiO_2 has rather a low activity towards photocatlytic water splitting due to the electron-hole recombination process. Here we design a new architecture of TiO_2 supported on Gr/Ir(111), that we believe could effectively separate the electron-hole pair and further enhance its

efficiency toward photocatalysis.

4.1 Co-oxide nanoclusters supported on Gr/Ir(111)

The experimental results described in this part of the chapter were carried out using spectroscopic techniques at the SuperESCA beamline (for chemical state analysis) and microscopic technique at the Nanospectroscopy beamline (for growth mechanism and cluster morphology analysis). The Ir(111) single crystal was cleaned by using the same methods described in earlier chapters. These procedures allowed obtaining a clean, well ordered substrate, as reflected in the sharp (1×1) LEED pattern, as shown in Fig 4.1 (left). Gr was epitaxially grown on the clean Ir(111) using the

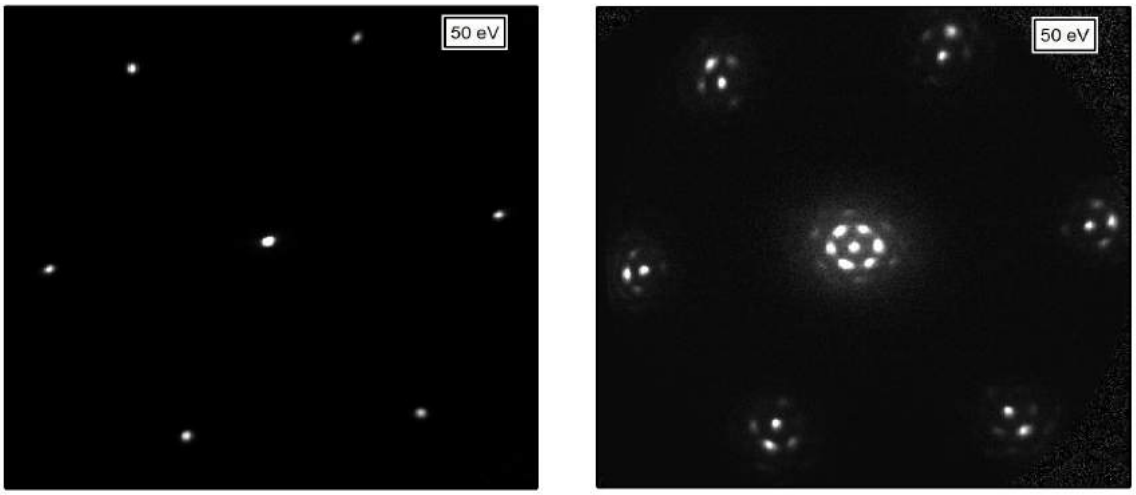

Figure 4.1: μ-LEED pattern acquired at E = 50 eV (left) Clean Ir(111) (right) Gr on Ir(111).

CVD method already descried in Chapter 3. The C 1s core level spectrum of the Gr/Ir(111) substrate (Fig. 4.2 (a)) shows a single component, as typical of weakly interacting lattice mismatched Gr-metal systems, which is in good agreement with data previously reported [31, 32] and also discussed in Chapter 3 [33]. The LEEM image acquired after Gr growth, Fig. 4.3 (a) shows that the Gr grows over the steps and uniformly extends on the terraces of the Ir(111) surface. The LEED images show the features of a moiré superlattice (Fig. 4.1 (right)), *i.e.* formed by (10×10) unit cells of Gr over (9×9) substrate unit cells in good agreement with previous studies [31, 34, 35]. Based on previous studies [31, 34, 35], we estimate that the C coverage of an ideal single layer of Gr extending over the whole substrate is $2(10 \times 10)/(9 \times 9)$

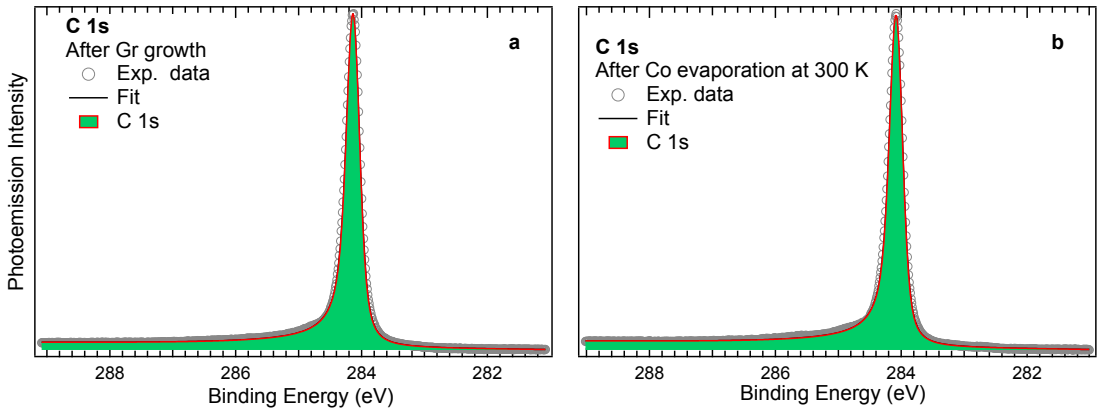

Figure 4.2: High energy resolution C 1s core level spectrum of Gr/Ir(111) measured at $h\nu$= 400 eV in the normal emission configuration, (a) before and (b) after Co deposition at 300 K. The spectrum shows a single component, a hallmark of weakly interacting lattice-mismatched Gr/metal systems.

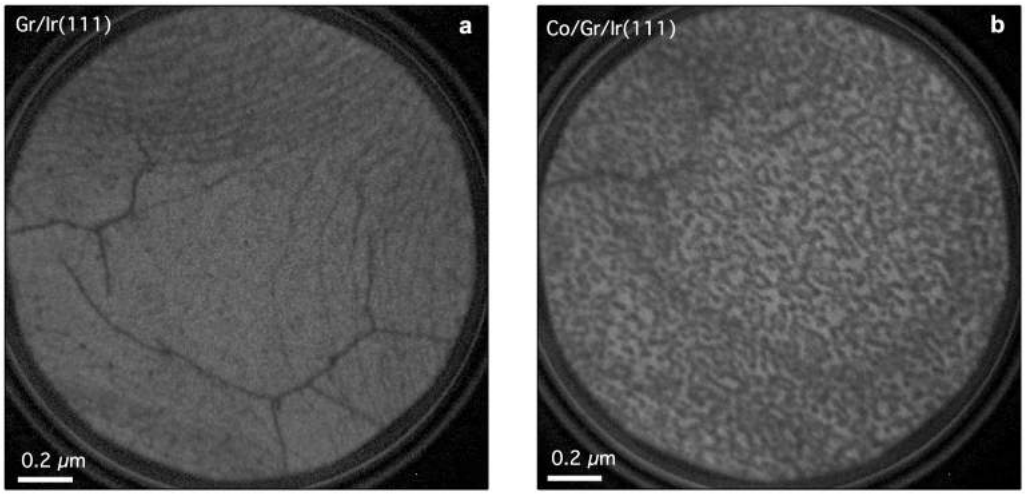

Figure 4.3: LEEM images (a) Gr on Ir(111) with SV = 3.6 eV and (b) as deosited Co-clusters with SV = 5.5 eV (SV= start voltage).

$\cong$ 2.5 ML (Gr has two C atoms per unit cell). Here and in the following, we adopt the conventional definition of one ML as the surface coverage corresponding to one adsorbate for each atom of the substrate surface. In order to further confirm that the Gr grown by our method is formed by just a monolayer of C atoms (see Fig. 4.4) we measured the electron reflectivity curve from clusters free Gr regions (see Fig. 4.4 (b)). We found that this curve is in very good agreement with what was previously found by the McCarty group [36] for a single layer Gr, as shown in red curve in Fig. 4.4 (c).

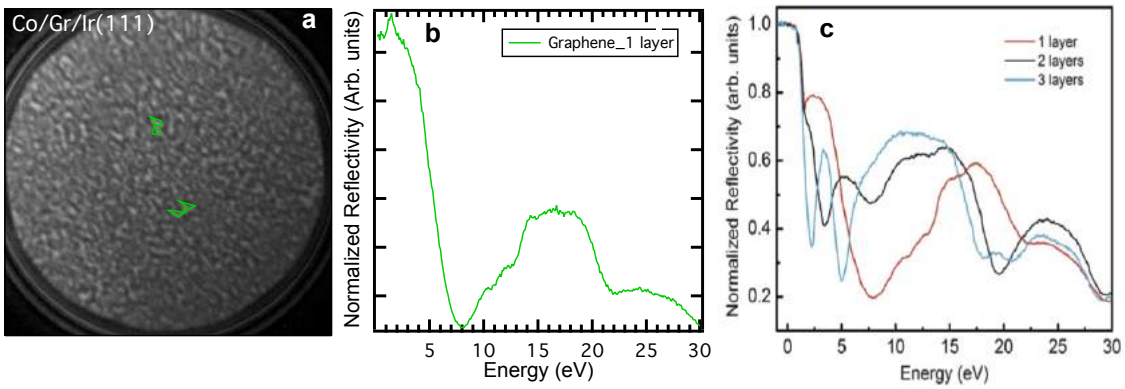

Figure 4.4: Characterization of Gr-film thickness (field of view (FOV) = 1.3 μ m) (a) LEEM Image, Green box show analyzed region (b) variation in electron reflectivity vs. energy measured from regions marked in image (a), (c) Adopted from [36] for comparison.

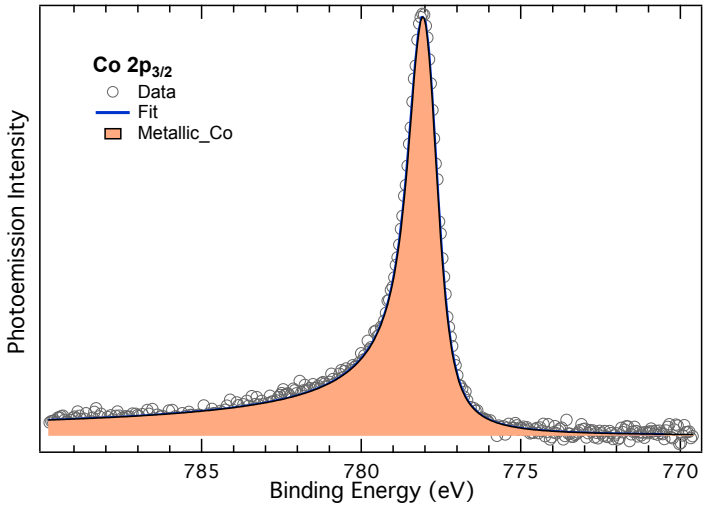

Figure 4.5: Co $2p_{3/2}$ core level spectra acquired at *hv*= 880 eV after Co deposition at 300 K.

After the preparation and characterization of the Gr/Ir(111) interface, we have grown Co-nanoclusters by sublimation of pure Co metal, keeping the surface at 300 K in order to limit the diffusion of atoms and clusters. Further, at this temperature the intercalation is precluded, and the metallic species usually tend to form clusters on top of graphene/Ir(111). It is also quite clear from the LEEM image, shown in Fig. 4.3 (b), that these nanoclusters are randomly distributed all over the Gr/Ir(111) rather than following any preferable growth nucleation site, in good agreement with previous investigations [37, 38]. The start voltage values used to acquire the images in 4.3 (a,b) are low in order to get images in LEEM regime for better morphological

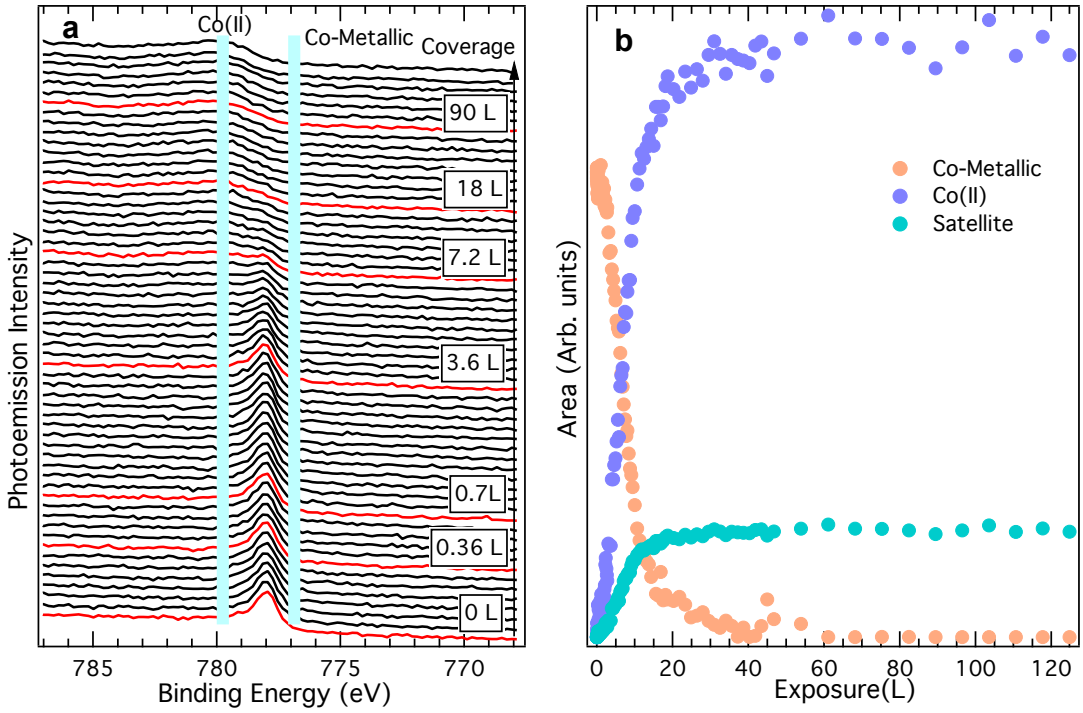

Figure 4.6: Time–lapsed series of Co $2p_{3/2}$ core level spectra ($h\nu$= 880 eV) acquired at different exposures during Co-nanocluster oxidation at 300 K, (a) Co $2p_{3/2}$ and (b) quantitative analysis obtained from (a).

contrast (for cluster size and distribution determination). In order to determine the chemical state of Co-nanoclusters we acquired HR-XPS Co $2p_{3/2}$ core level spectra and found that they show only a single component at 778 eV (see Fig. 4.5). Based on the comparison with previous literature data [39, 40] we attribute this component to metallic cobalt. It is also quite clear from Fig. 4.2 (b) that the C 1s core level spectrum does not show appreciable modifications upon cluster deposition.

The oxidation of the Co clusters was performed at 300 K by introducing oxygen at a pressure ranging from 2×10^{-9} to 5×10^{-7} mbar, while monitoring O 1s and Co $2p_{3/2}$ in real-time until no further spectral changes were observed, *i.e.* up to complete oxidation of cobalt-clusters. The evolution of the system during oxidation is shown in time lapsed series of Co $2p_{3/2}$ core levels shown in Fig. 4.6 (a). The initial stage of the uptake (at exposures <10 L) is characterized by the appearance of a new component at 779.4 eV which in earlier studies [39, 40] has been identified as the fingerprint of Co-oxide formation. The intensity of this peak stops growing once it reaches saturation after 20 L of oxygen exposure, as shown in Fig. 4.6 (b). On

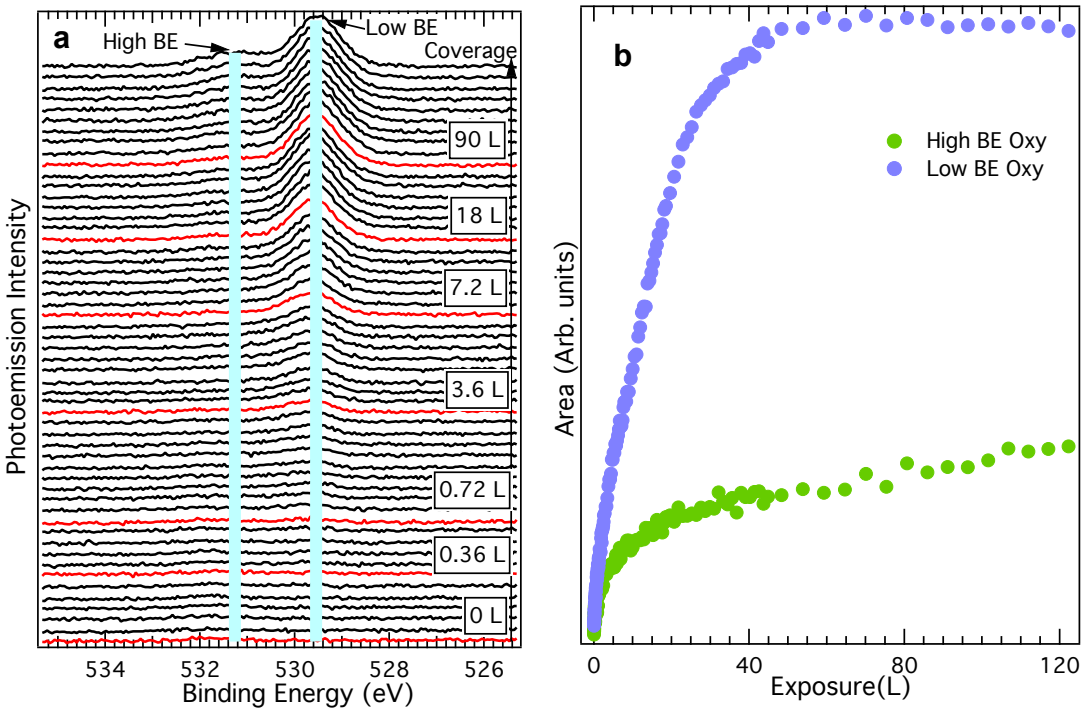

Figure 4.7: Time–lapsed series of O 1s core level spectra ($h\nu$= 650 eV) acquired at different exposures during Co-nanocluster oxidation at 300 K, (a) O 1s and (b) quantitative analysis obtained from (a).

other hand the evolution of different O 1s core level components during oxidation is reported in Fig. 4.7 (a). The initial stage of the uptake is characterized by the appearance of a single peak at about 529.45 eV (labelled as Low BE in Fig. 4.7 (a)). At higher oxygen exposure the low BE peak is saturated and another component at high BE, as shown in Fig. 4.7 (a), start appearing at 531.2 eV.

4.1.1 Characterization of Co-oxide nanoclusters

In order to better understand the chemical state of Co clusters after oxidation, we analysed the Co $2p_{3/2}$ and O 1s spectra. The analysis of Co $2p_{3/2}$ is quite complex due to the background and the appearance of satellite peaks. However, following what was done previously for Co $2p_{3/2}$ [39, 40, 41], we have adopted a Shirley background. The core level spectra have been decomposed into several components, whose individual shape consists of a Donjach-Sunjic line profile convoluted with a Gaussian distribution. From the data analysis we conclude that the pristine Co $2p_{3/2}$

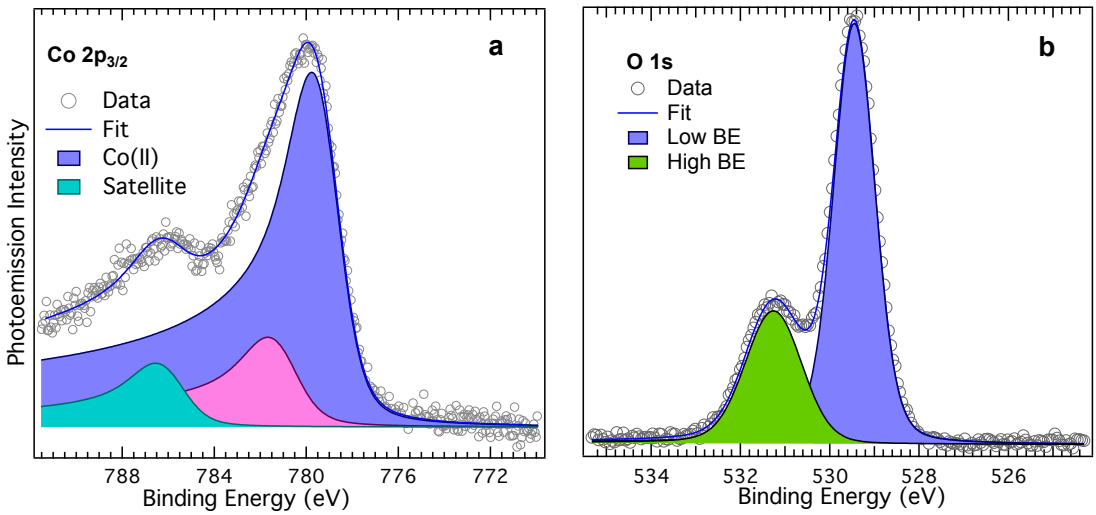

Figure 4.8: HR-XPS core level spectra acquired after Co-nanocluster oxidation at 300 K (a) Co $2p_{3/2}$ at $h\nu$= 880 eV (b) O 1s at $h\nu$= 650 eV.

consists of a single core level component with BE of 778 eV, which is characteristic of the metallic Co^0 species, as shown in Fig. 4.5. After the oxygen exposure, the metallic component slowly decreases and the emission peak evolve at higher binding energies in the range 779.26 eV, as shown in Fig. 4.8 (a). This peak, which is quite broad, due to the multiplet coupling effects [42, 43], needs more than one component to be properly described. We added another component at 781.13 eV as described in previous studies [39] in order to get best fit. On the other hand a peak at 786.02 eV can be recognized as the shake-up satellite peak which is characteristic of late transition metals in their respective oxides [44]. It could be attributed to Co cations that are tetrahedrally coordinated in Co^{+2} chemical state and give rise to shake-up peaks, since in this configuration the crystal field leads to a low energy e_g doublet and a partially filled higher energy t_{2g} triplet. In a simplified relaxation model, the absence of satellite features can be understood as a consequence of an electronic structure consisting of filled valence levels to which charge transfer from the ligand is precluded [44, 45, 46]. This is expected to be the case for octahedrally coordinated trivalent cobalt, where the crystal field splits the 3d levels into a low energy triplet t_{2g} level, and to a high energy e_g doublet, leading to full occupancy of the t_{2g} states, with a corresponding low spin state. In our case, we found a satellite peak at 786.02 eV, which corresponds to a $2p^5 3d^7$ final state [42, 47]. It is important to underline that

satellite features may be employed to identify the valence state of cobalt in oxides, thus suggesting the presence of cobalt-oxide species, more specifically Co^{+2} oxide that consists of a main oxide peak at 779.26 eV and a satellite peak at 786.02 eV, both features are consistent with a CoO stoichiometry [42, 47].

The O 1s HR-XPS spectra shows two distinct components, as shown in Fig. 4.8 (b), the first at 529.45 eV associated to the presence of Co^{+2}, as previously assigned [39, 40, 41]. The second peak at 531.2 eV could be associated to

- the hydroxyl species (OH),
- cation coordination change from tetrahedral monoxide (CoO) to octahedral, *i.e.* in more oxidized spinal oxide (Co_3O_4) [41].

However, in this case the first hypothesis seems to more valid because hydroxyl species are stable on oxide surfaces. On the other side, we ruled out the presence of any CO or carbonate species and its also quite clear from C 1s spectra shown in Fig. 4.10 (c).

In order to further understand the effect of clusters on Gr, we acquired LEED images, as shown in Fig. 4.9. The line profile analysis of the diffraction patterns proved that the moiré cell of Gr/Ir(111), up to Co-oxide formation, exhibits the same periodicity. The fact that, in all three cases (Gr/Ir(111), Co/Gr/Ir(111) and CoO/Gr/Ir(111)), the LEED spots of the overlayer are aligned with the radial direction between the zero- and the first–order diffraction spots, without appreciable broadening, indicates that the moiré lattice is still preserved after Co-deposition and its oxidation. These findings suggest that the Gr structure has not changed appreciably. The corresponding C 1s spectra of Gr after Co oxidation shows a single component at 284.12 eV which indicates that Gr is still present as reported in Fig. 4.10 (c). This oxidation was done at 300 K where oxygen has very small probability of intercalation as reported in previous studies [48, 49], where intercalation starts above 600 K. The background in LEED images is only slightly changed, but the first order spots that get weaker after oxidation, is a sign of some disorder introduce by the intercalation process.

From the application point a view in catalysis, it is important to investigate the size distribution of the Co-nanoclusters grown on the Gr/Ir(111) interface. The

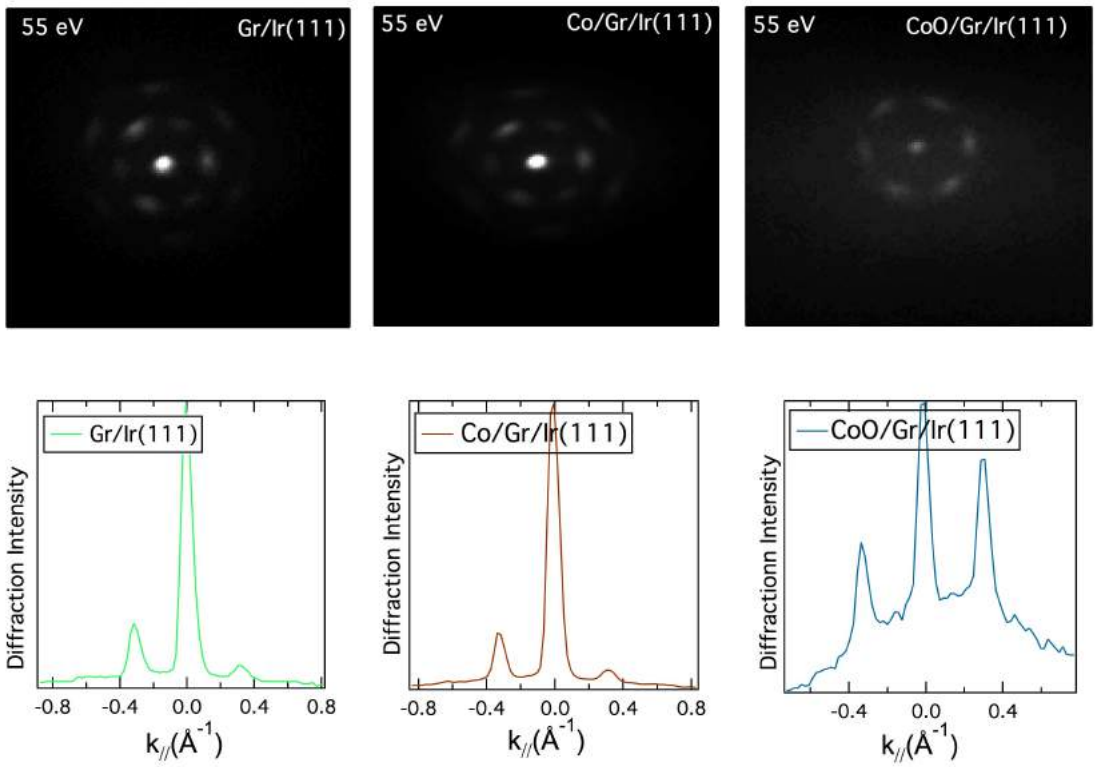

Figure 4.9: Top (from left to right): LEED patterns of clean Gr/Ir(111), Co-nanoclusters/Gr/Ir(111) and CoO/Gr/Ir(111), respectively. All the images were acquired at 55 eV electron energy. Bottom: comparison of the LEED line profiles of the 3 systems, measured along the direction between two diametrically opposite first–order spots of the Gr moiré.

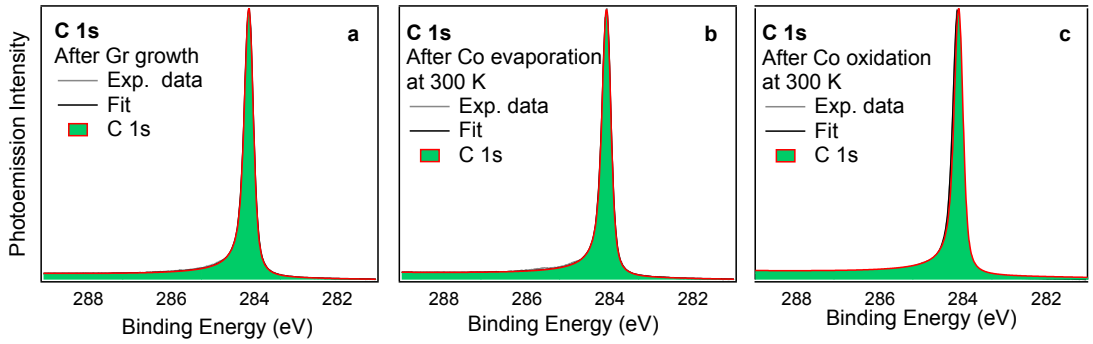

Figure 4.10: High energy resolution C 1s core level spectrum of Gr/Ir(111) measured at $h\nu$= 400 eV in the normal emission configuration, (a) after Gr growth (b) after Co deposition at 300 K and (c) after Co oxidation at 300 K. The spectrum shows a single component a hallmark of weakly interacting lattice-mismatched Gr/metal systems.

LEEM image in Fig. 4.11 (a) shows that the areas contoured with white spots are the Co-clusters on Gr. Image line profile allow us to estimate the particle size as shown in Fig. 4.11 (b) which is about 20 nm and is compatible with the value obtained from the detailed particle analysis and reported in Fig. 4.11 (c).

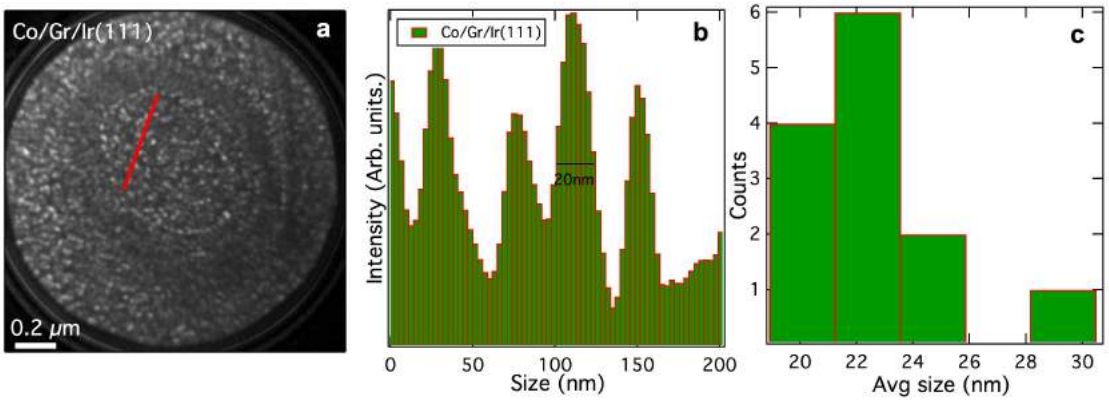

Figure 4.11: Size distribution of Co-nanoclusters on Gr/Ir(111) interface (a) LEEM image of Co-nanoclusters/Gr/Ir(111) (b) particle size from line profile from the LEEM image as shown in red (c) histogram of the cluster size distribution.

The final goal of this research activity was to test the catalytic properties of the Co^{+2} oxide prepared on top of Gr/Ir(111). This was done in collaboration with the group led by Prof. Fornasiero at the Chemistry Department, University of Trieste. We performed the photo-catalytic measurements on the sample prepared at Elettra under the simulated sunlight irradiation in their experimental set up. Illumination was performed using solar simulator (LOT-Orial) equipped with 150 W Xe lamp (for only visible irradiation a 400 nm cut-off filtered was used). The sample was mounted on a sample holder and placed on the bottom of the reactor, filled with water in the first case and with methanol/water 1:1 (v/v) in the second case. All the experiments were performed with the photo-reactor immersed in a thermostatic bath at 25 °C. Evolved gaseous products were striped by Ar flow (flux of 15 ml/min) and on-line detected by an Agilent Gas Chromatograph. We performed a series of experiments on both bare Gr/Ir(111) (as a blank) and Co^{+2} oxide clusters on Gr/Ir(111), but unfortunately didn't get the desired results. The reasons can be found in the detection limit of the instrument, in the chemical state of our Co-oxide nanoclusters (CoO) (with pressure and temperature range we used), which is known

to be less active toward photocatalysis than Co_3O_4 and could also be related to the particle size and surface oxygen species which highly effects the catalytic activity.

In conclusion, using the Gr/Ir(111) interface as a model system, we were able to grow Co-oxide nanocluster at 300 K. From an application-oriented standpoint, the stability of these system is the key factor as we didn't observe any change with temperatures up to 500-600 K (data not shown here). The thorough understanding of theses architecture, both by spectroscopic and microscopic methods, will add further insight into the design of such system which could find possible application in the field of catalysis.

4.2 Ti-oxide nanoclusters supported on Gr/Ir(111)

Titanium dioxide, is known as very interesting material in the field of catalysis owing to its chemical stability, high chemical inertness, non-toxicity and low cost [50]. However, due the large band gap (3.2 eV) its use is limited only to the narrow range of UV (3-5% of total sunlight) [51]. In addition electron-hole recombination probability further restricts its photocatalytic application. In fact, the photo-generated electrons and holes in TiO_2 may experience a rapid recombination, which significantly decreases the efficiency of the photocatalytic reaction [52]. For this reason the inhibition of the recombination of photo-induced electron–holes and the extension of the light absorption to the visible light region are the key factors for improving the photocatalytic activity of TiO_2 [52, 53]. Recently, incorporation of carbon based materials with TiO_2 has been demonstrated to improve the efficiency towards photocatalysis activity. These carbon based materials, like single walled carbon nanotubes, fullerenes, and graphene were used as an electron acceptor to enhance the photo-induced charge transfer [54, 55]. Many efforts have been made to incorporate Gr into TiO_2 based materials like in the case of GS (graphene sheets)/TiO_2 composite photo-catalysts [56]. Self-assembled TiO_2 nanorods [57] on Gr-oxide sheets at water/toluene interface are another example effective charge anti-recombination structure. However, TiO_2-nanoclusters has been ignored until now. We believe that well dispersed TiO_2 nanoclusters on Gr can be crucial to enhance the photocatalytic water splitting. The bandgap of TiO_2 decreases from 3.28 to 3.17 eV when particle size decreased from 29

to 17 nm and then increases from 3.17 to 3.28 eV as particle size decreased from 17 to 3.8 nm [58] . This behaviour then depends upon the effective masses and dielectric constant of TiO_2. This nanomaterial will play its role by decreasing average size of TiO_2 nanoclusters in a range to effectively reduce the bandgap.

4.2.1 Ti-oxide/graphene interfaces

Deposition and growth of metal- and oxide-nanoclusters are performed with an intention to explore the role of graphene-nanoclusters in the overall photocatalytic reactivity. Our goal was to create Gr-TiO_2 composites material, where Gr will act

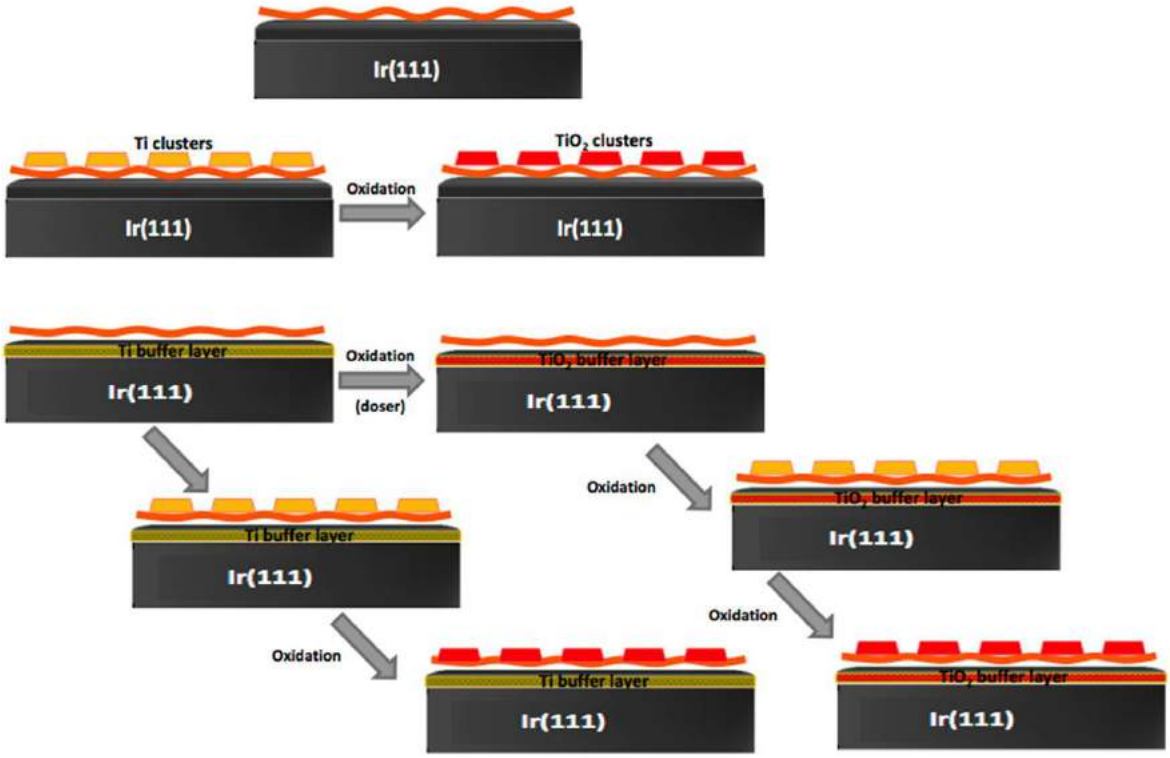

Figure 4.12: Schematic outline of the the different architectures and interfaces which have been synthesisized and characterized.

as a buffer layer to inhibit electron-hole recombination, to provide support and to anchor Ti-oxide nanoclusters. We have adopted the strategy of growing titania above the corrugated graphene layer prepared on Ir(111), at the interface and in both configurations, as illustrated in Fig. 4.12. We prepared three different architectures

- TiO_2/Gr/Ir(111): after the growth of Ti-nanoclusters on Gr/Ir(111) at 300 K we proceeded with the oxidation at 300 K in $p(O_2) = 2\times10^{-9} \div 5\times10^{-6}$ mbar.

- TiO_2/Gr/Ti/Ir(111): after the intercalation of titanium at 700 K we subsequently deposited Ti-nanoclusters at 300 K. A final oxidation was performed at 300 K in $p(O_2) = 2\times10^{-9} \div 5\times10^{-6}$ mbar.

- TiO_2/Gr/TiO_2/Ir(111): after the intercalation of titanium at 700 K we subsequently oxidized the intercalated layer at 600 K in $p(O_2) = 5\times10^{-4}$ mbar. Then we have grown Ti-nanoclusters at 300 K and a further oxidation was performed at 300 K in $p(O_2)= 2\times10^{-9} \div 5\times10^{-6}$ mbar.

In order to understand the intercalation and the oxide formation processes we did a series of experiments by following in situ the evolution of surface species using core level photoemission spectroscopy with synchrotron radiation. The results are discussed in the following sections.

4.2.2 Charaterization of Ti-oxide/graphene interfaces

The measurements described in this section were carried out using spectroscopic technique at the SuperESCA beamline of Elettra. The Ir(111) cleaning procedure and the Gr growth were done in a similar manner as previously described. On top of Gr/Ir(111) we have grown Ti clusters. The nanocluster were obtained by Ti sublimation from high purity Ti wire wrapped in W wire in order to avoid collapse during evaporation. A Quartz Micro Balance (QMB) was used in parallel during deposition to get the exact amount of Ti being evaporated during each deposition step.

In the first part of the characterization, we focused on how the different architectures influence the C 1s and Ir 4f core level spectra. The comparison of the Ir $4f_{7/2}$ core level spectra of the substrate prior and after the Gr growth (Fig. 4.13 (a)) shows that the substrate is not appreciably modified by the presence of the C layer. For Gr/Ir(111) and TiO_2/Gr/Ir(111), we notice only a reduction of the Ir 4f photoemission intensity due to the screening effect of the Gr film and Ti-oxide. The surface component of Ir $4f_{7/2}$ spectra signals disappear completely only when we intercalate Ti between Gr/Ir(111), and also for the TiO_2/Gr/Ti/Ir(111) and TiO_2/Gr/TiO_2/Ir(111) interfaces. In fact, Ir $4f_{7/2}$ core levels show distinct spectral features for bulk and surface atoms, due to the different coordination. As the interca-

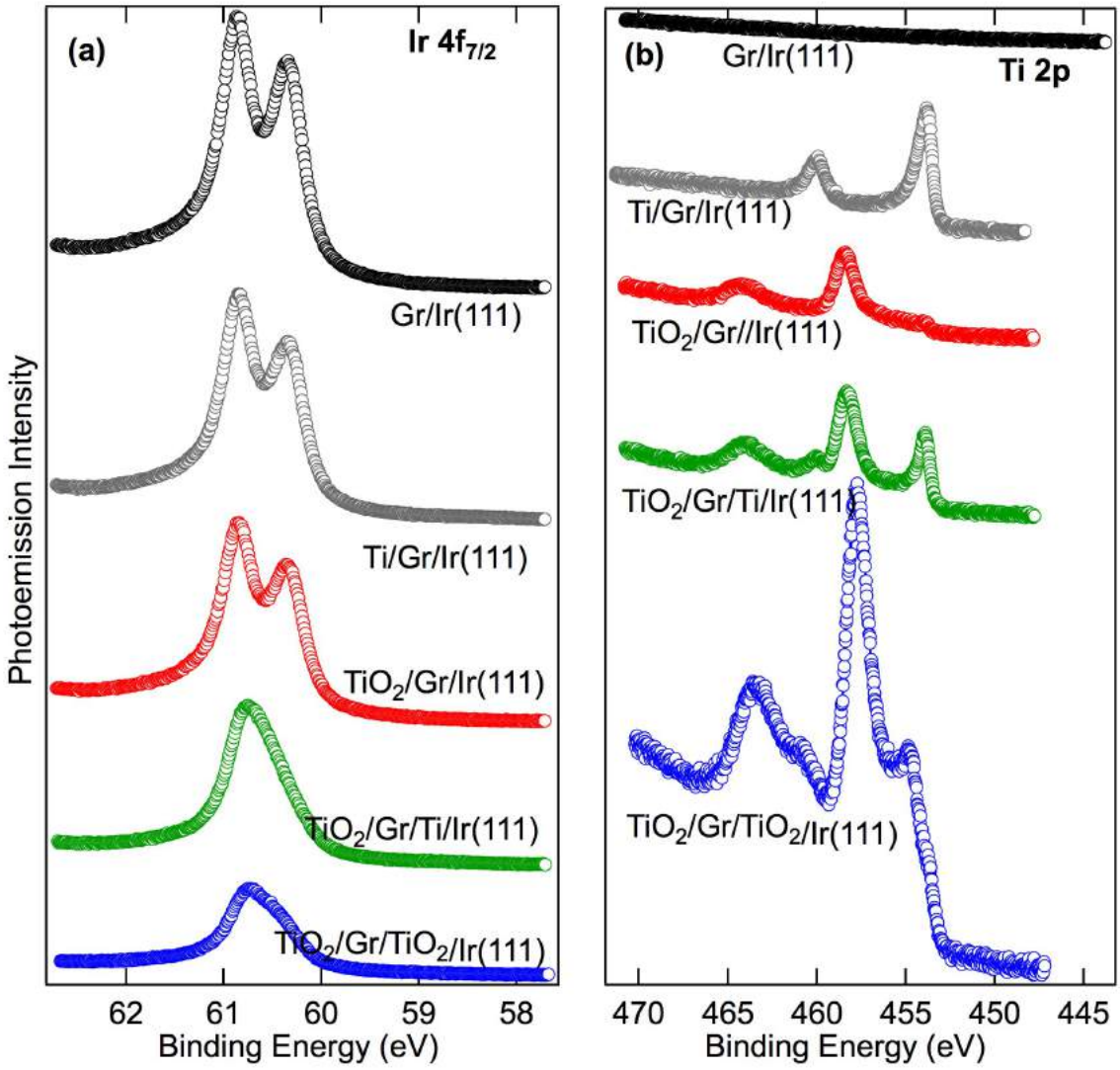

Figure 4.13: Comparison of core level spectra of (a) Ir $4f_{7/2}$ ($h\nu$= 200 eV), (b) Ti 2p ($h\nu$= 550 eV) in different configuration for the Ti-oxide/Gr interfaces.

lation proceeds, the intercalated metal cover the substrate surface atoms, thus their local coordination and chemical environment is largely affected. As we are reaching 1 ML of intercalated species, the population of substrate surface atoms decreases and eventually vanishes. In the C 1s spectra we observe a single component at 284.1 eV, typical of weakly interacting lattice mismatched Gr-metal systems [32]. A summary of the C 1s spectra acquired for different investigated systems is reported in Fig. 4.14. The C 1s spectra for the first architecture TiO_2/Gr/Ir(111) shows a very small shift of 100 meV towards high BE, which can be appreciated in Fig. 4.14 (red curve). However, the TiO_2/Gr/Ti/Ir(111) interface induces an upward shift of 360 meV (see Fig. 4.14, green curve). This shift to high BEs is more prominent with Ti intercalation

and could be related to n-doping as also discussed in the case of Si-intercalation [59, 49, 60] is related to interfacial Ir atoms interacting with Ti-layer. On the other hand, in the presence of a oxide layer below Gr for the TiO_2/Gr/TiO_2/Ir(111) interface, we observe a shift of -200 meV to low BE after high pressure oxidation of intercalated Ti-layer (see Fig. 4.13, blue curve). This C 1s shift to lower BE could be

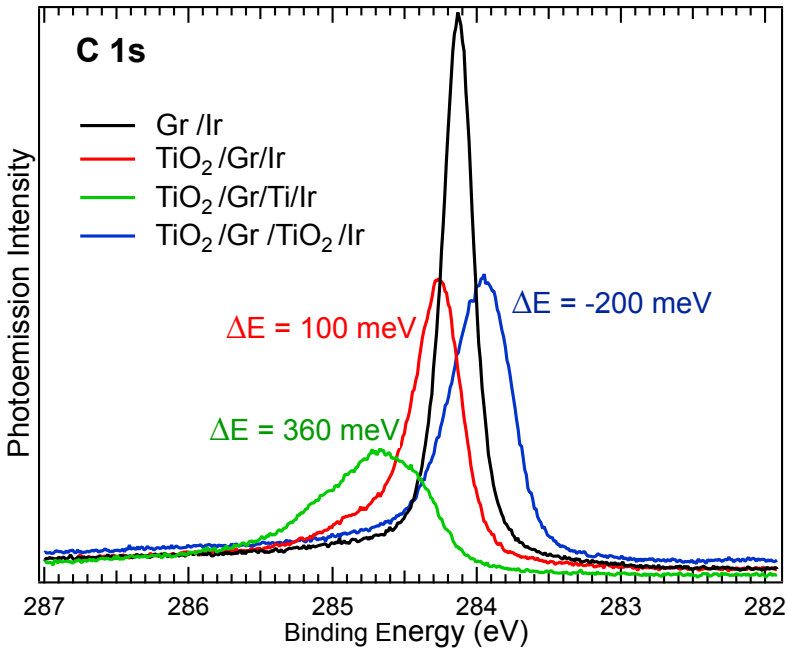

Figure 4.14: Comparison of C 1s core level spectra ($h\nu$= 400 eV) corresponding to different configuration for the Ti-oxide/Gr architectures.

attributed to the Gr sitting on the oxide layer and charge transfer from Gr to the more electronegative oxygen atoms, leading to the hole doped Gr [49] when the oxidation is performed at 600 K.

Finally, the as grown Ti-clusters show only a metallic peak in the Ti $2p_{3/2}$ core level (see Fig. 4.13 (b)) while in case of Ti-oxide nanoclusters we found quite complex line shape, which may be due to the presence of more than one kind of oxide. In order to understand the complexity of oxide species formed upon growth and oxidation we did a detailed analysis of Ti 2p and O 1s XPS spectra.

4.2.3 Core-level photoemission spectroscopy of Ti-oxide

The data analysis of Ti 2p peak was complex due to spin-orbit splitting and multiple oxidation states. For these reasons, core level spectra have been decomposed into

several components, whose individual shape consist of Donjach-Sunjic line shape profile convoluted with Gaussian distribution. The intensity ratio of the spin-orbit splitted $2p_{3/2}$ and $2p_{1/2}$ were also constrained to 2:1. Once the relative positions were set, the spectra were fitted using a Shirley-background. The Ti 2p along with O 1s spectra for all different configuration are discussed below.

- **TiO_2/Gr/Ir(111)**

The Ti 2p spectra of Ti-nanoclusters grown on Gr/Ir(111) at 300 K are reported in Fig. 4.15, which clearly indicates that as grown Ti-nanoclusters are in metallic states with Ti $2p_{3/2}$ peak at 453.7 eV BE, *i.e.* with BE value which is a fingerprint of the metallic state of Ti [61, 62].

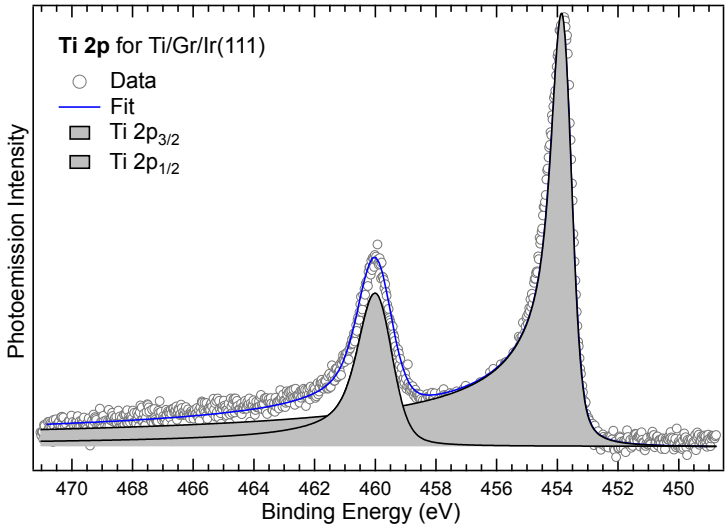

Figure 4.15: HR-XPS core level spectra of Ti 2p ($h\nu$= 550 eV) acquired after Ti deposition at 300 K.

The oxidation of Ti-clusters was performed at 300 K by slowly increasing the oxygen pressure from $1\times10^{-9} \div 5\times10^{-6}$ mbar over a period of half an hour in order to reach oxygen saturation. In order to accurately analyze the data for the Ti-oxide nanoclusters, we firstly obtain the line shape parameters (Γ,α,G) from the spectra acquired with different architecture of Ti-clusters, and assumed that the line shape of each component (Γ,α) was unchanged throughout all the experiment, whereas the Gaussian parameter G was allowed to change, in order to describe possible contributions due to structural inhomogeneities. The spin-orbit splitting was kept fixed to 6.01 eV for metallic and 5.8 eV for oxide components, in contrast to the

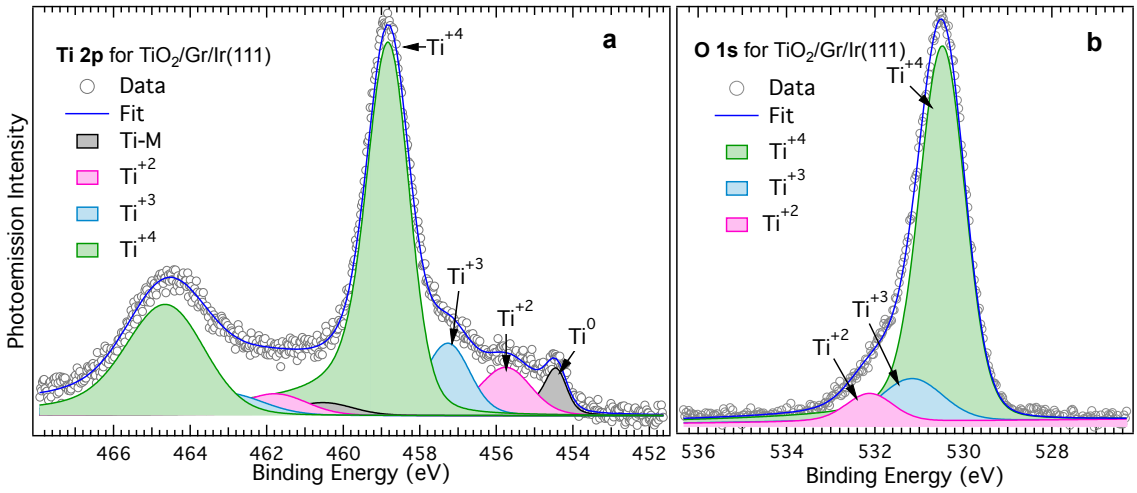

Figure 4.16: HR-XPS core level spectra acquired after Ti-nanocluster oxidation at 300 K, (a) Ti 2p ($h\nu$= 550 eV) and (b) O 1s ($h\nu$= 650 eV).

previous studies [61, 62, 63, 64], where different spin-orbit splitting value were used for each oxide specie in titanium. In the Ti 2p spectra (see Fig. 4.16 (a)), the peak with lowest BE is assigned to the $2p_{3/2}$ of the titanium atoms at the interface while the peak at 458.77 eV is assigned to Ti^{+4} species. Beside these, the Ti^{+x} oxide peak between Ti^{0} and Ti^{+4}, with distinct BE at 455.56 and 457.2 eV is attributed to the sub-oxide Ti^{+3} and Ti^{+2} and is in line with values found for these oxide systems [61, 62, 63, 64, 65, 66]. The O 1 spectra for this architecture shows three distinct peaks as reported in Fig. 4.16 (b), with BEs at 530.35, 530.8 and 531.9 eV. These components can be attributed to the oxide present in Ti^{+4}, Ti^{+3} and Ti^{+2} oxidation states respectively [62, 61, 65]. Nevertheless there is a possibility that the 531.9 eV component arises due to hydroxyl (OH) species which are ubiquitous on oxide surfaces. We neglected this hypothesis here as in the O 1s spectra (see Fig. 4.16 (b)), the shift to higher BE is associated with the electron transfer from oxygen to titanium atoms and this is well in line with previous study [65].

- **TiO_2/Gr/Ti/Ir(111)**

We have then extended our analysis to the TiO_2/Gr/Ti/Ir(111) architecture. For this design we intercalate Ti between Gr/Ir(111) interface by keeping the sample at 700 K. HR spectra obtained after this intercalation are shown in Fig. 4.17 (a). The BE for this intercalated metallic titanium is different than what we previously found for the metallic titanium reported in Fig. 4.15. It moved 670 meV towards high BE, keeping

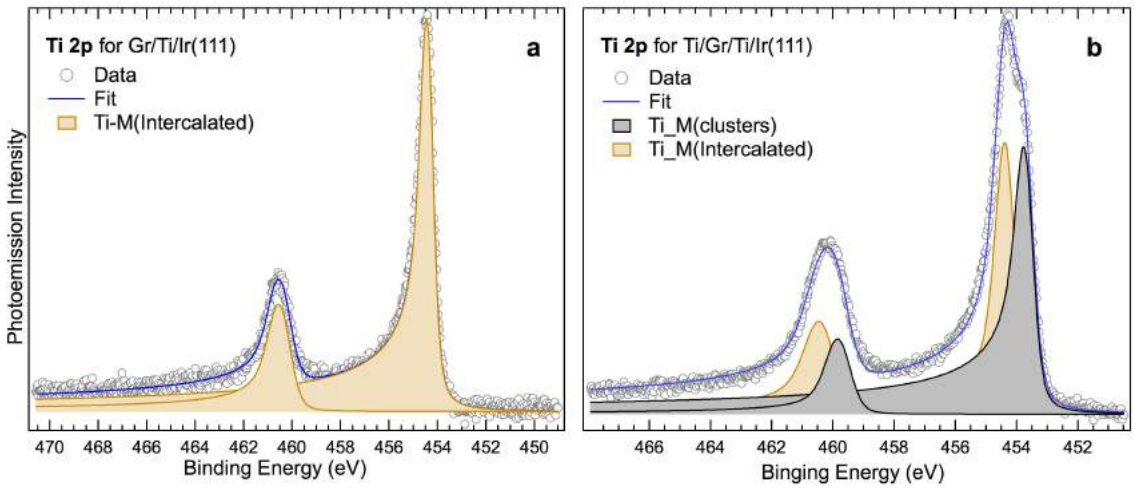

Figure 4.17: HR-XPS core level spectra of (a) Ti 2p after Ti-intercalation at 700 K and (b) Ti 2p after Ti deposition on top of Gr/Ti/Ir(111) at 300 K acquired with ($h\nu$= 550 eV).

the same spin-orbit splitting as for metallic titanium (6.01 eV). This indicates that this titanium layer is present in a metallic state at the interface between Gr and Ir(111), forming a chemical bond with the Ir surface underneath. After this Ti-intercalation,

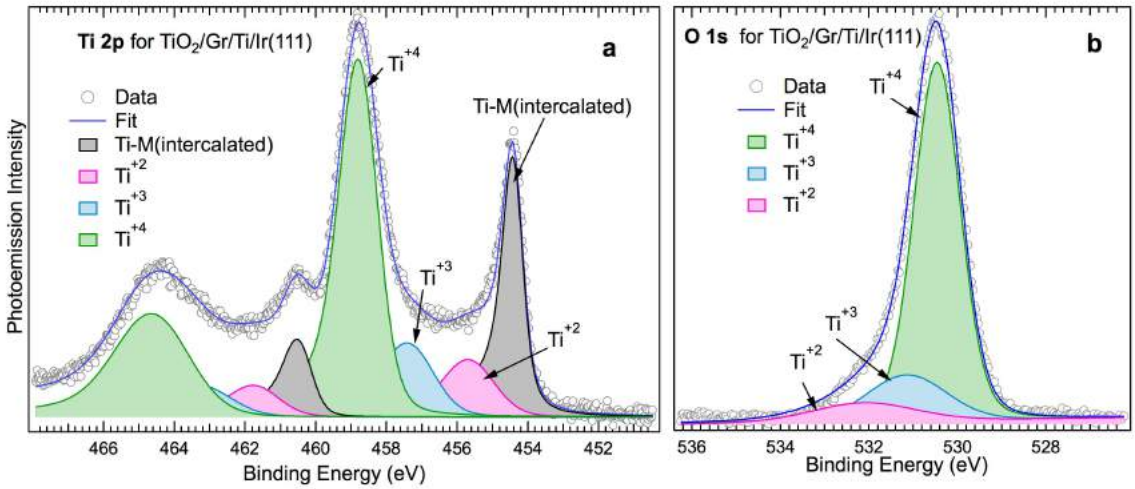

Figure 4.18: HR-XPS core level spectra acquired after oxidation at 300 K for the TiO_2/Gr/Ti/Ir(111) architecture, (a) Ti 2p ($h\nu$= 550 eV) and (b) O 1s ($h\nu$= 650 eV).

we grow Ti-clusters at 300 K and get Ti-clusters on top of Gr (Gr/Ti/Ir(111)), as shown in Fig. 4.17 (b). In this case the peak at low BE (gray colored) appearing at 453.7 eV is similar to the metallic titanium as described earlier for the first architecture (Ti^0/Gr/Ir(111)) (see Fig. 4.15) and the second peak at 454.3 eV is attributed to the metallic titanium at the interface. The next step after the Ti-cluster deposition was

the oxidation. This was in similar way as it was done for previous architectures by slowly increasing the pressure of oxygen in step from $1\times10^{-9} \div 5\times10^{-6}$ mbar at 300 K. The oxidation of Ti-cluster produces the same species of titanium-oxides (see in Fig. 4.18(a) and (b)) as we observed in case of TiO_2/Gr/Ir(111) reported in 4.16 (a) and (b).

- **TiO_2/Gr/TiO_2/Ir(111)**

As a final structure, we prepared an architecture in which Gr is sandwiched between TiO_2 structures. The sample preparation and Gr growth was performed in similar manner as previously done. The intercalation of titanium was achieved at 700 K with a subsequent oxidation achieved at 600 K with a pressure up to $p(O_2) = 5\times10^{-4}$ mbar for one hour which corresponds to a total exposure of 10^6 L. The oxidation of intercalated titanium is quite critical, with two main limitations. The first one has to do with the temperature, because if we go too high in temperature then oxygen

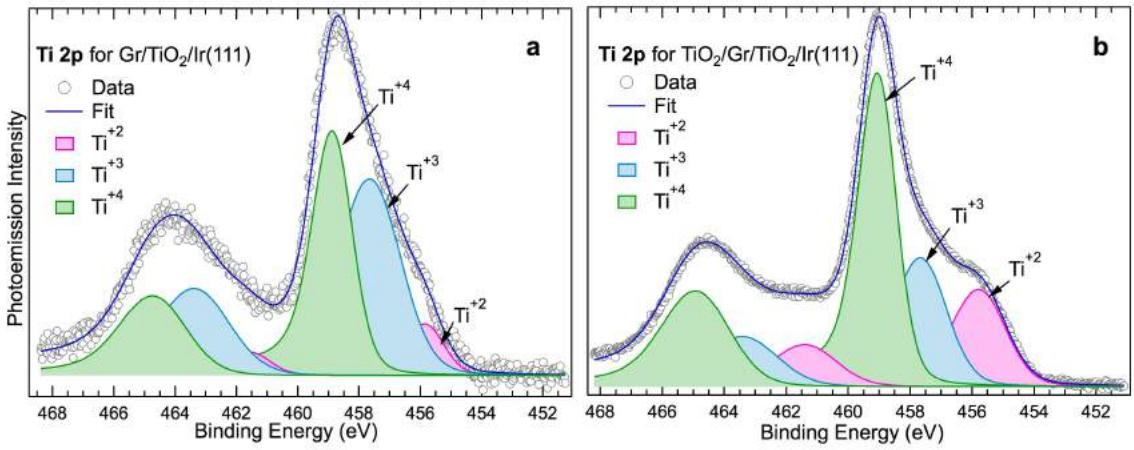

Figure 4.19: HR core level spectra of Ti 2p acquired at ($h\nu$= 550 eV) (a) after oxidation at 600 K for Gr/TiO_2/Ir(111) and (b) after oxidation at 300 K for TiO_2/Gr/TiO_2/Ir(111) architecture.

start reacting with Gr and etching it away [49]. The second limitation is related to the maximum pressure that can be used in UHV conditions. In order to overcome this we used a gas doser [67] to expose the sample to such a high oxygen pressure. After the oxidation of intercalated Ti-layer, we have grown Ti-clusters at 300 K on top of Gr/TiO_2/Ir(111), using the same procedure adopted above, and successively oxidized them at 300 K to get the TiO_2/Gr/TiO_2/Ir(111) architecture. From the analysis, it is quite clear that the Ti 2p spectra for intercalated oxide (Gr/TiO_2/Ir(111))

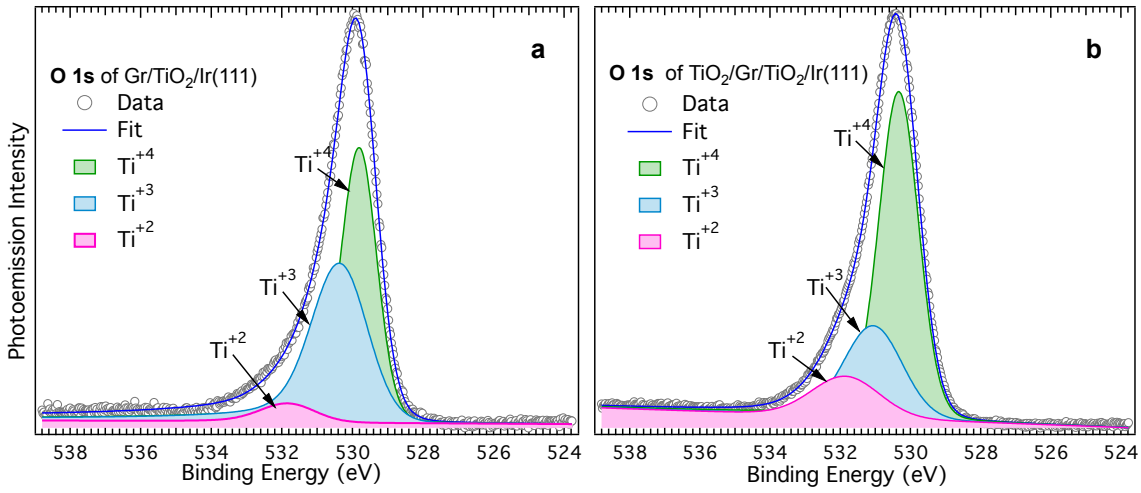

Figure 4.20: HR-XPS core level spectra acquired at ($h\nu$= 650 eV) for O 1s (a) after oxidation at 600 K for $Gr/TiO_2/Ir(111)$ and (b) after oxidation at 300 K for $TiO_2/Gr/TiO_2/Ir(111)$ interfaces.

in Fig. 4.19 (a) contain all three oxide species (Ti^{+2}, Ti^{+3}, and Ti^{+4}), but in slightly different ratio with respect to the Ti-oxide nanoclusters (see Fig. 4.19 (b)). This could be attributed to the incomplete oxidation of intercalated Ti-layer. The O 1s spectra of these Ti-oxides, shown in Fig 4.20 (a) and (b), present three distinct components corresponding to three kinds of oxide in these architectures.

It is important for an in depth chemical understanding to know what is present on the surface of the new architectures, as a fundamental step prior their final application in photocatalytic experiments. From our analysis we can conclude that the Ti-oxide nanoclusters either directly grown on top of Gr/Ir(111) or on $Gr/TiO_2/Ir(111)$) show same kind of oxide species *i.e.* (Ti^{+4}, Ti^{+3} and Ti^{+2}) and quantitative evaluation of these oxides gives 7.5:1.5:1 ratio corresponding to the population of each oxide. This is further confirmed by O 1s spectra: the main peak is associated with TiO_2 as a dominant component while the minor peaks at high binding energy are due to Ti_2O_3 and TiO in the order of TiO_2>Ti_2O_3>TiO.

4.2.4 Photocatalytic measurements

The photocatalytic measurements were performed using the set up described in chapter two. The Photo-catalytic experiments were performed using sensitizers in visible range with head spaced vials (total volume 20 mL). The vial containing

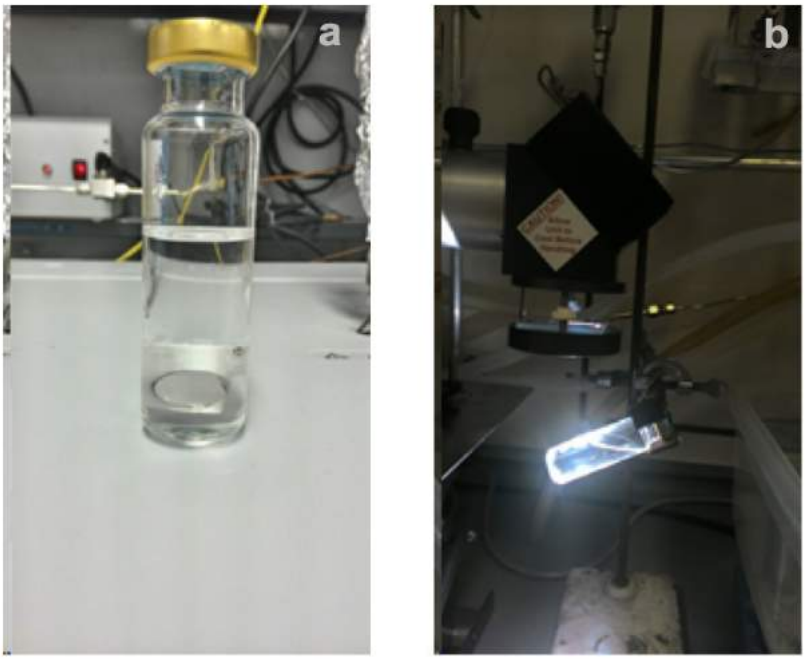

Figure 4.21: (a) Sample mounted in the vial and (b) sample under irradiation.

sample was filled with 12.5 mL solution with water and methanol 1:1 ratio. The vial was then sealed using appropriate rubber septa and air was removed bubbling Ar for 30 minutes. After this equilibrium period, the vial was irradiated using the system shown in Fig. 2.16. The analysis of the reaction products was performed injecting 50 μL of the gas phase into a gas chromatograph (Agilent 7890). The Thermal Conductivity Detector (TCD) was used for the quantification of H_2, using a MoISIEVE 5A column with Ar as carrier. This is a chemical specific detector and senses the changes in thermal conductivity of column effluent and compares it to a reference flow of carrier gas. The thermal conductivity of most of the compounds is less than the common carrier gases like helium or argon. When an analyte elutes, the thermal conductivity of the column effluents is reduced and produces detectable signal.

We prepared the TiO_2/Gr/TiO_2/Ir(111) sample and the system without Gr TiO_2/Ir(111), in order to see whether Gr is really playing its role as buffer layer and its effect on the photocatalyic activity. The results we obtained from the photocatalysis experiments showed that these Gr-titania based architecture is highly active towards H_2 production (see Fig. 4.21). We clearly measured a huge decrease of the photocatlytic activity without Gr at the interfaces. Titania-Gr interface is more than

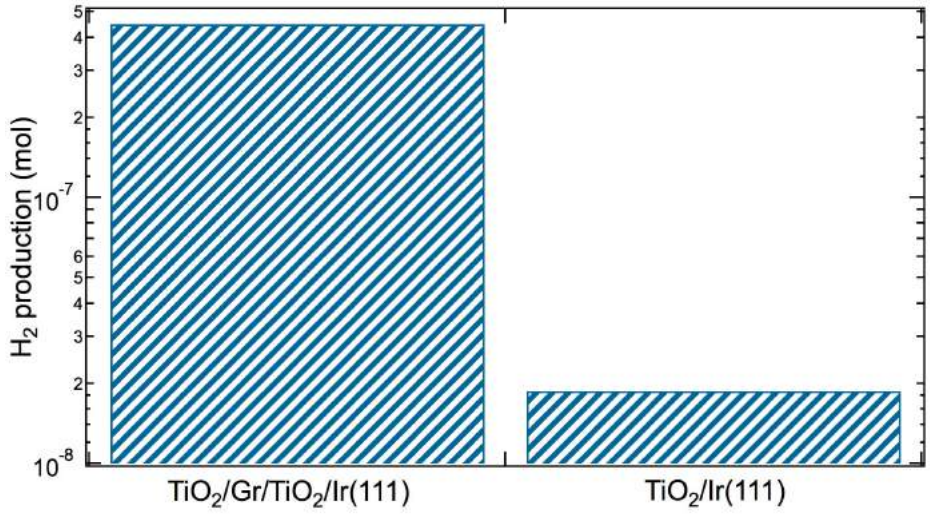

Figure 4.22: The production of H_2 after 20 h under illumination for titania-architecture with and without Gr.

20 times active (4.49×10^{-7} moles of H_2, corresponding to 0.8350 mol of H_2/mol of TiO_2) than titania without Gr (1.87×10^{-8} moles of H_2 , corresponds to the 0.0349 mol of H_2/mol of TiO_2) for photocatalytic hydrogen generation. We can conclude that Gr is playing its role as buffer layer and its presence effects the activity toward clean H_2 production with improved electron-hole separation after light excitation. Our next goal is two fold: firstly, to prepare same architectures and find the activity over the period of time and also compare it with other architecture like TiO_2/Gr/Ir(111) for comparison as in two cases the doping of Gr is different and secondly, extend the characterization to the cluster size, morphology and growth mechanism.

This study allowed us to understand the reaction of titanium atoms with oxygen above and at the interface of graphene. The architectures we have prepared and characterized have been used to test their photocatalytic performances. Very encouraging results have been obtained in the case of TiO_2/Gr/TiO_2/Ir(111) and presence of Gr at the interface plays a fundamental role.

Bibliography

[1] C. T. Campbell, S. C. Parker, and D. E. Starr. *The effect of size dependent nanoparticle energetic on catalyst sintering.* Science, 298: 811-814, 2002.

[2] B. Yoon, H. Hakkinen, U. Landman, A. S. Worz, J. M. Antonietti, S. Abbet, K. Judai, and U. Heiz. *Charging Effects on Bonding and Catalyzed Oxidation of CO on Au8 Clusters on MgO.* Science, 307: 403-407, 2005.

[3] M. Che, and C. O. Bennett. *The Influence of Particle Size on the Catalytic Properties of Supported Metals.* Advances in Catalysis, 36: 55-172, 1989.

[4] M. Harut. *Size and Support-Dependency in the Catalysis of Gold.* Catalysis Today, 36:153-166, 1997.

[5] H. A. Gasteiger, and N. M. Markovic. *Just a dream or future reality?* Science, 324:48–49, 2009.

[6] G. M. Whitesides, and G. W. Crabtree. *Don't forget long-term fundamental research in energy.* Science, 315:796–798, 2007.

[7] H. B. Gray. *Powering the planet with solar fuel.* Nature Chemistry, 1:7, 2009.

[8] M. W. Kanan, and D. G. Nocera. *In situ formation of an oxygen-evolving catalyst in neutral water containing phosphate and Co2p.* Science, 321:1072–1075, 2008.

[9] M. Armand, and J. M. Tarascon. *Building better batteries.* Nature, 451:652–657, 2008.

[10] Y. C. Lu. *Platinum–gold nanoparticles: a highly active bifunctional electrocatalyst for rechargeable lithium–air batteries.* Journal of American Chemical Society, 132:12170–12171, 2010.

[11] R. Bashyam, and P. A. Zelenay. *Class of non-precious metal composite catalysts for fuel cells.* Nature, 443:63–66, 2006.

[12] M. Lefevre, E. Proietti, F. Jaouen, and J-P. Dodelet. *Iron-based catalysts with improved oxygen reduction activity in polymer electrolyte fuel cells.* Science, 324:71–74 2009.

[13] L. Liao, Q. Zhang, Z. Su, Z. Zhao, Y. Wang, Y. Li, X. Lu, D. Wei, G. Feng, Q. Yu, X. Cai, J. Zhao, Z. Ren, H. Fang, F. R.-Hernandez, S. Baldelli, and J. Bao. *Efficient solar water-splitting using a nanocrystalline CoO photocatalyst.* Nature Nanotechnology, 9:69-73, 2014.

[14] J. Jasieniak, M. Califano, and S. E. Watkins. *Size-dependent valence and conduction band-edge energies of semiconductor nanocrystals.* ACS Nano, 5:5888–5902, 2011.

[15] X. Chen, S. H. Shen, L. J. Guo, and S. S. Mao. *Semiconductor-based photocatalytic hydrogen generation.* Chemical Reviews, 110:6503–6570, 2010.

[16] A. Kudo, and Y. Miseki. *Heterogeneous photocatalyst materials for water splitting.* Chemical Society Reviews, 38:253–278, 2009.

[17] A. T. N'Diaye, S. Bleikamp, P. J. Feibelman, and T. Michely. *Two-dimensional Ir cluster lattice on a graphene moiré on Ir(111).* Physical Review Letters, 97:215501, 2006.

[18] Z. Zhou, F. Gao, and D.W. Goodman. *Deposition of metal clusters on single-layer graphene/Ru(0001): Factors that govern cluster growth.* Surface Science, 604:L31, 2010.

[19] P. Yi, M. Gao, L. Huang, F. Liu, and H. J. Gao. *Directed self-assembly of monodispersed platinum nanoclusters on graphene moiré template.* Applied Physics Letters, 95:093106, 2009.

[20] Q. Liao, H. J. Zhang, K. Wu, H. Y. Li, S.N. Bao, and P. He. *Nucleation and growth of monodispersed cobalt nanoclusters on graphene moiré on Ru(0001).* Nanotechnology, 22:125303, 2011.

[21] M. Sicot, S. Bouvron, O. Zander, U. Rdiger, Y. S. Dedkov, and M. Fonin. *Nucleation and growth of nickel nanoclusters on graphene moiré on Rh(111).* Applied Physics Letters, 96:093115, 2010.

[22] B. Wang, B. Yoon, M. König, Y. Fukamori, F. Esch, U. Heiz, and U. Landman. *Size-selected monodisperse nanoclusters on supported graphene: Bonding, isomerism, and mobility.* Nano Letters, 12:5907, 2012.

[23] A. Chen, and P. H.-Hindle. *Platinum-Based Nanostructured Materials: Synthesis, Properties, and Applications.* Chemical Reviews, 110:3767–3804, 2010.

[24] Z. Peng, and H. Yang. *Designer platinum nanoparticles: Control of shape, composition in alloy, nanostructure and electrocatalytic property.* Nano Today, 4:143–164, 2009.

[25] B. Solsona, T. E. Davies, T. Garcia, I. Vazquez, A. Dejoz, and S. H. Taylor. *Total Oxidation of Propane Using Nanocrystalline Cobalt Oxide and Supported Cobalt Oxide Catalysts.* Applied Catalysis B, 84:176-184, 2008.

[26] B. Solsona, I. Vazquez, T. Garcia, T. E. Davies, and S. H. Taylor. *Complete Oxidation of Short Chain Alkanes Using a Nanocrystalline Cobalt Oxide Catalyst.* Catalysis Letters, 116:116-121, 2007.

[27] L. P. R. Profeti, E. A. Ticianelli, and E. M. Assaf. *Ethanol Steam Reforming for Production of Hydrogen on Magnesium Aluminate-Supported Cobalt Catalysts Promoted by Noble Metals.* Applied Catalysis A, 360:17-25, 2009.

[28] J. Lojewska, A. Koodziej, P. D.-Latka, and A. W.-Birczynska. *Engineering and Chemical Aspects of the Preparation of Micro-structured Cobalt Catalyst for VOC Combustion.* Catalysis Today, 101:81-90, 2005.

[29] G. Busca, M. Daturi, E. Finocchio, V. Lorenzelli, G. Ramis, and R. J. Willey. *Transition Metal Mixed Oxides as Combustion Catalysts: Preparation, Characterization and Activity Mechanisms.* Catalysis Today, 33:239-249, 1997.

[30] A. Fujishima, and K. Honda. *Electrochemical Photolysis of Water at a Semiconductor Electrode.* Nature, 37:238, 1972.

[31] A. T. N'Diaye, J. Coraux, T. N. Plasa, C. Busse, and T. Michely. *Structure of epitaxial graphene on Ir(111).* New Journal of Physics, 10:043033, 2008.

[32] A. B. Preobrajenski, M. L. Ng, A. S. Vinogradov, and N. Mårtensson. *Controlling graphene corrugation on lattice-mismatched substrates.* Physical Review B, 78:073401, 2008.

[33] F. Presel, N. Jabeen, M. Pozzo, D. Curcio, L. Omiciuolo, P. Lacovig, S. Lizzit, D. Alfé, and A. Baraldi.*Unravelling the roles of surface chemical composition and geometry for the graphene–metal interaction through C1s core-level spectroscopy.* Carbon, 93:187–198, 2015.

[34] J. Coraux, A. T. N'Diaye,M. Engler, C. Busse, D. Wall, N. Buckanie, F. J. Meyer zu Heringdorf, R. van Gastel, B. Poelsema, and T. Michely. *Growth of graphene on Ir(111).* New Journal of Physics, 11:023006, 2009.

[35] A. T. N'Diaye, J. Coraux, T. N. Plasa, C. Busse, and T. Michely. *Structure of epitaxial graphene on Ir(111).* New Journal of Physics, 10:043033, 2008.

[36] S. Nie, A. L. Walter, N. C. Bartelt, E. Starodub, A. Bostwick, E. Rotenberg, and K. F. McCarty. *Growth from Below: Graphene Bilayers on Ir(111).* ACS Nano, 5(3):2298–2306, 2011.

[37] C. V.-Van, S. Schumacher, J. Coraux, V. Sessi, O. Fruchart, N. Brookes, P. Ohresser, and T. Michely. *Magnetism of cobalt nanoclusters on graphene on iridium.* Applied Physics Letters, 99(14):142504, 2011.

[38] S. Vlaic, A. Kimouche, J. Coraux, B. Santos, A. Locatelli, and N. Rougemaille. *Cobalt intercalation at the graphene/iridium(111) interface: Influence of rotational domains, wrinkles, and atomic steps.* Applied Physics Letters, 104:101602, 2014.

[39] A. Chaudhury, L. Gragnaniello, T. Ma, S. Surnev, and F. P. Netzer. *Alumina-Supported Array of Co Nanoparticles: Size-Dependent Oxidation Kinetics?* Journal of Physical Chemistry C, 117(35):18112–18119, 2013.

[40] D. Barreca, C. Massignan, D. Barreca, C. Massignan, C. Piccirillo, L. Armelao, and E. Tondello. *Composition and Microstructure of Cobalt Oxide Thin Films Ob-*

tained from a Novel Cobalt(II) Precursor by Chemical Vapor Deposition. Chemistry of Materials, 13 (2):588–593, 2001.

[41] M. Li, and E. I. Altman. *Shape, Morphology, and Phase Transitions during Co Oxide Growth on Au(111).* Journal of Physical Chemistry C, 118(24):12706–12716, 2014.

[42] T. J. Chuang, C. R. Brundle, and D. W. Rice. *Interpretation of the X-ray Photoemission Spectra of Cobalt Oxides and Cobalt Oxide Surfaces.* Surface Science, 59:413-429, 1976.

[43] K. Okada, A. K. Kotani, and B. T. Thole. *Charge Transfer Satellites and Multiplet Splitting in X-ray Photoemission Spectra of Late Transition Metal Halides.* Journal of Electron Spectroscopy and Related Phenomenon, 58:325-343, 1992.

[44] B. W. Veal, and A. P. Paulikas. *Final-state screening and chemical shifts in photoelectron spectroscopy.* Phycical Review B, 31(8):5399-5416, 1985.

[45] J. Ghijsen, L. H. Tjeng, J. van Elp, H. Eskes, J. Westerink, and G. A. Sawatzky. *Electronic structure of Cu_2O and CuO.* Phycical Review B, 38(16):11322-11330, 1988.

[46] T. Kroll, F. Roth, A. Koitzsch, R. Kraus, D. R. Batchelor, J. Werner, G. Behr, B. Büchner, and M. Knupfer. *Absorption and photoemission spectroscopy of rare-earth oxypnictides.* New Journal of Physics, 11:025019, 2009.

[47] K. S. Kim. *X-Ray-Photoelectron Spectroscopic Studies of the Electronic Structure of CoO.* Physical Review B, 11:2177-2185, 1975.

[48] Z. Novotny, F. P. Netzer, and Z. Dohnalek. *Cerium Oxide Nanoclusters on Graphene/Ru(0001): Intercalation of Oxygen via Spillover.* ACS Nano, 9(8):8617–8626, 2015.

[49] R. Larciprete, S. Ulstrup, P. Lacovig, M. Dalmiglio, M. Bianchi, F. Mazzola, L. Hornekær, F. Orlando, A. Baraldi, P. Hofmann, and S. Lizzit. *Oxygen Switching of the Epitaxial Graphene–Metal Interaction.* ACS Nano, 6(11):9551–9558, 2012.

[50] J. Zhang, Q. Z. Xu, C. Feng, M. J. Li, and C. Li. *Importance of the Relationship between Surface Phases and Photocatalytic Activity of TiO_2.* Angewandte Chemical International Edition, 47:1766, 2008.

[51] G. Liu, Y. Zhao, C. Sun, F. Li, G. Q. Lu, and H. M. Cheng. *Synergistic Effects of B/N Doping on the Visible-Light Photocatalytic Activity of Mesoporous TiO_2.* Angewandte Chemical International Edition, 47:4516, 2008.

[52] D. Robert. *Photo-sensitization of TiO_2 by M_xO_y and M_xS_y nanoparticles for heterogeneous photo-catalysis applications.* Catalysis Today, 122:20–26, 2007.

[53] J. H. Park, S. Kim, and A. J. Bard. *Novel Carbon-Doped TiO_2 Nanotube Arrays with High Aspect Ratios for Efficient Solar Water Splitting.* Nano Letters, 6(1):24–28, 2006.

[54] A. Kongkanand, R. M. Dominguez, and P. V. Kamat. *Single wall carbon nanotube scaffolds for photoelectrochemical solar cells. Capture and transport of photo-generated electrons.* Nano Letters, 7:676, 2007.

[55] B. Farrow, and P. V. Kamat. *CdSe Quantum Dot Sensitized Solar Cells. Shuttling Electrons Through Stacked Carbon Nanocups.* Journal of American Chemical Society, 131:11124, 2009.

[56] X. Y .Zhang, H.-P. Li, X.-L. Cui, and Y. Lin, *Graphene/TiO2 nanocomposites: synthesis, characterization and application in hydrogen evolution from water photocatalytic splitting.* Journal of Material Chemistry, 20:2801–2806, 2010.

[57] J. C. Liu, H. W. Bai, Y. J. Wang, Z. Y. Liu, X. W. Zhang, and D. D. Sun. *Self-Assembling TiO_2 Nanorods on Large Graphene Oxide Sheets at a Two-Phase Interface and Their Anti-Recombination in Photocatalytic Applications.* Advanced Functional Materials, 20:4175–4181, 2010.

[58] H. Lin, C.P. Huang, W. Li, C. Ni, S. I. Shah, and Y.-H Tseng . *Size dependency of nanocrystalline TiO_2 on its optical property and photocatalytic reactivity exemplified by 2-chlorophenol.* Applied Catalysis B: Environmental, 68:1–11, 2006.

[59] S. Lizzit, R. Larciprete, P. Lacovig, M. Dalmiglio, F. Orlando, A. Baraldi, L. Gammelgaard, L. Barreto, M. Bianchi, E. Perkins, and Ph. Hofmann. *Transfer-free electrical insulation of epitaxial graphene from its metal substrate.* Nano Letters, 12(9):4503–4507, 2012.

[60] D.Löffler,J.J. Uhlrich,M.Baron,B.Yang,X.Yu,L.Lichtenstein,L.Heinke, C. Büchner, M. Heyde, S. Shaikhutdinov, H. G. Freund, R. Wlodarczyk, M. Sierka, and J. Sauer. *Growth and structure of crystalline silica sheet on Ru(0001).* Physical Review Letters, 105(14):146104, 2010.

[61] T. Matsumoto, M. Batzill, S. Hsieh, and B. E. Koel. *Fundamental studies of titanium oxide-Pt(100) interfaces.I. stable high temperature structures formed by annealing TiO_x films on Pt(100).* Surface Science, 572:127-145, 2004.

[62] G. Lu, S. T. Bernasek, and J. Schwartz. *Oxidation of polycrystalline titanium surface by oxygen and water.* Surface Science, 458:80-905, 2000.

[63] R. Zanoni, G. Righini, A. Montenero, G. Gnappi, G. Montesperelli, E. Traversa, and G. Gusmano. *XPS analysis of sol-gel processed doped and undoped TiO_2 films for sensors.* Surfaces and Interface Analysis, 22:376, 1994.

[64] J. Pouilleau, D. Devilliers, and H. Groult. *Surface study of a titanium-based ceramic electrode material by X-ray photoelectron spectroscopy.* Journal of Materials Science, 32(21):5645–5651, 1997. L. Meng, R. Wu, H. Zhou, G. Li, Y. Zhang, L. Li, Y. Wang, and H. J. Gao. Silicon intercalation at the interface of graphene and Ir(111). Applied Physics Letters, 100(8):083101, 2012.

[65] M. J. Jackman, A. G. Thomas, and C. Muryn. *Photoelectron Spectroscopy Study of Stoichiometric and Reduced Anatase TiO_2(101) Surfaces: The Effect of Subsurface Defects on Water Adsorption at Near-Ambient Pressures.* Journal of Physical Chemistry C, 119(24):13682–13690, 2015.

[66] A. C. Papageorgiou, G. Cabailh, Q. Chen, A. Resta, E. Lundgren, J. N. Andersen, and G. Thornton . *Growth and Reactivity of Titanium Oxide Ultrathin Films on Ni(110).* Journal of Physical Chemistry C, 111(21):7704–7710, 2007.

[67] C. T. Campbell, and S. M. Valone. *Design considerations for simple gas dosers in surface science applications.* Journal of Vacuum & Science Technologies A, 3(2):408-411, 1985.

Chapter 5

Nanographene formation by molecular adsorption of coronene on Ir(111)

This chapter is devoted to investigate the dehydrogenation mechanism of a complex organic molecule, namely coronene, on Ir(111) up to formation of Gr-nanoflakes to get insight on how conformational changes in a molecule can trigger chemical reaction. A number of studies reported the possibility to grow Gr-nanoribbons and nanoflakes on the basis of surface assisted cyclodehydrogenation of suitable precursors [1, 2, 3, 4]. These precursors are playing a key role to control the chemical and transport properties of nanographene and nanoribbons by effectively tailoring the band gap [5, 6, 7]. The band gap problems in Gr can be overcome by exploiting the quantum confinement effects, which allow the modification in the Gr electronic structure by adjusting the width and type of edge termination.

This is very challenging especially in the field of heterogeneous catalysis due to the complicated dissociation mechanism of such large molecules. In fact, they undergo dissociation through different configurations, some of them may bring major changes in chemistry of molecules which may thermodynamically favour some specific reactions to occur [8]. Such molecular configurations are key to the success of many catalytic systems of fundamental interest and practical importance, and worth to be investigated. It is very important to obtain a detailed knowledge of all chemical, structural and electronic transformations involved in these cyclodehdrogenation processes to find efficient routes to fabricate nanographene and nanoribbons with tailored properties and to use these conformational changes to effect the kinetics of

specific chemical reactions.

In order to get insight into the dissociation mechanism of such large molecule, we choose coronene ($C_{24}H_{12}$) and study its thermally assisted cyclodehydrogenation process. The dehydrogenation path, which includes molecular lifting, twisting and curling, was characterized by a combination of several different experimental techniques, including X-ray absorption spectroscopy, photoelectron spectroscopy, electron diffraction, and thermal desorption spectroscopy. These experimental findings were complemented by DFT calculations performed by a collaborating group at the University College London in order to get the atomistic details of the process.

5.1 Coronene adsorption on Ir(111)

The Ir(111) single crystal used in this experiment was cleaned using the procedure described in chapter two, which was optimized to ensure a high-quality surface, as judged by LEED and XPS. All the measurements reported in this chapter were performed in UHV conditions with a base pressure of the order of 1×10^{-10} mbar. We use commercially available coronene powder (99%, purified by sublimation). Coronene molecules were evaporated using a evaporator consisting of a Boron Nitride crucible wrapped with a 1 mm diameter Ta wire used to heat it by resistive dissipation. The crucible was annealed in vacuum to increasing temperatures up to 670 K before the experiment, in order to outgas the evaporation cell. The temperature inside the crucible was measured through a K-type thermocouple which is in thermal contact with the coronene powder. The evaporation of Coronene was achieved by keeping the crucible at a fixed temperature in the $400 \div 440$ K range. Coronene was further purified by means of short annealing cycles up to 450 K before each evaporation while monitoring the chamber residual gas composition with a residual gas analyzer. During evaporation the Ir(111) sample was kept at room temperature.

Figure 5.1 shows the C K-edge absorption spectra measured for sub-ML coverage of coronene at two different incident angles. The resonances in the 284 to 289 eV range are ascribed to C 1s$\rightarrow \pi^*$ transitions, while the features above 290 eV are assigned to C 1s$\rightarrow \sigma^*$ transitions, in good agreement with previous results [9]. The multiple components present in each spectral region can be explained in

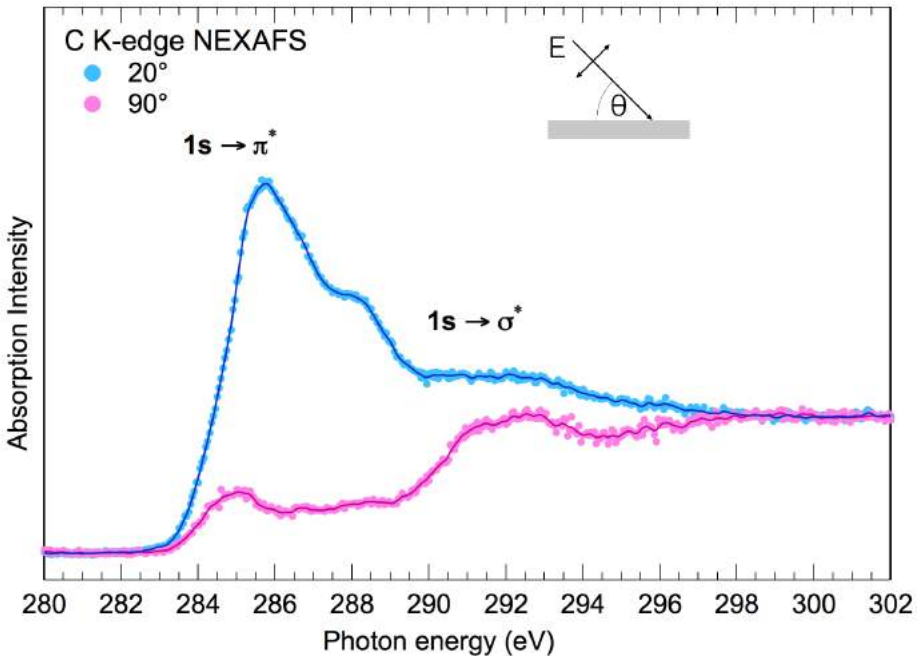

Figure 5.1: C K-edge NEXAFS spectra acquired after deposition of sub-monolayer coverage of coronene on Ir(111) at room temperature. The spectra were acquired with linearly polarized radiation, with the electric field either parallel (pink dots) or almost normal (blue dots) to the crystal surface. Corresponding smoothed spectra (solid lines) are also presented.

terms of C 1s→LUMO+n transitions, along with initial state effects given by the presence of non- equivalent C atoms due to the interaction with the surface. The most prominent feature is the strongly reduced intensity of the C 1s→ π^* transition components and the increased spectral weight in the σ^* region when the electric field is almost normal to the surface (blue curve), indicating a nearly flat adsorption geometry. The σ^* molecular orbitals for sp^2 C compounds, like coronene, are parallel to the molecular plane, while the π^* are normal to it. This shows that if the molecules lie flat on the surface, the C 1s→ σ^* transition probability is maximized when the impinging electric field vector is parallel to the surface, while C 1s→ π^* transitions are maximized when the electric vector is normal to the surface.

The strong modification in the electronic structure of coronene upon adsorption is confirmed by the UPS results reported in Fig. 5.2. These valence band spectra have been measured at normal emission at 34 eV photon energy after different surface preparations. The spectrum acquired after deposition of a monolayer of coronene on clean Ir(111) (red curve), shows several peaks associated to molecular

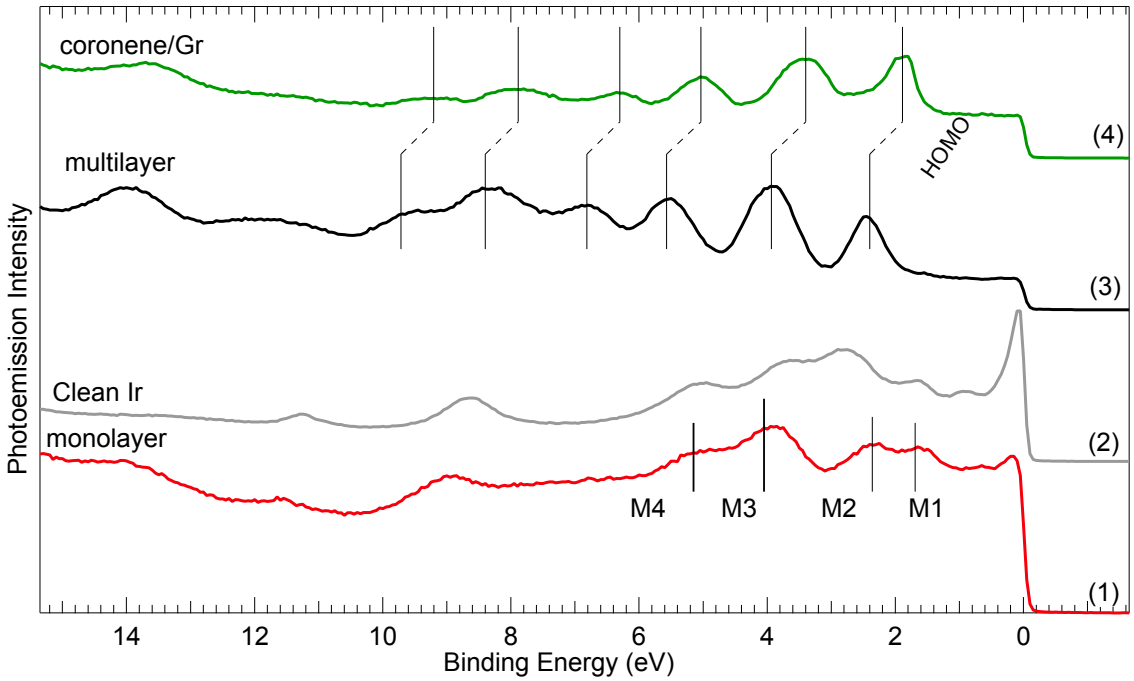

Figure 5.2: Valence band spectra acquired at 34 eV photon energy for monolayer coronene on Ir(111) (1, red curve), clean Ir(111) (2, gray curve), multilayer coronene on Ir(111) (3, black curve), and monolayer coronene on graphene/Ir(111) (4, green curve).

signals appearing at different binding energies with respect to those present in the spectrum of clean Ir(111) (gray curve), which is dominated by the large d-band density of states. These molecular states can be associated with non-dispersing features in the ARPES maps as shown in Fig. 5.3 (c,d), and underlined also by an Energy Dispersion Curve acquired near the M point, where the substrate density of state is almost flat (see Fig. 5.3 (a,b)). There are four peaks (M_{1-4}) at 1.8, 2.4, 4.1 and 5.2 eV, attributed to hybridization of the coronene molecular orbitals with the Ir 5d bands. That the surface Ir(111) has the ability in creating strong π bonds to poly aromatic hydrocarbons is confirmed by considering the spectral components appearing for other coronene-based interfaces with weaker interactions, i.e. coronene multi-layers grown on Ir(111) (see Fig. 5.2, black curve) and for coronene on Gr/Ir(111) (see Fig. 5.2, green curve). In these cases, besides the rigid shift induced by different charge transfer, the spectra are a clear fingerprint of the coronene molecular orbitals (E_{2u}, B_{1g}, B_{2g}, E_{1g}, E_{2u}, A_{2u}, E_{2g}, marked with vertical lines in the Fig. 5.2), whose BE distribution is in excellent agreement with previous experimental and theoretical findings [10, 11, 12].

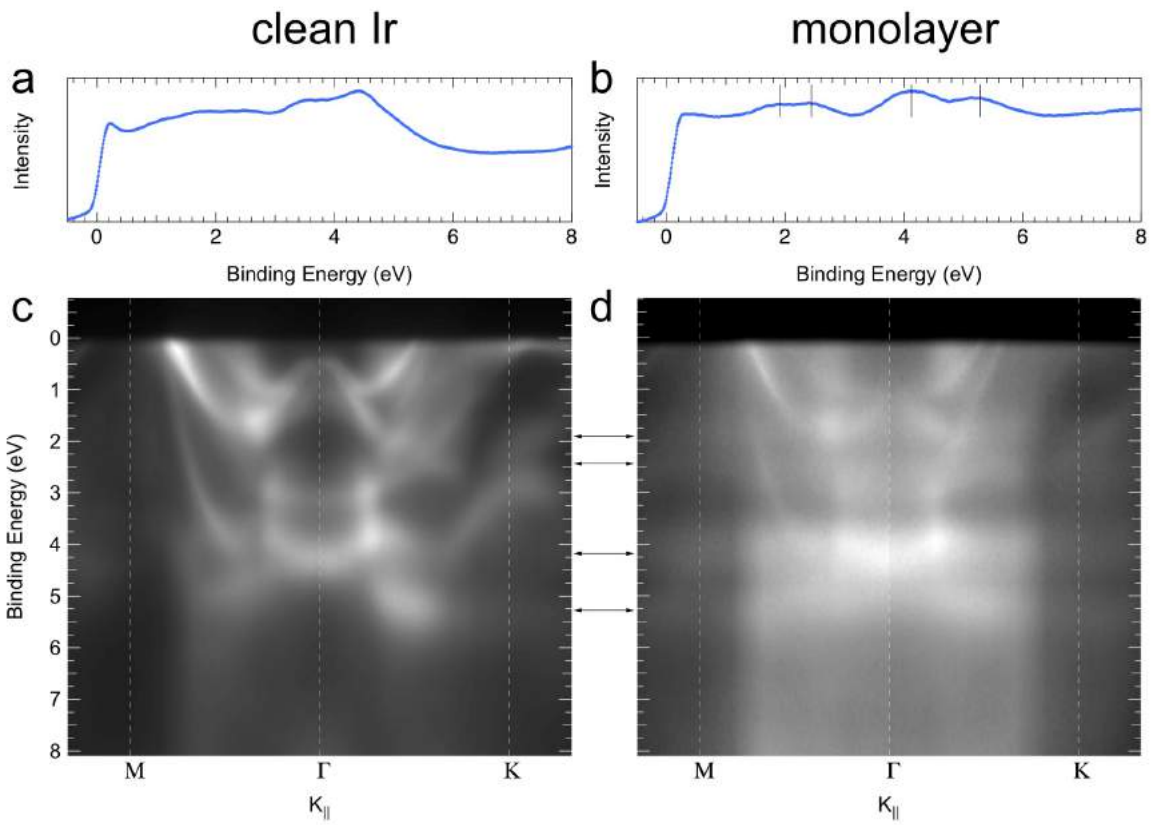

Figure 5.3: (a) Energy Dispersion Curve for the clean Ir(111) obtained by selecting a vertical cut of the ARPES image below at the M point. (b) EDC curve for a monolayer of coronene on Ir(111) obtained by selecting a vertical cut of the ARPES image below at the M point. The molecular levels are shown superimposed (vertical bars). (c) ARPES map along the M-Γ-K direction for the clean Ir(111) acquired at *hv*=34 eV. (d) ARPES map along the M-Γ-K direction acquired (*hv*=34 eV) after deposition of a monolayer of coronene on Ir(111). The four clearly visible non-dispersing molecular levels are marked with arrows.

Further insight into the modification of the coronene electronic structure induced upon adsorption was gained by C 1s core level spectra at different molecular coverages (see Fig. 5.4, shades of blue). In contrast to the two-peak line shape observed for coronene on Gr (pink curve) and for gas phase coronene [9] we observe three-peak spectral shape for different coverages. However, the C 1s spectral line shape is same regardless of the coronene amount, suggesting that the adsorption configuration and site are not modified by intermolecular interactions in denser molecular layers. The presence of three components cannot be simply justified as due to the geometrically non equivalent C atoms forming the inner, middle and outer rings in the molecule, since the spectral weight does not match the 1:1:2 ratio

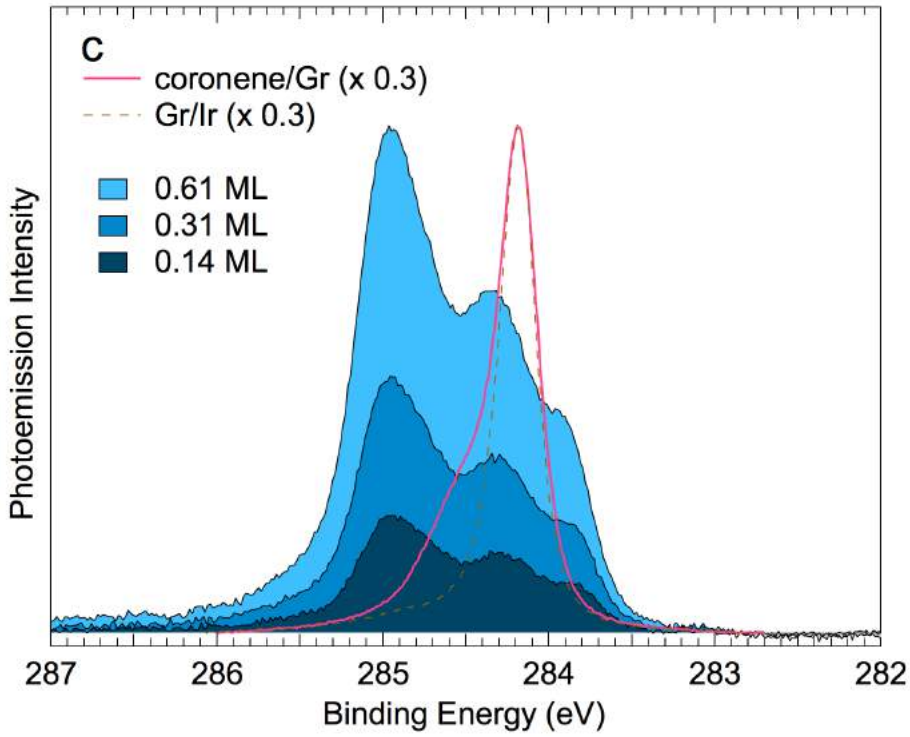

Figure 5.4: C 1s spectra acquired at *hv*=400 eV for different coverages of coronene on Ir(111) (shades of blue), compared with monolayer coronene on graphene/Ir(111) (pink curve) and pristine graphene on Ir(111) (dotted curve).

corresponding to the population of those atoms.

In order to further shed light on the coronene adsorption geometry and on the origin of the different core-level components, we performed DFT calculations. These calculations were performed for a single coronene molecule adsorbed on a 9×9 Ir surface. The different coronene configurations that were probed, are shown in Fig 5.5, including molecules with symmetry axes oriented along different directions, in different adsorption sites and also in non-planar configurations.

The minimum energy configuration corresponds to coronene adsorbed with the inner C hexagon in bridge-site and the molecular axis aligned parallel to the [101] direction of Ir(111) (see Fig. 5.6 (c)). The molecules assume a bowl-like shape (side view shown in Fig. 5.6 (b)), usually associated with π-conjugated compounds known as buckybowls or π-bowls [13, 14]. These species have been found to commonly form stable adlayers on metal surfaces, as in the case of corannulene ($C_{20}H_{10}$) on Cu(110) [15, 16] and of sumanene ($C_{21}H_{12}$) on Ag(111) [17]. In our case, the adsorbed molecule develops its bowl opening upward: C atoms in the inner ring are about

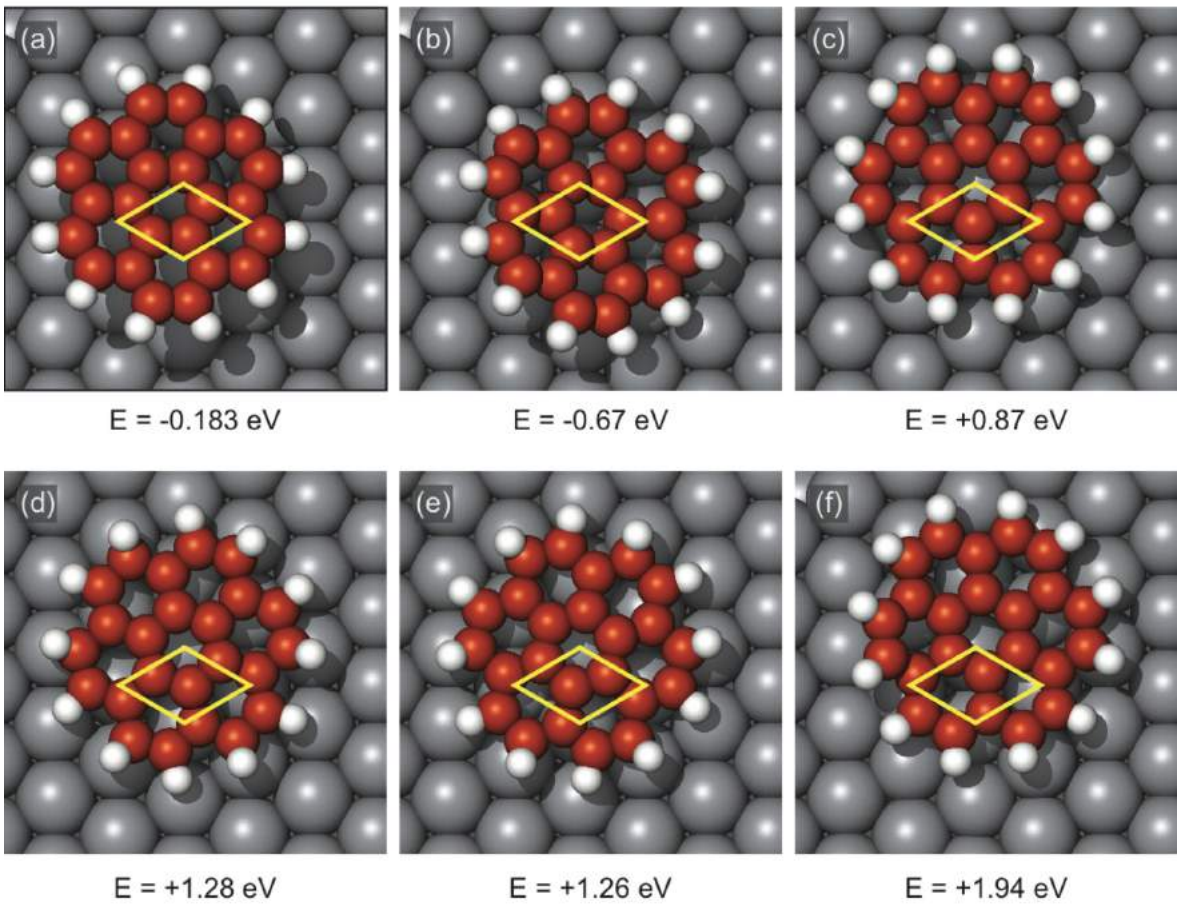

Figure 5.5: Additional adsorbed molecular configurations probed by DFT. The yellow parallelogram in each panel represents the substrate elementary cell, with each corner on a top position. The adsorption energies are calculated with respect to the gas phase molecule configuration.

0.23 Å closer to the surface with respect to C atoms in the outer ring (see Fig. 5.6 (a)). The bowl-shaped geometry is enhanced by the hydrogen atoms displaying an average height of 2.74 Å, 0.7 Å farther from the surface than the inner C atoms, and a C-H bond angle ranging from 22° to 39° with respect to the Ir surface plane.

In order to test the consistency of the minimum energy adsorption structure we compared in Fig. 5.6 (d) the experimental C 1s core-level spectra (empty circles), for which the molecule-substrate interaction is expected to have a strong influence, and fit results (solid line). We computed the C 1s core-level binding energy (BE) for each of the 24 C atoms of the coronene molecules, including also final state effects due to core-hole screening. The results, illustrated in Fig. 5.6 (d), show that the computed BEs for the carbon atoms in the coronene molecule are not only linked to some extent

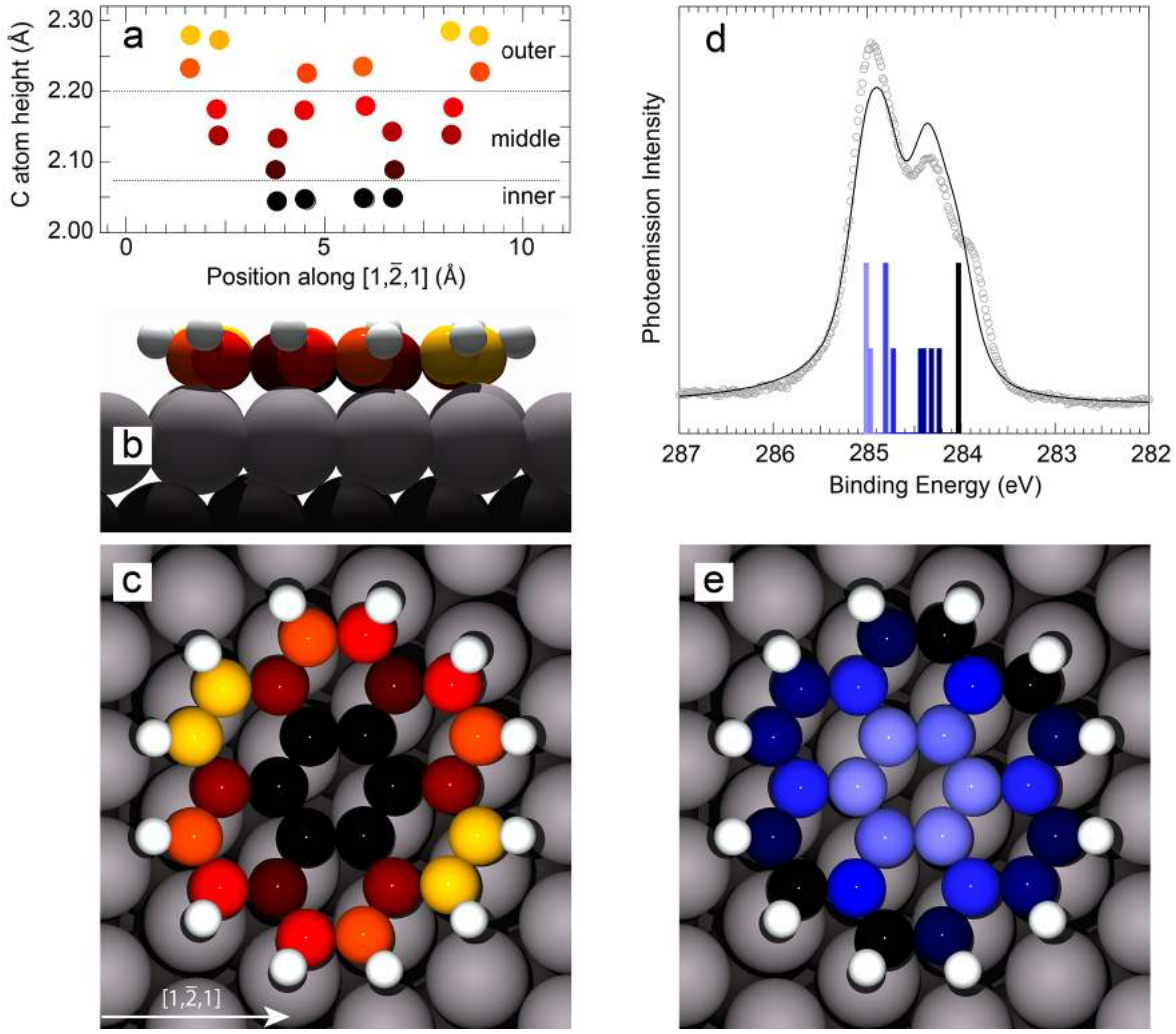

Figure 5.6: (a) Carbon-iridium distance for the non-equivalent C atoms of the coronene molecule. (b,c) Illustration of the side and top views of the $C_{24}H_{12}$ molecular orientation as found in DFT calculations. The color scale reflects the separation between the C atoms and the substrate beneath. Small differences in the C-Ir distance between apparently equivalent C atoms can be accounted for by considering the small influence of the second Ir layer, which breaks the 6-fold symmetry of the first atomic layer. (d) C 1s spectrum measured at normal emission and $h\nu$ = 400 eV (empty circles) together with the fit result (solid line) and the calculated spectral distribution originated from the 24 C atoms. (e) Color scale in the model reflects the BEs of the different C 1s calculated components.

to the carbon-metal distance (C atoms in the central ring showing the highest BEs), but are strongly dependent on the positions with respect to the first-layer Ir atoms. This is especially true for those C atoms sitting in the outer ring and bonded to H atoms, whose C 1s BE depends on the degree of interaction with the substrate Ir atoms, besides the bond with H instead of another C. The good agreement between

experimental data and fit results strongly supports the DFT calculated molecular adsorption geometry.

5.2 Temperature promoted coronene dehydrogenation

In order to explore the mechanism of coronene dissociation we initially employed TPD, in the temperature range 150-590 K, to figure out the threshold of hydrogen desorption (m/z=2), which can be used as fingerprint of C-H break-up. The desorp-

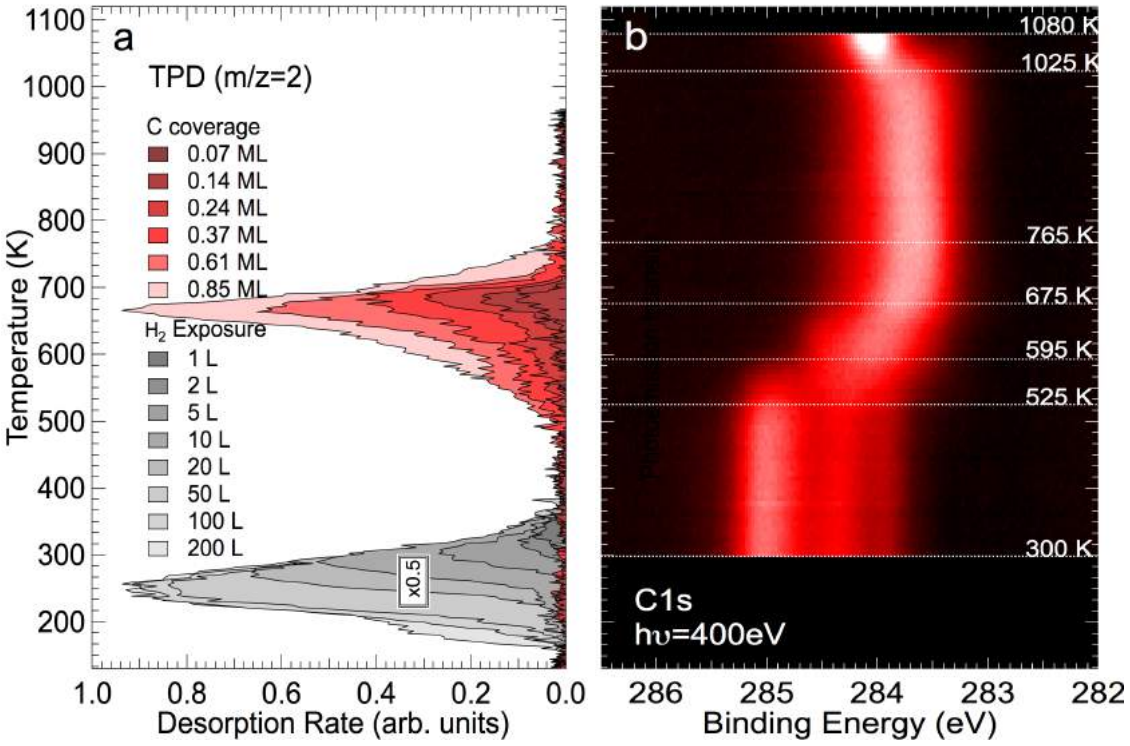

Figure 5.7: (a) Temperature programmed desorption spectra of m/z = 2 after coronene deposition at T = 300 K (red scale), and after molecular hydrogen adsorption at T = 100 K (gray scale, intensity rescaled by a factor 0.5). (b) Temperature-dependent C 1s core-level spectra (about 100 spectra) shown as a two-dimensional intensity plot.

tion spectra corresponding to different coronene coverages, reported in Fig. 5.7 (a) (in red scale), indicate that the gas phase H_2 can be detected only above 500 K, with a maximum desorption rate around 650 K. In order to verify that the molecules do not undergo any dissociation at room temperature, we compared the TPD data to a similar H_2 desorption experiment starting from hydrogen adsorbed on clean Ir(111) at

100 K which is shown with gray scale in Fig. 5.7 (a). The H_2 adsorbs dissociatively on Ir(111) [18, 19] and the onset of desorption is indicative of the recombination of two H atoms after surface diffusion. The large difference in H_2 formation temperature and lack of any overlap in the temperature scale of the two desorption experiments, is an indication that the coronene molecules do not dissociate upon adsorption and the first C-H breakup occurs only around 500 K.

The dissociation of coronene was monitored in-situ by means of fast-XPS measurements. The C 1s core level spectrum during a linear temperature ramp (0.25 K/s) from 300 to 1080 K is reported as 2D plot in Fig. 5.7 (b). As expected from the desorption measurements, the spectrum does not change in the initial stage of the ramp, as we discuss above and clear modifications are observed above 525 K, corresponding to the onset of H_2 desorption. The spectral weight shifts to lower BE, reaching a stable situation above 700 K, when the TPD results shows that all the hydrogen atoms have desorbed. The C 1s signal starts shifting back to higher BE above 1000 K eventually reaching the value of 284.10 eV at 1050 K, which is a clear fingerprint of graphene formation [20, 21]. It is important to mention that, during the dissociation process, there is no loss in the overall C 1s intensity, suggesting that the energy barrier for C-H bond cleavage is significantly lower than that for desorption of the intact molecule or C containing species.

In order to gain an insight on the atomistic details of the kinetics of coronene dissociation to classify the C 1s spectral sequence, extensive DFT calculations were performed for the energy barriers between the computed intermediate species, using the Nudged Elastic Band (NEB) method [22]. The twelve intermediate configurations corresponding to the energetically most favorable reaction pathway for breaking the C-H bonds in n sequential steps (with n from 1 to 12) are reported in Fig. 5.8, leaving the dehydrogenated molecules and an additional single H atom on the surface. The energy diagrams reported below each configuration are given with respect to the energy of the n-1 configuration, being n=0 the intact coronene molecule. It is worth stressing that, despite the higher final state energy of each dehydrogenation step, the reaction can easily proceeds because, at the temperatures of our experiments, the H atoms can diffuse very rapidly on the surface and form H_2 that immediately desorbs, thus preventing the reverse reaction. Close inspection of the images shown in Fig.

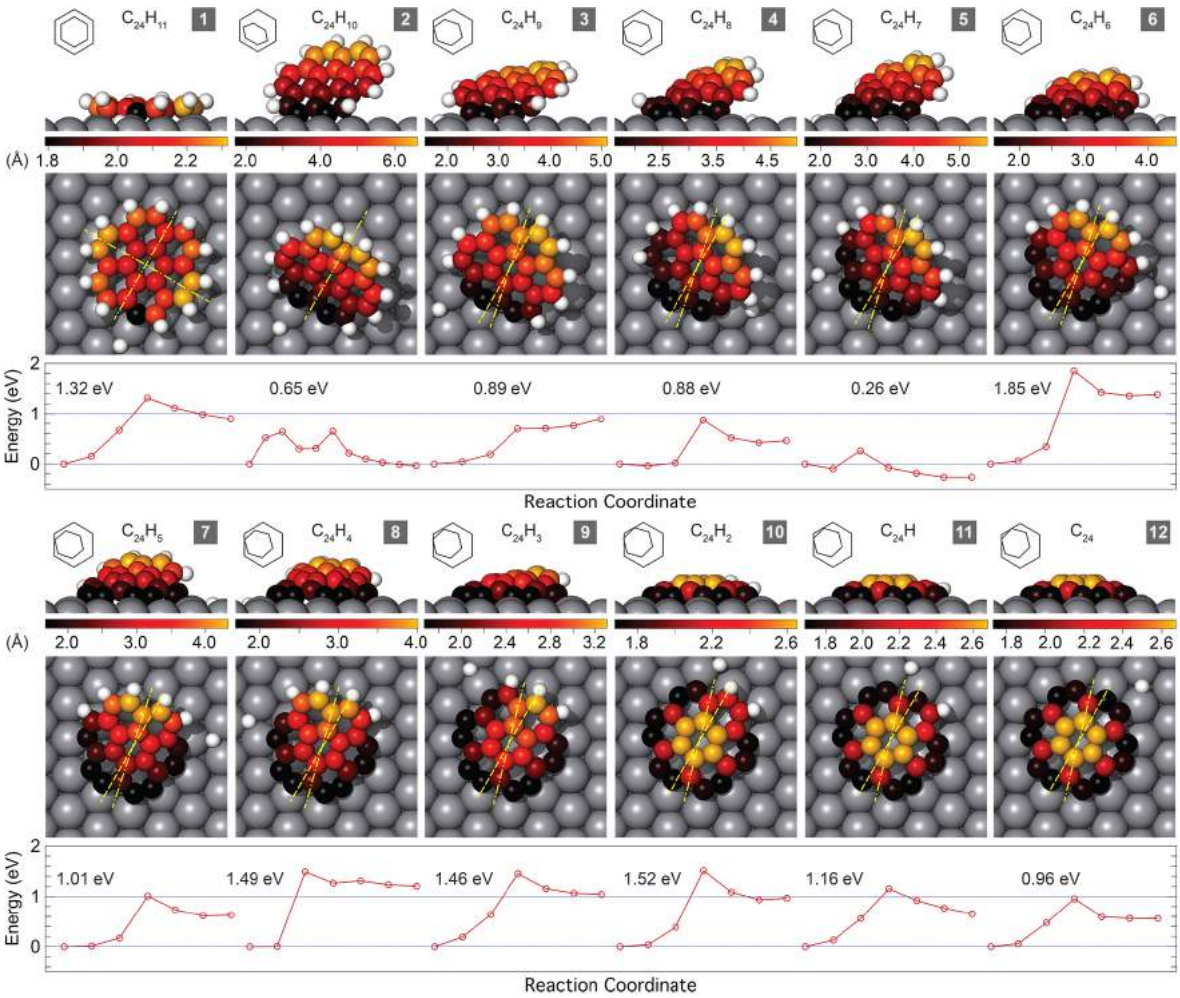

Figure 5.8: Illustration of the side and top views of the $C_{24}H_n$ dehydrogenation through the sequential cleavage of the n = 12 C-H bonds. Different colors correspond to different C-metal substrate heights. The colors have been rescaled in each step to emphasize the geometrical differences in each configuration (the height scale in Å is also reported for each step of the reaction). Above each illustration, a schematic representation of the coronene to Ir relative orientation is reported. Yellow dash-dotted lines in steps 1-2 represent the symmetry axes shared by the adsorbed coronene molecule and the Ir substrate. In steps n = 3-12, the dashed line represents the original coronene orientation, while the dash-dotted line represents the current one.

5.8 outlines the dissociation path that the molecules undergo up to the formation of nanographene flakes. The stepwise dehydrogenation mechanism appears to be driven by the proximity of the C outer ring atom to the final adsorption position. The coronene molecules upon adsorption have significant internal C-C strain with respect to the gas phase configuration (see Fig. 5.9). The dissociation begins (see Fig.

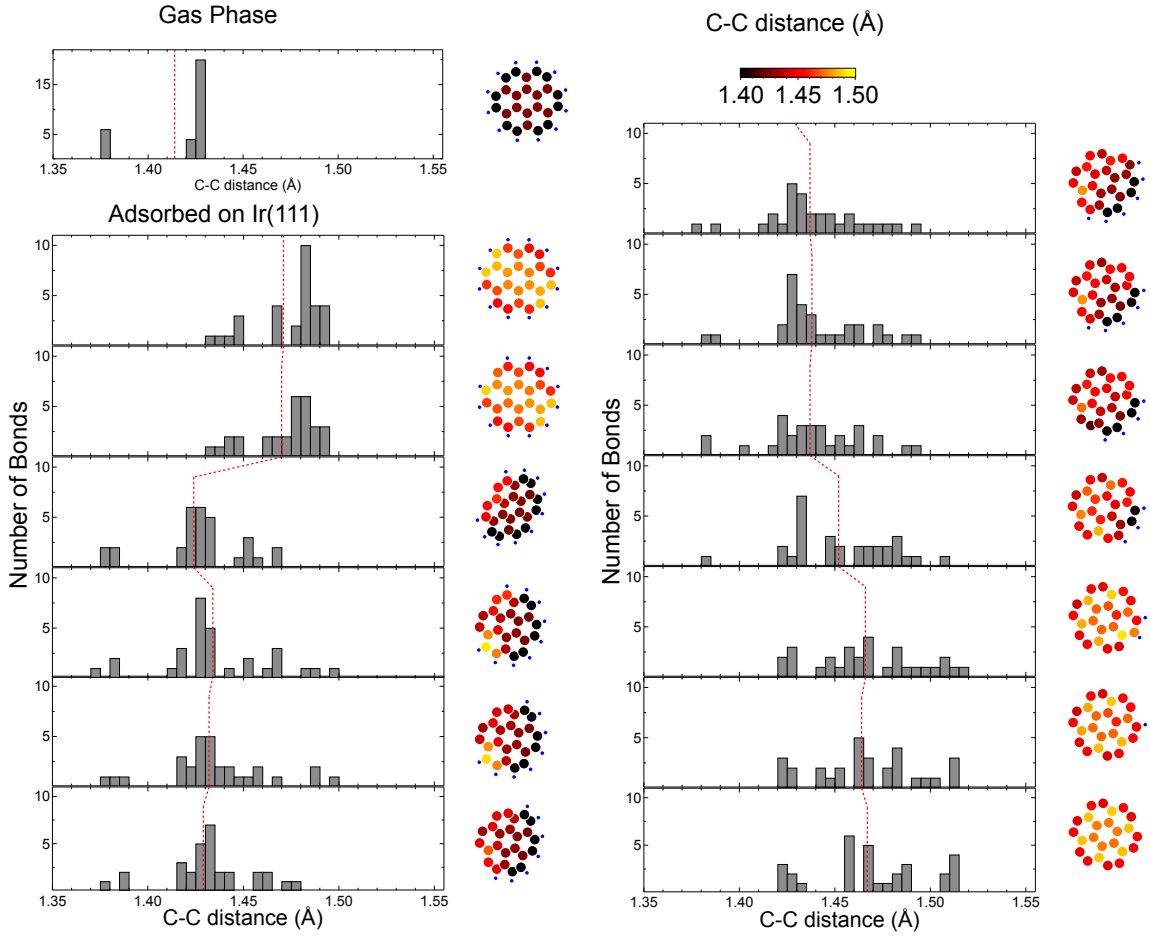

Figure 5.9: (left) C-C bond length histograms for gas phase (top), and adsorbed coronene during dehydrogenation, as obtained from DFT calculations. All the 30 C-C bonds were included. The average C-C bond length for each dissociation step is also reported (dashed red line). (right) Schematic representation of gas phase (top), and adsorbed coronene during dehydrogenation of Ir(111). The C atoms are coloured according to the mean distance from the 3 (or 2) nearest neighbours. The colour scale is reported on top.

5.8, n=1) from one of the four equivalent peripheral C atoms closest to the Ir surface top position, which, after the C-H bond cleavage, binds strongly to the surface Ir atoms, approaching its preferred adsorption site, much closer to the surface. The next dissociation step causes a sudden lifting of the molecule with respect to the surface plane (Fig. 5.8, n=2), resulting in an almost complete internal strain relief (see Fig. 5.9). In fact, three peripheral C atoms are found in equivalently favorable sites, giving therefore three candidates C-H bonds for the next dehydrogenation. However, the lifting of the molecule, which was found to give a 0.67 eV energy gain with respect to the minimum energy flat configuration, implies the breaking of C-H bond closest to

the previously dehydrogenated one. At this point, one symmetry axis of the molecule with respect to the substrate still remains. Always keeping in mind that the driving mechanism for dehydrogenation is the proximity of the peripheral C atom to a top site, the two C atoms, adjacent to the freshly dehydrogenated carbons, are found to be equivalent. The evolution of the system toward the state (Fig. 5.8, n = 3) results in a clear twist of the molecule in one direction, in order to better accommodate the newly dehydrogenated C atom in its favored bond site on the substrate. This causes the loss of the second symmetry axis, and the remaining evolution of the dissociation reaction is fully determined.

It is significant that during the dehydrogenation process also the atoms of the Ir substrate are slightly rearranged, in particular becoming more elevated with respect to the average surface plane, which eventually contributes to the formation of a stronger molecule-Ir bond. From this step on, the molecule evolves by gradually completing the rotation to the final adsorption geometry, and by curling toward a dome shape configuration, always losing H atoms next to dehydrogenated bonds. This gradually changing shape increases the internal strain of the part attached to the substrate, while always keeping one end lifted until the very end, allowing for some strain to be relieved in the lifted portion of the molecule during the intermediate steps. The topology during the dissociation process is also affected by the contributions of the σ and π orbital overlap with the substrate d-bands, the former tending to cause the C rings to stand perpendicular to the surface, the latter trying to push the C ring parallel to it. The final state configuration is very similar to what has been found for the initial stages of growth of graphene using ethylene: dome-shaped C nanoislands whose interactions with the Ir substrate take place only at the cluster edges [23]. With increasing temperature, the mobility of the nanodomes becomes large enough to permit the formation of larger clusters and eventually graphene [24].

In order to confirm the reaction intermediates, we simulated the C 1s core-level spectra for all the carbon atoms of the intermediate species. Fig. 5.10 (b) reports a series of simulated spectra together with the experimental one, showing an excellent agreement. Starting from a three component line shape, associated to $C_{24}H_{12}$ and $C_{24}H_{11}$ molecules, the C 1s spectra, above 525 K, changes shape and shifts to lower BE, as observed, for example, for $C_{24}H_{10}$ and $C_{24}H_{7}$, eventually

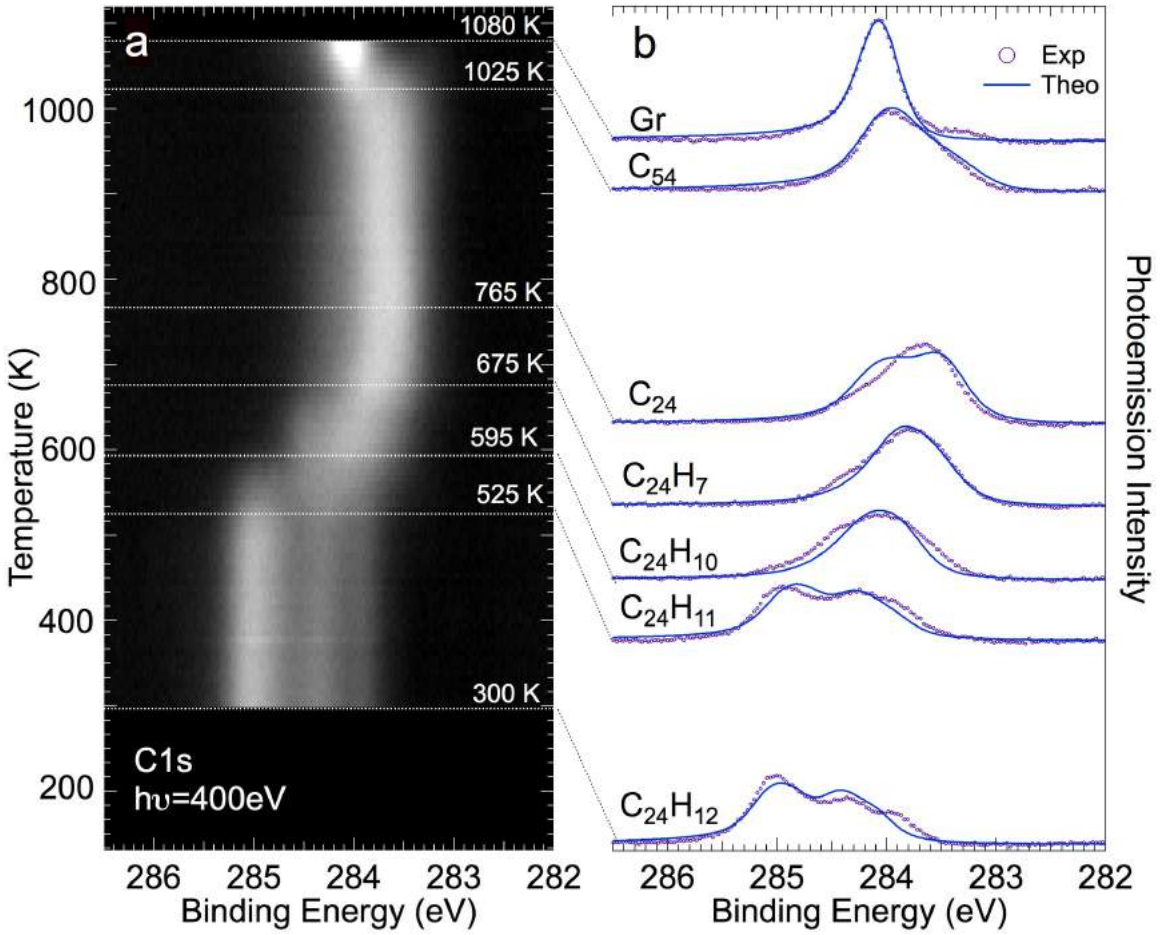

Figure 5.10: 2D plot of the temperature dependent C 1s core level spectra (about 100 spectra). (b) Comparison between experimental (purple) and DFT simulated (blue) selected C 1s core-level spectra.

forming the nanodomes around 765 K. The clusters nucleate to form larger islands and the spectral distribution becomes narrower at higher temperature (see simulated spectrum corresponding to the graphene flake formed by 54 C atoms - C_{54}). The single peak at 284.1 eV, fingerprint of graphene formation on Ir(111), appears only at the highest temperature (1080 K).

Though the process illustrated in Fig. 5.8 is the most energetically favorable, we also tested many other reaction paths that revealed striking differences in terms of geometry, and do not include the process of molecular lifting and curling. For example we found that an alternative possibility is that, after the first dehydrogenation, the molecules break the next C-H bond but still remain flat on the surface. However, the final state is 0.67 eV higher in energy. Moreover, the evolution of the reaction

following this new sequence would end up with a C_{24} carbon cluster in a geometrical configuration that is not energetically favorable. However, it is important to stress that the unrotated C cluster, i.e. the one presenting the same azimuthal orientation as the original coronene molecule, has a 2.27 eV higher energy. Notably, the reaction path involving the flat dissociation behavior results in a calculated C 1s core-level spectrum with an additional component growing at lower BE (at 282.9 eV), which is not experimentally observed. In fact, during the flat dissociation pathway, some Ir atoms that bind to peripheral C atoms of the partially dissociated molecule, are also bound to another C atom. This produces the theoretically predicted, but not experimentally observed, low BE component in the C 1s spectrum.

We have compared the experimental $C_{24}H_{12}$ coverage evolution with temperature, as extracted from the C 1s photoemission data (see Fig. 5.11), with a theoretical prediction based on a micro-kinetic model, assuming that the reaction rate depends on the activation energy of the first C-H bond breaking reaction step through a Boltzmann factor, with the energy barrier provided by the NEB calculations. The temperature behavior is in good agreement with the experimentally observed decrease of the $C_{24}H_{12}$ population when the pre-exponential factor is equal to 10^{10}. This value, which could seem small if compared with the typical value of 10^{13}, is reasonable if we consider that the pre-factors for dissociation reactions are typically $1/10$ to $1/10^5$ of the pre-factors for desorption of the same molecule [25]. It is intriguing to compare our results with the simplest aromatic molecules like benzene (C_6H_6) [26]. Theoretical calculations of benzene adsorption on Cu(100) show that, after the first hydrogen scission starting from its flat adsorption configuration, also the phenyl radical C_6H_5 and the ortho-benzyne species C_6H_4 assume upright configurations. It is interesting to observe that the dissociation of benzene on Pt(111), which is a transition metal quite similar to Ir, results in a tilted configuration with the C atoms bonded to a top site [27]. In our case the results suggest that the process of thermally activated molecular lifting in the dissociation process of similar molecules can be a more general behavior, also for larger PAHs. We suppose that this is the case for other transition metal surfaces, where the presence of unsaturated C bonds could lead to the development of strong interactions between the partially dehydrogenated molecules and the metal substrates. The main driving force resulting in the tilt

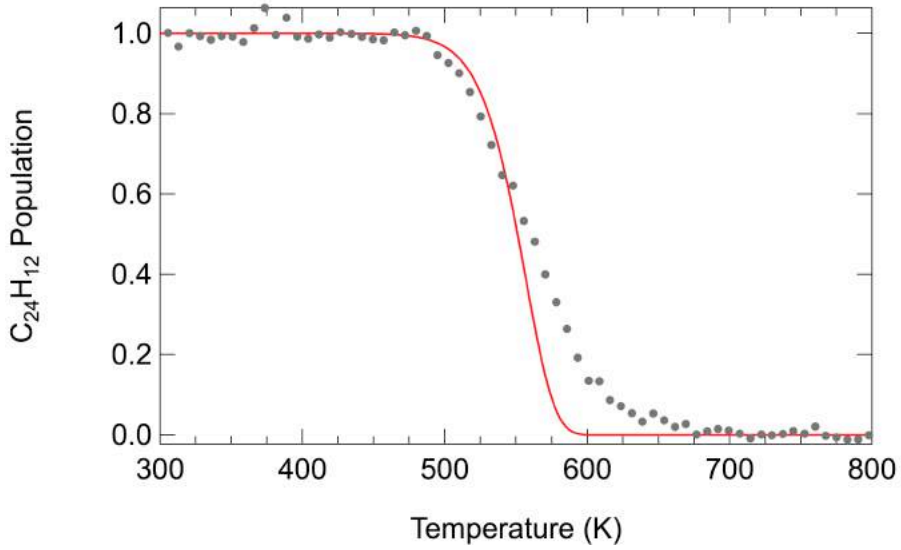

Figure 5.11: (gray dots) Experimentally deduced $C_{24}H_{12}$ population during the annealing ramp and (red curve) theoretical desorption model.

and rotation of the molecule before curling, *i.e.* the creation of new bonds with the substrate which breaks the molecular symmetries and allows for some internal strain relief, somehow mimics what happens in the case of heterocyclic aromatic adsorbates such as pyridine, pyrrole, and thiopene for which, besides flat-lying configurations, also tilted geometries have been discussed previously [26].

In conclusion, using a multimethod experimental approach and extensive theoretical calculations, we have shown that coronene molecules adsorbed on Ir(111) undergo major conformational changes during the dissociation process, which bring the molecules from a flat, slightly upward-pointing bowl shape to graphene through a series of exotic configurations. Upon the second C-H bond cleavage, the molecules tilt upward with respect to the surface, and then rotate to accommodate the reactive C terminations to the most favorable bond site with the substrate. As the reaction proceeds, the molecules gradually settle down to form peculiar dome-shaped nanographene islands. Higher temperatures promote the surface diffusion of the nano-domes, which result in the formation of larger C islands and eventually, above 1050 K, in single layer Gr [23].

This study of dehydrogenation mechanism of large organic molecules could be exploited to create new materials with different functionalities by encapsulating single adatoms below the carbon dome, trough diffusion of the new species under-

neath the carbon disk just before the molecular crowding. We hope that our studies could inspire further to investigate different precursor to tailor band-gap by very narrow nanoribbons with edge termination [28]. Pyridine derivatives with graphene nanoribbons can constitute a novel and well-defined heterogeneous electrocatalyst with good stability and tunable active sites for the ORR, which provides a useful guidance to develop the next-generation of low-cost and metal-free electrocatalysts [29]. We strongly believe that this study both (experimentally and theoretically) explains well the complex dehydrogenation mechanism of large organic molecules, which could facilitate various synthetic transformations. Similar system could be investigated to get control over surface structure and chemical composition (conformationally controlled chemical reactions) in nano-catalysis for more efficient catalytic systems.

Bibliography

[1] J. Cai, P. Ruffieux, R. Jaafar, M. Bieri, T. Braun, S. Blankenburg, M. Muoth, A. P. Seitsonen, M. Saleh, X. Feng, K. Müllen, and R. Fasel. *Atomically precise bottom-up fabrication of graphene nanoribbons.* Nature, 466(7305):470–473, 2010.

[2] M. Treier, C. A. Pignedoli, T. Laino, R. Rieger, K. Müllen, D. Passerone, and R. Fasel. *Surface-assisted cyclodehydrogenation provides a synthetic route towards easily processable and chemically tailored nanographenes.* Nature Chemistry, 3(1):61–67, 2011.

[3] P. Ruffieux, J. Cai, N. C. Plumb, L. Patthey, D. Prezzi, A. Ferretti, E. Molinari, X. Feng, K. Müllen, C. A Pignedoli, and R. Fasel. *Electronic structure of atomically precise graphene nanoribbons.* ACS Nano, 6(8):6930–6935, 2012.

[4] L. Talirz, H. Söde, J. Cai, P. Ruffieux, S. Blankenburg, R. Jafaar, R. Berger, X. Feng, K. Müllen, D. Passerone, R. Fasel, and C. A. Pignedoli. *Termini of bottom-up fabricated graphene nanoribbons.* Journal of the American Chemical Society, 135(6):2060–2063, 2013.

[5] M. Y. Han, B. Özyilmaz, Y. Zhang, and Ph. Kim. *Energy band- gap engineering of graphene nanoribbons.* Physical Review Letters, 98(20):206805, 2007.

[6] L. Yang, C. H. Park, Y. W. Son, M. L. Cohen, and S. G. Louie. *Quasiparticle energies and band gaps in graphene nanoribbons.* Physical Review Letters, 99(18):186801, 2007.

[7] Y. W. Son, M. L. Cohen, and S. G. Louie. *Energy gaps in graphene nanoribbons.* Physical Review Letters, 97(21):216803, 2006.

[8] M. E. Chiu, D. J. Watson, G. Kyriakou, M. S. Tikhov, and R. M. Lambert. *Tilt the Molecule and Change the Chemistry: Mechanism of S-Promoted Chemoselective Catalytic Hydrogenation of Crotonaldehyde on Cu(111).* Angewandte Chemie, 118:7692-7696, 2006.

[9] G. Fronzoni, O. Baseggio, M. Stener, W. Hua, G. Tian, Y. Luo, B. Apicella, M. Alfé, M. de Simone, A. Kivimäki, and M. Coreno. *Vibrationally resolved high-resolution NEXAFS and XPS spectra of phenanthrene and coronene.* The Journal of Chemical Physics, 141(4):044313, 2014.

[10] R. Boschi, E. Clar, and W. Schmidt. *Photoelectron spectra of polynuclear aromatics. III. The effect of nonplanarity in sterically overcrowded aromatic hydrocarbons.* The Journal of Chemical Physics, 60(11):4406– 4418, 1974.

[11] P. G. Schroeder, C. B. France, B. A. Parkinson, and R. Schlaf. *Orbital alignment at p-sexiphenyl and coronene/layered materials interfaces measured with photoemission spectroscopy.* Journal of Applied Physics, 91(11):9095–9107, 2002.

[12] K. Medjanik, D. Kutnyakhov, S. A. Nepijko, G. Schönhense, S. Naghavi, V. Alijani, C. Felser, N. Koch, R. Rieger, M. Baumgarten, and K. Mullen. *Aromatic Molecular-Bowl Hydrocarbons: Synthetic Derivatives, Their Structures, and Physical Properties.* Physical Chemistry Chemical Physics, 12(26):7184-7193, 2010.

[13] Y.-T. Wu, and J. S. Siegel. *Electronic structure of large disc-type donors and acceptors.* Chemical Reviews, 106(12):4843-4867, 2006.

[14] V. M. Tsefrikas, and L. T. Scott. *Geodesic Polyarenes by Flash Vacuum Pyrolysis* Chemical Reviews, 106(12):4868-4884, 2006.

[15] M. Parschau, R. Fasel, K.-H. Ernst, O. Gröning, L. Brandenberger, R. Schillinger, T. Greber, A. P. Seitsonen, Y.-T. Wu, and J. S. Siegel. *Buckybowls on Metal Surfaces: Symmetry Mismatch and Enantio-morphism of Corannulene on Cu(110).* Angewandte Chemical Internationl Edition, 46:8258-8261, 2007.

[16] W. Xiao, D. Passerone, P. Ruffieux, K. Aït-Mansour, O. Gröning, E. Tosatti, J. S. Siegel, and R. Fasel. *C_{60}/Corannulene on Cu(110): A Surface-Supported Bistable*

Buckybowl-Buckyball Host-Guest System. Journal of the American Chemical Society, 130:4767-4771, 2008.

[17] R. Jaafar, C. A. Pignedoli, G. Bussi, K. Aït-Mansour, O. Groening, T. Amaya, T. Hirao, R. Fasel, and P. Ruffieux. *Bowl Inversion of Surface-Adsorbed Sumanene.* Journal of the American Chemical Society, 130:4767-4771, 2014.

[18] C. J. Hagedorn, M. J. Weiss, and W. H. Weinberg. *Dissociative chemisorption of hydrogen on Ir(111): Evidence for terminal site adsorption.* Physical Review B, 60(20):R14016, 1999.

[19] K. Moritani, M. Okada, M. Nakamura, T. Kasai, and Y. Murata. *Hydrogen-exchange reactions via hot hydrogen atoms produced in the dissociation process of molecular hydrogen on Ir (111).* The Journal of Chemical Physics, 115(21):9947–9959, 2001.

[20] C. Busse, P. Lazić, R. Djemour, J. Coraux, T. Gerber, N. Atodiresei, V. Caciuc, R. Brako, A. T. N'Diaye, S. Blügel, J. Zegenhagen, and T. Michely. *Graphene on Ir(111): physisorption with chemical modulation.* Physical Review Letters, 107(3):036101, 2011.

[21] I. Pletikosić, M. Kralj, P. Pervan, R. Brako, J. Coraux, A. T. N'Diaye, C. Busse, and T. Michely. *Dirac cones and minigaps for graphene on Ir(111).* Physical Review Letters, 102(5):056808, 2009.

[22] G. Henkelman, B. P. Uberuaga, and H. Jónsson. *A climbing image nudged elastic band method for finding saddle points and minimum energy paths.* The Journal of Chemical Physics, 113(22):9901–9904, 2000.

[23] P. Lacovig, M. Pozzo, D. Alfé, P. Vilmercati, A. Baraldi, and S. Lizzit. *Growth of dome-shaped carbon nanoislands on Ir(111): the intermediate between carbidic clusters and quasi-free-standing graphene.* Physical Review Letters, 103(16):166101, 2009.

[24] J. Coraux, A. T. N'Diaye1, M. Engler, C. Busse, D. Wall, N. Buckanie, F.-J M. zu Heringdorf, R. van Gastel, B. Poelsema and T. Michely. *Growth of graphene on Ir(111).* New Journal of Physics, 11(023006):22, 2009.

[25] C. T. Campbell, L. Árnadóttir, and J. R. V. Sellers. *Kinetic prefactors of reactions on solid surfaces.* Zeitschrift für Physikalische Chemie, 227(9-11):1435–1454, 2013.

[26] H. Lesnard, M. L. Bocquet, and N. Lorente. *Dehydrogenation of aromatic molecules under a scanning tunneling microscope: pathways and inelastic spectroscopy simulations.* Journal of the American Chemical Society, 129(14):4298–4305, 2007.

[27] W. Gao, W. T. Zheng, and Q. Jiang. *Dehydrogenation of benzene on Pt(111) surface.* The Journal of Chemical Physics, 129(16):164705, 2008.

[28] I. M. Fernandez, D. Wang, and Y. Zhang. *Direct Growth of Graphene Nanoribbons for Large-Scale Device Fabrication.* Nano Letters, 12:6175-6179, 2012.

[29] H. Zhang, J. Zhao, and Q. Caia. *Pyridine derivative/graphene nanoribbon composites as molecularly tunable heterogeneous electrocatalysts for the oxygen reduction reaction.* Physical Chemistry Chemical Physics, 18:5040-5047, 2016.

Chapter 6

Carbon monoxide interaction with Rh nanoclusters grown on Gr/Ir(111)

Metal or metal-oxide nanoclusters have attracted a great deal of attention in the last two decades due to the increasing interest of the scientific community in field of nanotechnology. The surface of nanoclusters represents an abrupt change in symmetry compared to the bulk materials, leading to reduced atomic coordination and higher chemical reactivity [1]. Surface science methodologies can be applied to get insight on how the electron density of states modifies the inter-atomic interactions, and hence the structural and electronic properties of supported nanoclusters. The surface behaviour of nanocluster–based materials is crucial for understanding the fundamental processes in real world applications, more specifically in heterogeneous catalysis. One of the most striking example of unexpected properties of metal nanoclusters is the high chemical activity reported for small Au nanoclusters [2, 3, 4]. Beside this, other transition metals, such as Pt, in fact, exhibit an enhanced reactivity in their nanocluster form [5, 6].

This high catalytic activity has been often explained in terms of the increased reactivity of corner and edge atoms, which are characterized by a lower coordination number (C_N) with respect to atoms in the bulk or on the clusters nanofacets [7, 8]. The coordination number linearly correlates with adsorption energies of reaction intermediates, and is one of the factors driving the overall catalytic activity [9]. Maximum reaction rates can be obtained when the binding of reaction intermediates to the surface is neither too strong nor too weak, yielding a "Sabatier volcano" (see

Fig. 6.1) named after the French chemist Paul Sabatier. Lowering the coordination

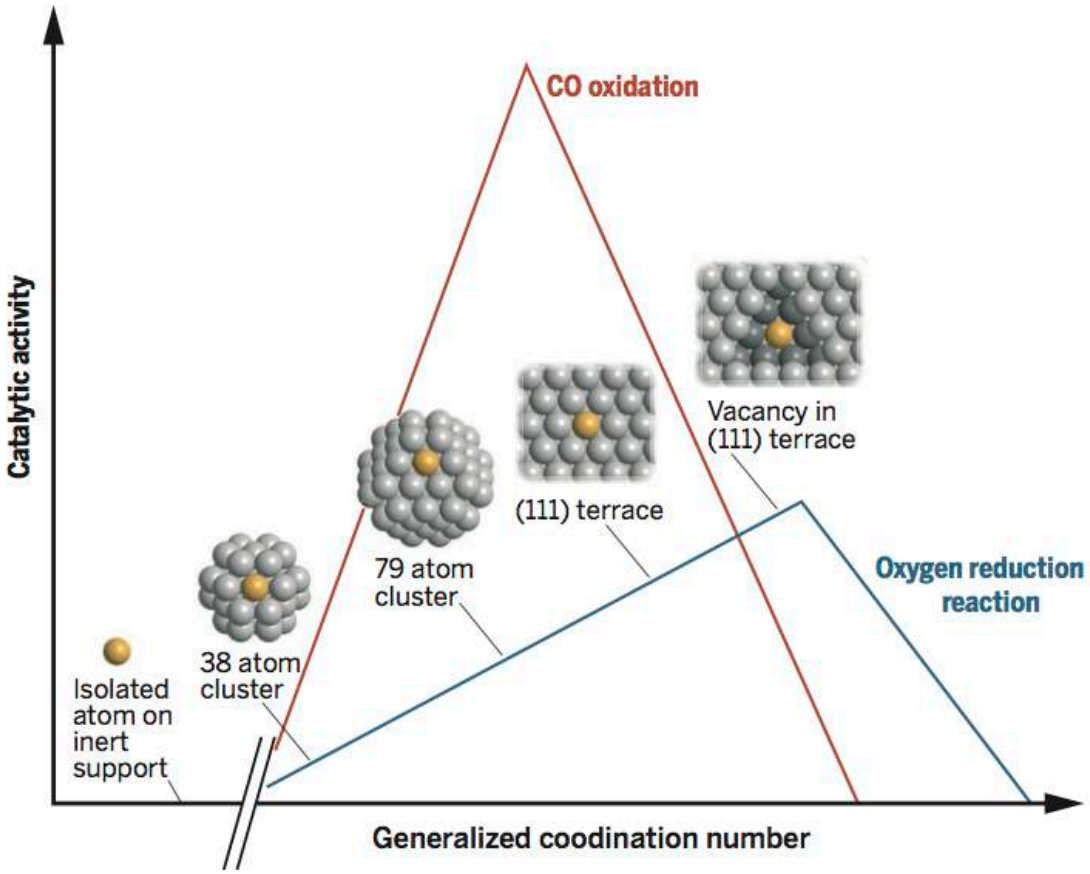

Figure 6.1: Platinum sites with higher coordination numbers (highlighted in gold) turn over oxygen reduction catalysis faster than those with lower coordination numbers. Generalizing this concept to include the coordination of the nearest-neighbor platinum sites, Calle-Vallejo [9] were able to predict that concave sites are three times as active for oxygen electroreduction as is Pt(111). This strategy may be extended to the CO oxidation reaction (red) and the water-gas shift reactions, investigated by Ding [10], who show that platinum nanoparticles rather than site-isolated platinum atoms are responsible for faster rates. Adopted from [16].

number of platinum by increasing the number of steps on single-crystal platinum surfaces leads to an increase in the rates of electrochemical oxygen reduction [11, 12]. On the other hand, increasing the number of steps on platinum surfaces can boost the rates of CO oxidation substantially [13, 14]. This observation has motivated the preparation of CO oxidation catalysts that minimize the coordination number of platinum through the use of small clusters or isolated atoms on oxide supports [15]. The rational design of catalysts for heterogeneous processes requires a detailed understanding of the interplay of both the electronic structure of the catalyst surface

and its local coordination environment [16]. In Au systems, in fact, it has been found that the binding energy of small molecules like O_2, O, and CO, increases with decreasing coordination number C_N [17]. This trend is typically interpreted in terms of the classical d-band model developed in the '90 by Bjork Hammer and Jens Nørskov [18, 19], which relates the chemical properties and reactivity of transition metals to the position of their d-band centre. In atoms with a small coordination number, the d-band width is reduced with respect to the case of bulk atoms, and hence, if the d-band is more than half filled (as in the case of Rh), its centre shifts to higher energies to preserve charge neutrality [18, 19, 20, 21]. As a consequence of this trend, atomic and molecular adsorbates tend to bind more strongly to atoms with a lower coordination.

In this respect, CO dissociation on transition metal vicinal surfaces and supported clusters is particularly important in heterogeneous catalysis being one of the fundamental steps in the Fisher-Tropsch catalytic reaction, where CO and H are converted into hydrocarbons [22, 23]. For example, it has been found that Ru atomic step sites exhibit enhanced CO dissociation activity compared to smooth (001) terrace sites [24]. On Rh, previous results have shown that CO dissociation is negligible on close packed (111), (110), and (100) surfaces [25], and that it increases on stepped (211) [26] and (210) [27] Rh substrates. Even Rh nanostructured surfaces presenting rhomboidal faceted nanopyramids grown on Rh(110), show large efficiency towards CO dissociation, a process which is inhibited on flat (110) terraces [28]. Experiments on Rh clusters supported on alumina surfaces have shown a strong size dependence of the reactivity towards CO dissociation but the nature of the active sites was not explained [29].

The key challenge for the development of cluster–based technologies is identifying a controllable and reproducible strategy to synthesize ordered, large-scale replicas of these building blocks on a suitable substrate [30, 31, 32]. This is achievable through self-assembly to obtain high-density arrays of nanoclusters periodically repeated over the substrate [33].

In this context, the moiré lattice formed by Gr on lattice–mismatched transition metals (like Ir(111)) is an ideal candidate because it has a natural corrugation which enables the growth of clusters which could self-assemble into extended, peri-

odic superstructures by adsorbing at the minimum–energy sites. Gr has been studied in recent years and proved as an excellent candidate for the supported growth of small transition metal nanoclusters and for the formation of long-range-ordered superstructures [34, 35, 36, 37]. The Gr/Ir(111) system discussed in Chapter 3 [38], due to the corrugation of the carbon layer and its very weak interaction with the substrate, is the ideal candidate to grow small Rh nanoclusters which could find application in the field of catalysis.

6.1 Rh nanoclusters supported on Gr/Ir(111)

Rh nanoclusters grown on Gr/Ir(111) have already been thoroughly investigated within our group as part of a research project on Gr–supported transition metal nanoclusters [36]. This study had demonstrated the possibility to finely control the morphology and the degree of structural order of Rh clusters grown on Gr/Ir(111) moiré superlattice. By measured and calculated Rh $3d_{5/2}$ core level BEs we identified non-equivalent edge, facet, and bulk atoms of the nanoclusters. Further, the Rh inter-atomic distance changes occur while varying the nanocluster size, thus leading to a modification of the clusters properties.

Initially, our focus was the characterization of the as-deposited Rh nanoclusters, in order to make a comparison with the previous results obtained by our group and to get a reference set of data for the subsequent carbon monoxide adsorption experiments.

All the experimental results discussed in this chapter were carried out at the SuperESCA beam line of Elettra, using HR-core level photoelectron spectroscopy. The Ir(111) single crystal was used as substrate to grow Gr and its cleaning procedure is the same as described in previous chapters.

Graphene was epitaxially grown on the clean Ir(111) substrate by C_2H_4 CVD, using C_2H_4 pressures between 5×10^{-8} and 3×10^{-7} mbar and then annealing the substrate between 550 to 1450 K. As reported in the previous chapters the C 1s core level spectrum of the Gr/Ir(111) substrate (see Fig. 6.2 (a)) shows a single component found at 284.08 eV as typical of weakly interacting lattice mismatched Gr-metal systems [39] and also we observed in our previous studies [38].

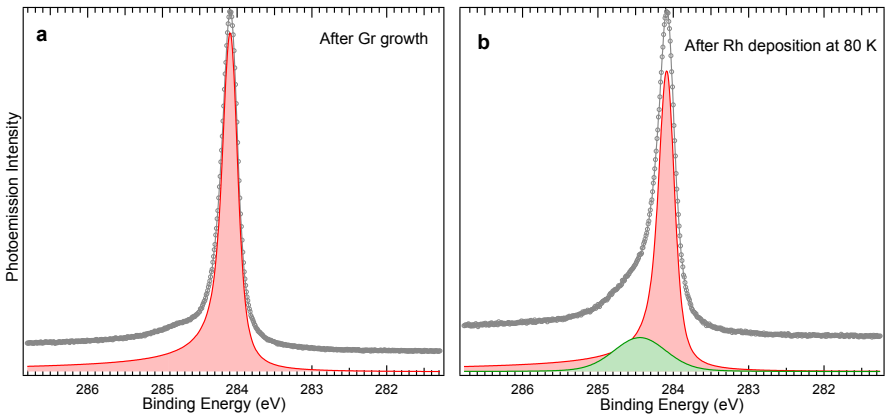

Figure 6.2: High energy resolution C 1s core level spectrum of Gr/Ir(111) acquired at T=80K, at $h\nu$=400 eV in the normal emission configuration, before (a) and after (b) low temperature Rh deposition. The spectrum shows a single component, a hallmark of weakly interacting lattice-mismatched Gr/metal systems.

The Ir $4f_{7/2}$ core level spectra of the substrate before and after Gr growth (see Fig. 6.3 (a) and (b)) shows that the substrate is not appreciably modified by the presence of the C layer.

The Rh nanoclusters were deposited by means of an evaporator (sublimation from a high purity Rh wire) at low temperature (80 K) on Gr/Ir(111) interface. We choose this low temperature to limit surface diffusion of atoms and clusters during deposition.

As highlighted in [36], we can observe slight changes in the C 1s spectrum with the appearance of new component originating specifically on the high BE side of the main peak. This arises from the interaction of the graphene layer with Rh metal atoms, both from the clusters and from the Ir substrate (green component in Fig. 6.2 (b)). This feature is especially evident at the lowest temperature, where the clusters are smaller and regularly distributed on the moiré template. When clusters are small they induce a pinning of the Gr interface layer to the substrate, thus inducing a modification of the core level electronic structure of Gr. As the clusters get bigger upon annealing to higher temperature, their surface density decreases, so that the local pinning mechanism is reduced and the associated spectral component in the C 1s core level spectrum is accordingly reduced.

The thermal evolution of the morphology and surface distribution of Rh nanoclusters have already been addressed in detail by previous study [36] for different

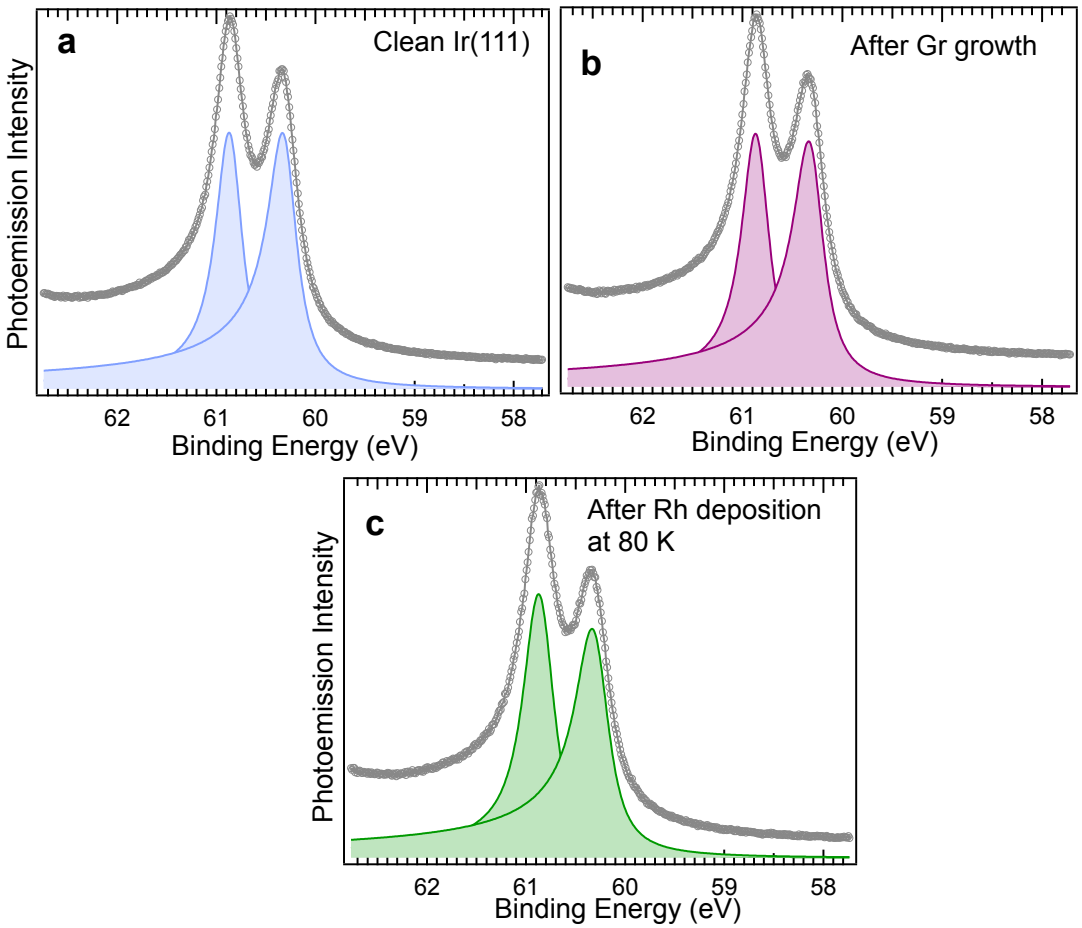

Figure 6.3: High energy resolution Ir $4f_{7/2}$ core level spectra of the clean (a) and Gr–covered substrate Ir(111) substrate before (b) and after (c) Rh evaporation, acquired at T=80 K, at $h\nu$=200 eV in the normal emission configuration. The spectrum does not show appreciable changes upon Gr growth.

initial Rh coverages, using a combination of STM, high energy resolution core level XPS and DFT calculations. A set of STM images of Gr-supported Rh nanoclusters acquired at initial Rh coverages (0.2 and 1 ML) with different annealing temperatures (300 and 840 K) is shown in Fig. 6.4 [36]. The structural analysis showed that, both at low (0.2 ML) and high Rh coverages (up to 1 ML), the as–deposited clusters are regularly spaced, with an occupancy of one moiré cell per cluster. This configuration is pretty stable up to a temperature of ∼300 K.

In oder to understand the cluster behaviour following same approach as used by [36], we annealed the as deposited Rh clusters at 300 K and the high resolution spectra of Rh $3d_{5/2}$ was acquired as shown in Fig. 6.5 (b). The structural disorder

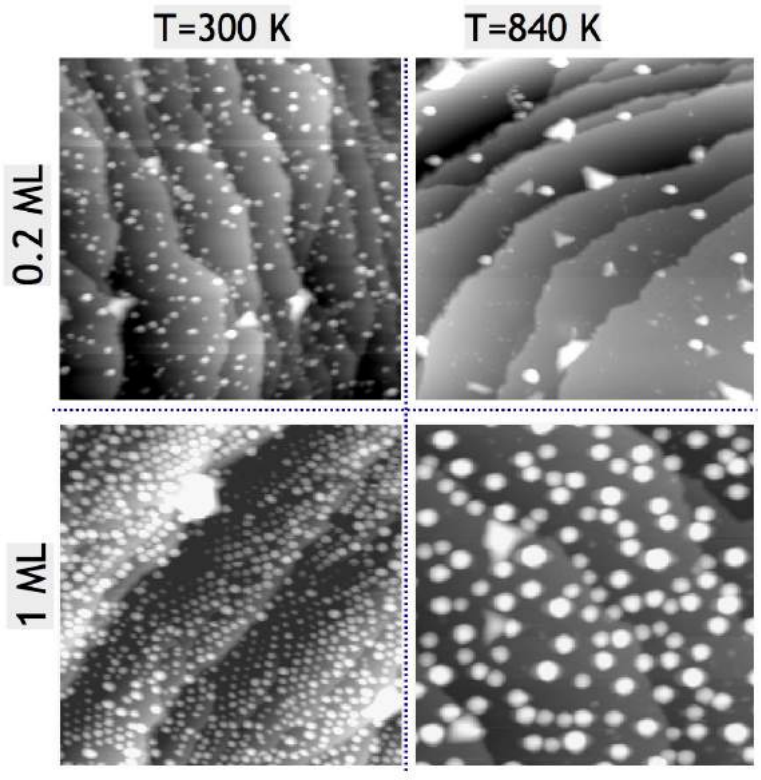

Figure 6.4: STM images (800×800 Å^2) of Rh clusters on Gr/Ir(111), for different Rh coverages and different annealing temperatures. Adopted from [36].

of the cluster atomic configurations is still present at this stage of the annealing and can be appreciated in the large Gaussian broadening of the spectrum. Further, we annealed the Rh clusters up to 840 K. This treatment promotes the coalescence of the particles into larger clusters of a few hundred atoms (with a diameter between 2 and 4 nm, see Fig. 6.4), extending over one or more moiré cells and exhibiting a high degree of crystallinity [36]. The high structural order of the clusters is directly reflected in the shape of the Rh $3d_{5/2}$ core level spectrum after annealing at 840 K (Fig. 6.5 (c)).

We also observe a partial decrease of the Rh $3d_{5/2}$ photoemission signal following the annealing, which has already been reported before [36] and has been interpreted in terms of inelastic mean free path effects because of the 3D character of the nanostructures. The quantitative analysis of the Rh $3d_{5/2}$ photoemission spectra revealed the presence of three core level components, in excellent agreement with the results obtained by Cavallin *et al.* [36] After annealing to high temperature (840 K), both Rh evaporation and intercalation can be safely ruled out, while only at higher

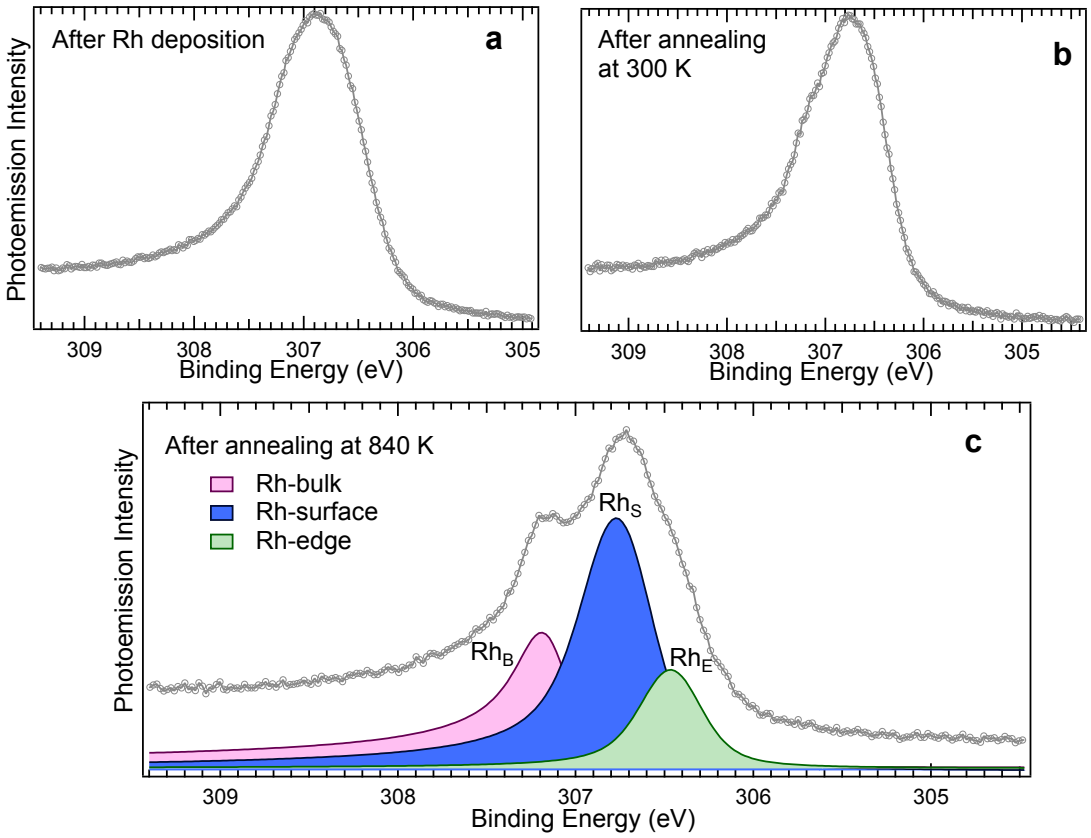

Figure 6.5: High energy resolution Rh $3d_{5/2}$ core level spectra acquired (a) after deposition of 0.4 ML of Rh at 80 K; (b) after annealing at 300 K; (c) after annealing at 840 K. All the photoemission measurements were carried out at $h\nu$= 400 eV at normal emission. The spectral deconvolution into three components, due to differently coordinated Rh atoms (Rh_B, Rh_S, Rh_E), as obtained from our analysis, is shown in panel (c).

temperatures a partial intercalation of the Rh atoms at the Gr/Ir interface can be observed. According to the interpretation suggested by Cavallin [36], we assigned the three components to non-equivalent Rh atoms with a different coordination number (here and in the following indicated as C_N): more specifically, we attributed the component at higher BE (Rh_B, 307.15 eV) to bulk Rh atoms (C_N = 12), the component in the middle, Rh_S, which has a SCLS of -420 meV, to Rh atoms on the nanofacets (C_N = 9 for (111) facets and C_N = 8 for (100) facets) and the component at the lowest BE (Rh_E, at -730 meV with respect to Rh_B) to Rh atoms at the nanoclusters edges (C_N = 7) (Fig. 6.5 (c)). This is in line with the general observation that a lower coordination is associated with a smaller BE of the corresponding Rh $3d_{5/2}$ core level component.

The DFT calculations carried out on Rh nanoclusters with a variable number

of atoms (between 19 and 82) proved that, while smaller clusters present a morphological disordered and lack a clear layered structure, clusters formed by several tens of atoms form regular truncated octahedral structures with a predominance of (111) and (100) nanofacets, as also predicted by the Wulff construction [1] [40]. The DFT calculations reported in [36] also showed that Rh atoms with a high C_N are associated with high BE values, while BEs smaller than 306.4 eV are indicative of under coordinated atoms with $C_N \leq 7$, in good agreement with our experimental findings.

The Rh coverage was estimated by measuring the photoemission intensity of the Rh $3d_{5/2}$ and Ir $4f_{7/2}$ spectra and rescaled it to account for the spin degeneracy and the photoelectron cross section of the respective core level at the experimental photon energy. Initially we considered that all the Rh $3d_{5/2}$ signal as originating from the surface and neglected any possible layered structure of the Rh nanoclusters. The surface signal of the Ir substrate I_0 was quantified using the equation

$$I_{tot} = \sum_{i=0}^{inf} I_0 exp(-x_i/\lambda) \tag{6.1}$$

where x_i is the thickness, i is the atomic layer index and I_{tot} is the measured Ir $4f_{7/2}$ total photoemission intensity. The screening effect of the Gr layer was introduced by rescaling factor given by the integral of the attenuation function exp $(-x/\lambda)$ over the thickness of a Gr monolayer and λ is the inelastic electron mean free path.

6.2 Carbon monoxide adsorption

The CO chemisorption on Rh single crystals has been widely investigated in literature particularly core level photoemission studies have been carried out, for the Rh(111) [41, 42, 43] and Rh(100) [44, 45] surfaces, where CO adsorbs non–dissociatively and results in the formation of well ordered over layer structure. Since the Rh clusters supported on graphene mainly exhibits (111)- and (100)-terminated nanofacets, it is informative to compare our findings with the results reported in literature for the corresponding single crystal surfaces.

[1] The Wulff construction returns the crystal shape that minimizes the free energy G at constant volume and yields a constant ratio between the surface energy and the distance of the corresponding basal plane from the centre of the cluster.

CO adsorption on Rh(111) forms at low temperature different ordered surface phases with increasing CO concentration. At 0.25 ML a (2×2)-1CO develops which is followed by $(\sqrt{3} \times \sqrt{3})R30°$-1CO phase at 0.33 ML. At around 0.5 ML a (4×4)-4CO phase is produced which, upon increasing CO coverage, transforms through a split (2×2) phase into a (2×2)-3CO structure at CO saturation (0.75 ML). The spectroscopic analysis [41, 42] revealed that CO molecules occupy two different sites: at coverages up to 0.5 ML most of the molecules are found to adsorb in on-top sites, whereas at higher coverages three-fold hollow sites become increasingly populated. The low temperature CO adsorption on Rh(100) results in formation of c(2×2) and $(4\sqrt{2} \times 4\sqrt{2})R45°$ ordered structures associated with the adsorption of CO molecules in on-top (low coverage) and bridge site adsorption (up to 0.75 ML).

The C 1s core level spectrum is a powerful source of information on the evolution of the adsorption sites occupation at each specific coverage. As discussed above, for Rh(111) and Rh(100), the CO adsorption is energetically more favourable on-top sites at low coverages, leading to the appearance of a single component at 286.06 eV and 285.85 eV on Rh(111) [41, 42] and Rh(100) [45], respectively. With the increase in CO coverage, this component shifts by about 100 meV towards smaller BEs. This is associated with different adsorption configurations: on Rh(111) a component due to CO molecules adsorbed at threefold sites appears at 285.38 eV, while on Rh(100) CO adsorption in bridge sites results in the appearance of a peak at 285.45 eV. In order to study the adsorption of CO on the Gr-supported clusters, in the first part of our study we exposed the clean clusters to an increasing CO pressure, between 1×10^{-9} mbar and 1×10^{-8} mbar, at 80 K, while monitoring in parallel the evolution of the C 1s and Rh $3d_{7/2}$ core level.

In our case, we also found a single component at 286 eV during the initial stage of CO exposure, the value is similar to the ones found for CO adsorption on top site (see Fig. 6.6). At higher coverages above 0.3 ML, another component start appearing at 285.46 eV, which can be attributed to a different CO phase. It is well known from the previous studies about CO adsorption on Rh(111) [41, 42] and Rh(100) [45] revealed that this second component is either bridge bonded CO on Rh(100) (285.45 eV) and for threefold–bonded CO on Rh(111) (285.38 eV). Considering the very similar C 1s BEs found for CO occupation in these adsorption sites it is very

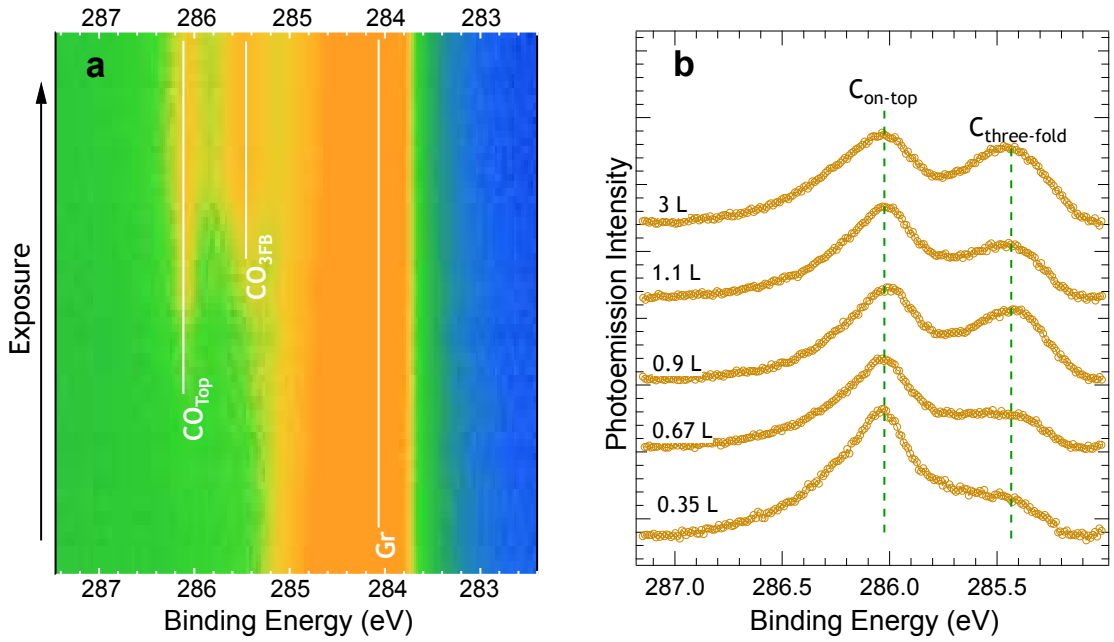

Figure 6.6: (a) 2D waterfall plot showing the evolution of the C 1s core level spectrum ($h\nu$=400 eV) during CO exposure at 80 K; (b) High energy resolution C 1s core level spectra acquired after dosing CO on the Rh nanoclusters up to selected exposures.

difficult to make at this stage an assignment. We will therefore assign this adsorption site based on the DFT results, which will be discussed later in this Chapter.

It is also very important to understand whether the spectral component due to Gr under goes any changes upon CO adsorption. The large single C 1s peak at 284.04 eV (see Fig. 6.6 (a)) is largely unaffected by CO adsorption on the supported Rh nanoclusters. This implies that CO does not bind to Gr at the temperature we used in this experiment, so that the whole measured C 1s signal due to CO originates exclusively from CO adsorbed on the Rh nanoclusters.

In oder to gain a deeper understanding of the CO adsorption behaviour on Rh nanoclusters, we analysed the Rh $3d_{5/2}$ spectra acquired while dosing CO at T= 80 K (see Fig. 6.7). The interpretation of the data is not as straightforward as in the case of Rh single crystal surfaces and this is attributed to the higher degree of structural complexity in nanoclusters.

For flat, low Miller index surfaces such as Rh(111) and Rh(100), the CO adsorption causes a suppression of the photoemission signal of the first layer clean surface atoms (*i.e.* Rh atoms that are not coordinated to adsorbates), followed by the

appearance of new CO–induced surface core level shifted component arises due to the CO molecule coordinated to more than one Rh atoms. This results in a shift to higher binding energy (because of corresponding d-band broadening) with respect to the clean surface components. We observe SCLSs of +270 and about +50 meV for the (111) and (100) surfaces for CO adsorption in on-top sites, resulting in a shift from the 'clean surface' component of +770 and +650 meV, respectively [41, 42, 45]. The SCLS induced by CO in bridge sites on Rh(100) is -300 meV (+350 meV relative to the clean surface component), while the SCLS associated with threefold coordinated CO on the Rh(111) surface is -220 meV (+280 meV relative to the clean surface). The higher the CO coordination, the lower is the CO-induced shift of the affected substrate atoms [41, 42, 45].

The situation is more complex with CO adsorption on Rh nanoclusters, however it is possible to identify some semi-quantitative trends and relate them with what is known in literature for Rh(100) and Rh(111). Figure 6.7 (a) shows the

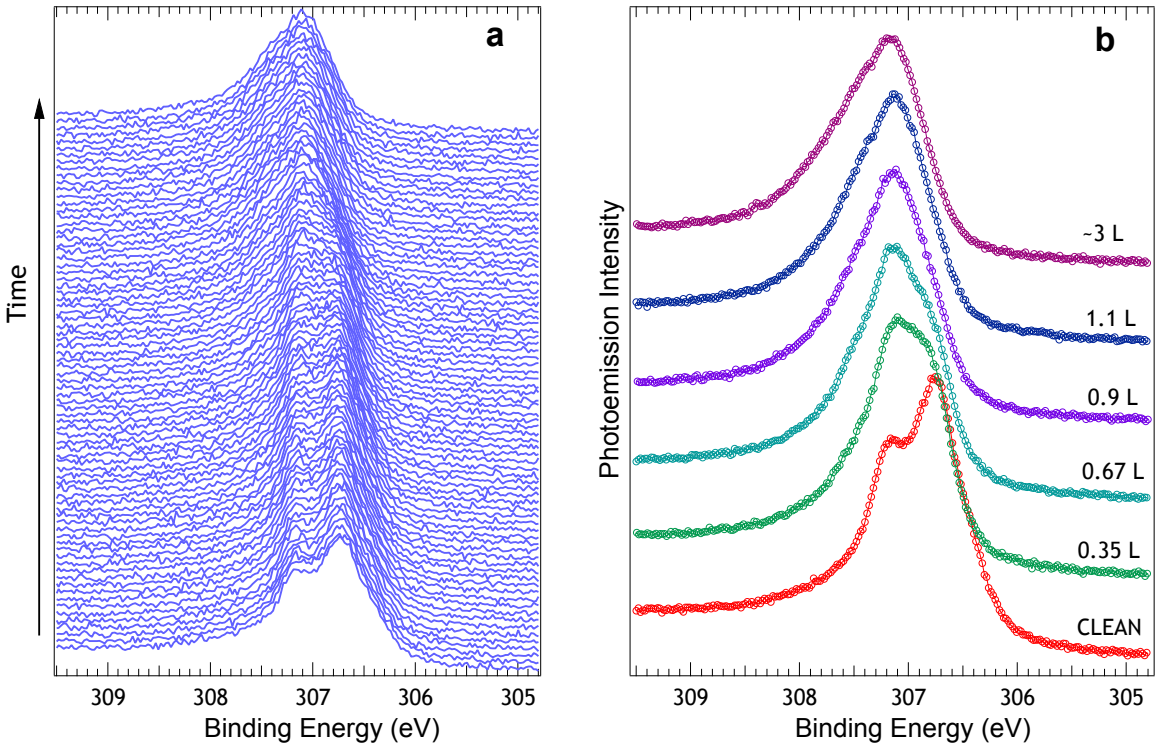

Figure 6.7: (a) Time lapsed series of Rh $3d_{5/2}$ core level spectra acquired at $h\nu$=400 eV during CO exposure at 80 K; (b) High energy resolution Rh $3d_{5/2}$ core level spectra acquired after dosing CO on the Rh nanoclusters up to selected exposures.

evolution of the Rh $3d_{5/2}$ core level during CO exposure. The most interesting result

is that the early stage of CO adsorption is accompanied by the disappearance of the core level component, Rh_E, due to Rh atoms at the cluster edges. This results in an increased spectral intensity between the bulk and surface component. While in the case of CO adsorption on Rh single crystals [41, 42, 45], the decrease of the Rh $3d_{5/2}$ clean surface component is accompanied by the appearance of a single new component associated with CO adsorption in on-top sites, in the case of the Rh clusters we observe a more complicated trend. In fact, along with the core level component at +320 meV with respect to the bulk, we also observe the appearance of a new peak with a surface core level shift of -200 meV. A satisfactory description of the Rh $3d_{5/2}$ spectrum can be obtained using only two additional CO-induced surface components (Rh_{S1} and Rh_{S2}, as shown in Fig. 6.7) up to the saturation exposure. For

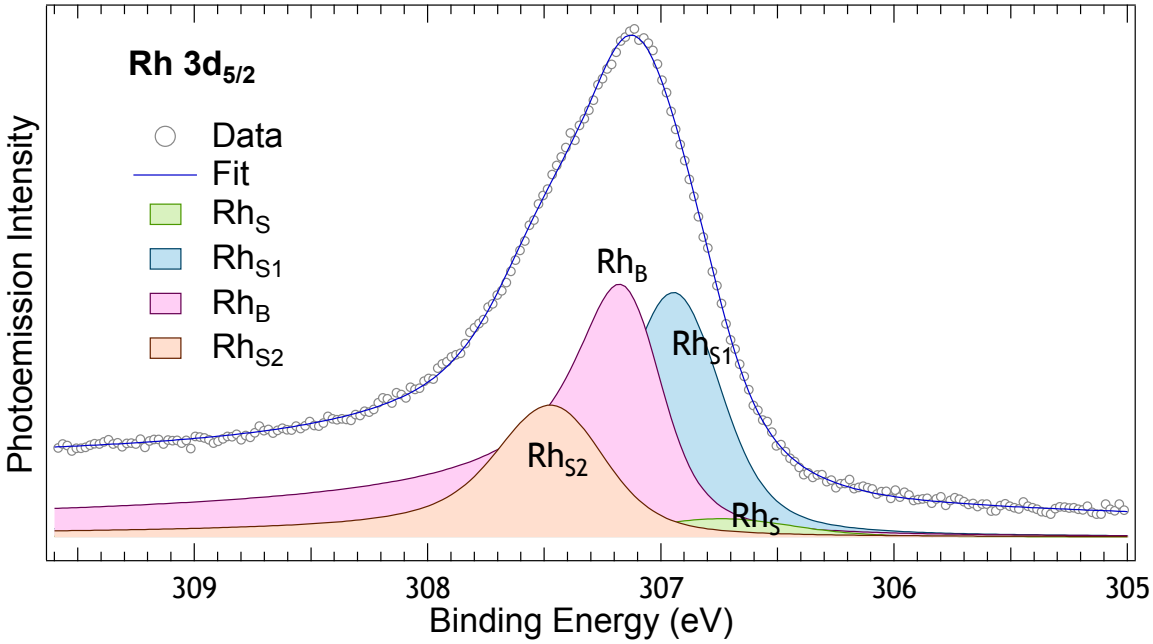

Figure 6.8: High energy resolution Rh $3d_{5/2}$ core level spectrum following CO exposure at 80 K at $h\nu$= 400 eV. The deconvolution into the individual spectral components is shown superimposed.

these new surface components we used the same Lorentzian and asymmetry line shape parameters as the one used for the Rh_S component except for the Gaussian width. This was done in order to reduce the number of fitting parameters for the clean surface peak (Rh_S). The evolution of the photoemission intensities of the different Rh $3d_{5/2}$ core level components during the CO uptake experiment is reported in Fig. 6.8. While the component at Rh_{S1} can be assigned to CO adsorption in on-top

sites, based on the similar SCLS found for the corresponding component on Rh(111) and Rh (100), the attribution of Rh_{S2} is less straightforward, also because this peak could overshadow the presence of a manifold of unresolved components in the BE region between the bulk and the surface Rh_S peak. The most interesting results of our uptake experiments is however the observation of a large decrease of the Rh_E components in the initial stage of the uptake, well before the decreased of the Rh_S peak.

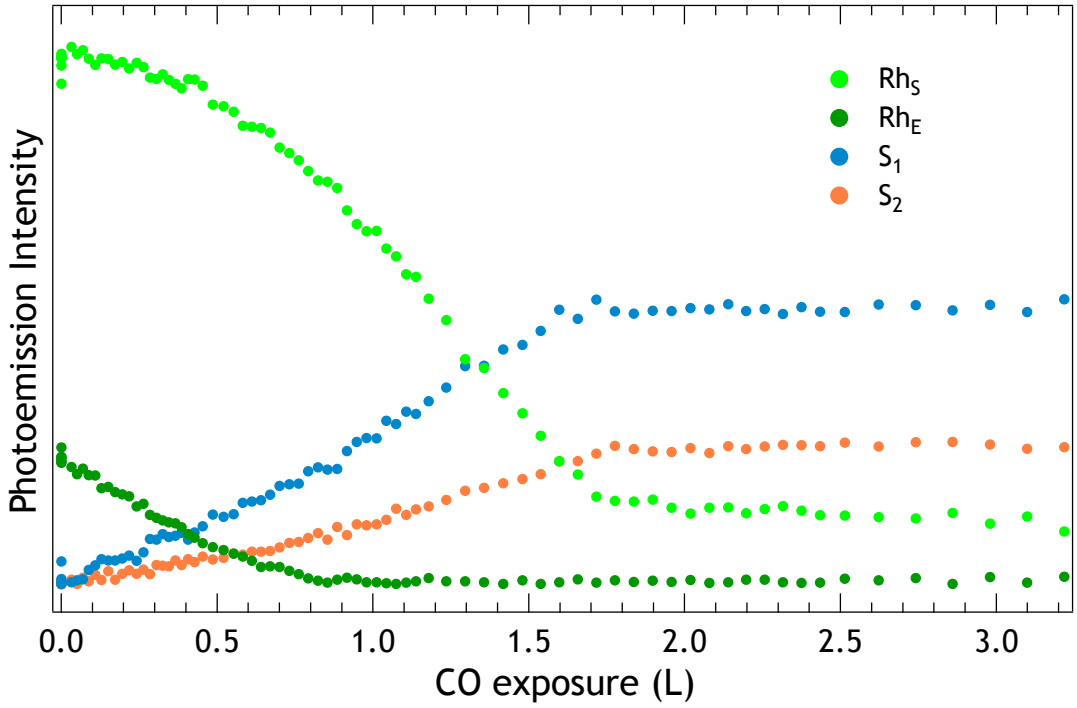

Figure 6.9: Photoemission intensity evolution of the different Rh $3d_{5/2}$ core level components during CO exposure at 80 K. To reduce fitting artifacts, the intensity of the bulk component, Rh_B , was held fixed to a constant value during the whole exposure.

In order to clarify these issues and to get an atomistic insight into the mechanisms of CO adsorption on the Rh nanoclusters and on the origin of different core level component, a series of DFT calculations were carried out by the theoretical group led by Prof. Dario Alfè at the UCL-London, UK.

Carbon monoxide is a simple diatomic molecule, but despite its simplicity it shows a rich phase diagram on metal surfaces [46, 47]. In light of this, it is important to underline that state of the art density functional calculations still fail to accurately describe few aspects of the adsorption of CO on metal surfaces. For

the Cu, Rh and Pt(111) surfaces, the generalized gradient approximation (GGA) in the Perdew–Burke–Ernzerhof (PBE) version predicts that CO adsorbs at a high coordination site (typically the hollow site) [48], whereas experiments unequivocally show that atop adsorption is preferred [49, 50]. Equally compelling is that adsorption energies are significantly overestimated using the PBE functional [49, 50]. These discrepancies were first noted in a classical paper by Feibelman [49]. Since then there has been emerging evidence that the present local and semi-local functionals are not capable of correctly describing the subtle balance between donation of charge to the substrate and back donation to the molecule for many adsorption problems [51]. The common model used to describe CO adsorption is the Blyholder model [52], which invokes interactions of the two CO frontier orbitals, the 5σ HOMO (highest occupied molecular orbital) and the $2\pi^*$ LUMO (lowest unoccupied molecular orbital), with the metal states. Due to the interaction with the metal states, bonding 5σ–metal orbitals and antibonding 5σ–metal orbitals develop, and the latter are partly shifted above the Fermi level of the metal, causing a net bonding interaction (donation). Likewise, bonding $2\pi^*$–metal hybrid states become populated (back-donation). Simple symmetry tells us that the highly directional 5σ–metal interaction is particularly strong for atop adsorption, whereas the $2\pi^*$ interaction dominates for hollow site adsorption [47, 53, 54, 55].

Clearly, however, none of the functionals can predict the surface energies and the adsorption energies well at the same time [51]. From their point of view, the main error of semi-local functionals is in the description of the strength of the back-donation to the $2\pi^*$ orbital, which tends to be overestimated using any of the semi-local density functionals. Hybrid functionals improve on that aspect, but unfortunately simultaneously increase the d bandwidth and concomitantly the overall adsorption energies while rPBE and BLYP underestimate binding in solids and surface energies, but describe adsorption energies well [51].

In this scenario, there is no single perfect functional which can describe well the CO-adsorption energies on Rh nanoclusters. We initially used PBE functional to probe adsoprtion energies for CO molecule in 17 different configurations as shown in Fig. 6.10. Adsorption sites have been chosen in such a way to have on-top (a-f-g), bridge (f-m) and three-fold (o-q) sites occupied on flat and tilted nanofactes (both

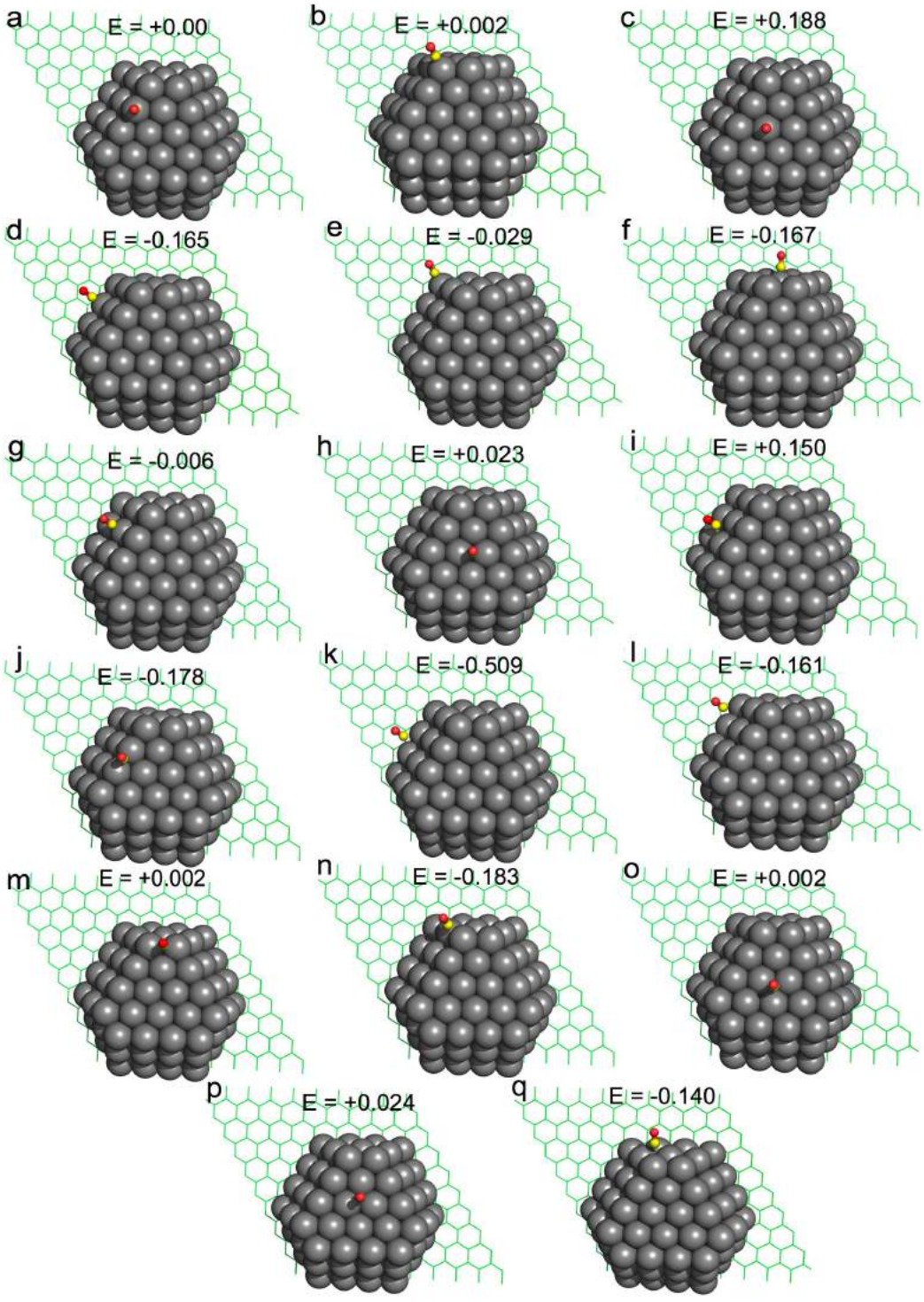

Figure 6.10: Illustration of CO (Gr in green, Rh nanoclusters in gray and CO molecule is in red and yellow color) adsorption on Rh nanoclusters (with n=82 Rh atoms) (a) to (q) present different adsorption sites.

(100) and (111)), on the lateral edges of the nanoclusters and on the basal edges. Positive values of the calculated adsorption energies indicate that the configuration

is unstable. This is the case in particular for the upper part of the nanocluster ((111) nanofacet) in on-top (c), bridge (h), three-fold HCP and FCC sites (o and p). This is also the case for CO in brdige site on the (100) lateral nanofacets (i). The most

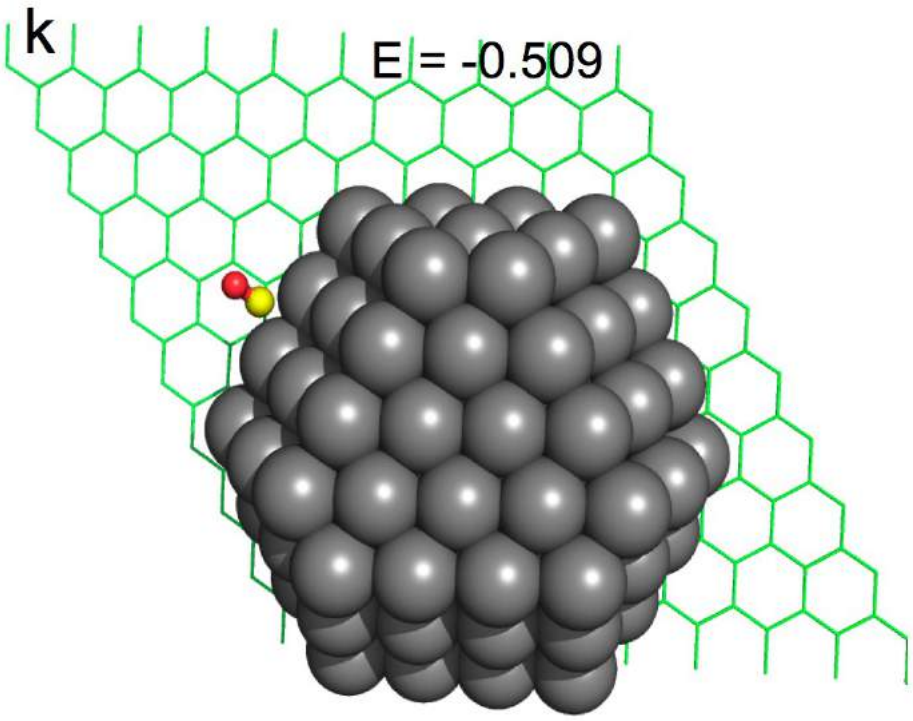

Figure 6.11: The most suitable CO adsorption configuration is bridge on the edge of the Rh nanoclusters (k).

preferred adsorption site is close to the basal plane of the cluster, namely the bridge (k), as shown in Fig. 6.11. Other sites with comparable energies are on-top ((d) and (f)), and the bridge ((j), (l) and (n)). The calculations performed using the PBE functional have been extended to selected configuration by using the PBE0 functional, that it is know to give better accuracy. It is extremely interesting to observe that the new calculations show an increase adsorption energies of all the CO configurations where the molecules is adsorbed on under-coordinated Rh atoms, while the stability on flat nanofacets has diminishes. This can be appreciated by comparing the energies in Table 6.1. CO in bridge site on the basal edge of the nanocluster (k) is still the preferred configuration, but the energy gain with respect to the top site on the cluster region is strongly reduced (energy difference change from 344 meV to 133 meV). The stability of CO molecules on the flat nanofacets instead has decreased: for example in the case of CO molecules in the (111) upper cluster nanofacet is reduced by more

CO adsorption sites	**PBE**	**PBE0**
c	+0.188 eV	+0.478 eV
d	-0.165 eV	-0.302 eV
f	-0.167 eV	-0.071 eV
h	+0.023 eV	+0.467 eV
i	+0.150 eV	+0.271 eV
k	-0.509 eV	-0.439 eV
n	-0.183 eV	-0.253 eV
o	+0.002 eV	+0.025 eV

Table 6.1: Comparison of CO adsorption energies in different adsorption sites on Rh nanoclusters on Gr/Ir(111) calculated using two different functionals.

than 400 meV.

CO adsorption sites	**C 1s core levels**
d	0
f	+232 meV
h	-420 meV
k	-500 meV

Table 6.2: Theoretically calculated C 1s core level shifts for CO configuration in different adsorption sites.

We remain still with the problem of the discrepancy between experimental and theoretical preferred adsorption configuration. In order to try to solve the issue we have calculated the C 1s core electron binding energy for each of the CO configurations reported in Table 6.2. The results of the core level shifts are calculated with respect to the C 1s binding energy of CO in top sites on the basal edge of the clusters (configuration d). CO molecules in on-top site in configuration f (tilted (111) nanofacets) present a core level shift of +232 meV, while the CO in bridge site on the upper face (h) and in the preferred adsorption site (k) are expected to show a shift of -420 and -500 meV, respectively. However, experimentally we determine that the

component at high BE 286 eV is attributed to the on-top adsorption site and the low BE component at 285.46 eV (see Fig. 6.6) is associated to the bridge configuration in the basal plane edges of the facet. The asymmetry in the on-top peak to the higher BE can be explained in term of final state vibrational excitation of the on-top adsorption site in the nanofacets or to occupation of different on-top configurations.

The more negative value of adsorption energy (see Table 6.1) means more preferable CO adsorption site on Rh nanoclusters. We have found that the best adsorption site is CO in on-top at low coverages (see Fig. 6.6) even though the DFT says that it is different. After the initial CO adsorption in on-top sites we observe that later CO sits on the edges of the Rh nanoclusters as it is clear from the Fig. 6.6 with higher exposure. This can be explained with the Rh $3d_{5/2}$ uptake, see Fig. 6.9, where Rh_E is consumed quickly even that the Rh_S is still present. From our DFT calculations we found that the most preferable site for CO adsorption is bridge on the edge of the Rh nanoclusters as reported in Fig. 6.11 and we also observe experimentally that the edge absorption sites (Rh_E), as shown in Fig. 6.9, were occupied very quickly. The wrong attribution of the preferred adsorption site in DFT can still be explain as due to the difficulty of ab initio theories to correctly describe the adsorption configurations of CO on transition metal surfaces, as discussed above.

We have demonstrated in previous studies [36] how to control the morphology of Rh nanoclusters which determines the density of edge and facet atoms. By using a combined experimental and theoretical approach now we have shown that the natural corrugation of Gr grown on Ir(111) enables the deposited clusters to arrange themselves into extended, periodic superstructures by adsorbing at the minimum–energy sites where the edges of Rh nanoclusters are the places where the adsorption of CO is preferred. Further this data confirm the previous finding on a variety of transition metal surfaces, where under coordinated atoms have displayed an important role in driving the chemical reactivity of supported nanoclusters. This study can be extended to the other metals to design new Gr-based materials which may help to improve fundamental properties at nanoscale for their application in field of catalysis.

Bibliography

[1] A. Zangwill. *Physics at Surfaces.* Cambridge University Press, Cambridge, 1988.

[2] M. Valden, X. Lai, and D. W. Goodman. *Onset of catalytic activity of gold clusters on titania with the appearance of nonmetallic properties.* Science, 281:1647, 1998.

[3] C. T. Campbell. *The active site in nanoparticle gold catalysis.* Science, 306:234, 2004.

[4] B. Hvolbæk, T. V. W. Janssens, B. S. Clausen, H. Falsig, C. H. Christensen, and J. K. Nørskov. *Catalytic activity of Au nanoparticles.* Nano Today, 2:14, 2007.

[5] N. Tian, Z. Zhou, S. Sun, Y. Ding, and Z. L. Wang. *Synthesis of tetrahexahedral platinum nanocrystals with high-index facets and high electro-oxidation activity.* Science, 316:732, 2007.

[6] S. Vajda, M. J. Pellin, J. P. Greeley, C. L. Marshall, L. A. Curtiss, G. A. Ballentine, J. W. Elam, S. Catillon-Mucherie, P. C. Redfern, F. Mehmood, and P. Zapol. *Subnanometre platinum clusters as highly active and selective catalysts for the oxidative dehydrogenation of propane.* Nature Materials, 8:213, 2009.

[7] P. Gambardella, S. Rusponi, M. Veronese, S. S. Dhesi, C. Grazioli, A. Dallmeyer, I. Cabria, R. Zeller, P.H. Dederichs, K. Kern, C. Carbone, and H. Brune. *Giant magnetic anisotropy of single cobalt atoms and nanoparticles.* Science, 300:1130, 2003.

[8] S. Rusponi, T. Cren, N. Weiss, M. Epple, P. Buluschek, L. Claude, and H. Brune. *The remarkable difference between surface and step atoms in the magnetic anisotropy of two-dimensional nanostructures.* Nature Materials, 2:546, 2003.

[9] F. C.-Vallejo, J. Tymoczko, V. Colic, Q. H. Vu, M. D. Pohl, K. Morgenstern, D. Loffreda, P. Sautet, W. Schuhmann, and A. S. Bandarenka. *Finding optimal surface*

sites on heterogeneous catalysts by counting nearest neighbor. Science, 350(6267):185-189, 2015.

[10] K. Ding, A. Gulec, A. M. Johnson, N. M. Schweitzer, G. D. Stucky, L. D. Marks, and P. C. Stair. *Identification of active sites in CO oxidation and water-gas shift over supported Pt catalysts.* Science, 350(6267):189-191, 2015.

[11] A. Kuzume, E. Herrero, and J. M. Feliu. *Oxygen reduction on stepped platinum surfaces in acidic media.* Journal of Electroanalytical Chemistry, 599:5333-343, 2007.

[12] A. S. Bandarenka, H. A. Hansen, J. Rossmeislc, and I. E. L. Stephens. *Elucidating the activity of stepped Pt single crystals for oxygen reduction.* Physical Chemistry Chemical Physics, 16:13625-13629, 2014.

[13] S. W. Lee, S. Chen, W. Sheng, N. Yabuuchi, Y.-T. Kim, T. Mitani, E. Vescovo, and Y. S.-Horn. *Roles of Surface Steps on Pt Nanoparticles in Electro-oxidation of Carbon Monoxide and Methanol.* Journal of American Chemical Society, 131(43):15669-15677, 2009.

[14] S. C. S. Lai, N. P. Lebedeva, and T. H. M. Koper. *Mechanisms of carbon monoxide and methanol oxidation at single-crystal electrodes.* Topics in catalysis, 46:320-333, 2007.

[15] Q. Fu, H. Saltsburg, and M. F.-Stephanopoulos. *Active nonmetallic Au and Pt species on ceria-based water-gas shift catalysts.* Science, 15(301):935-938, 2003.

[16] I. E. L. Stephens, J. S. Elias, and Y. S.-Horn. *Controlling the coordination of platinum boosts catalytic reaction rates.* Science, 350(6257):164, 2015.

[17] L. Bianchettin. *Electronic structure and chemical reactivity at solid surfaces: the role of under-coordinated atoms and bimetallic alloys.* PhD thesis, University of Trieste, 2008.

[18] B. Hammer, and J. K. Nørskov. *Theoretical surface science and cataly- siscalculations and concepts.* In B.C. Gates and H. Knozinger, editors, Impact of Surface Science on Catalysis, volume 45, page 71. Academic Press, 2000.

[19] J. K. Nørskov. *Why gold is the noblest of all the metals.* Nature, 376:238, 1995.

[20] T. Bligaard, and J. K. Nørskov. Chapter 4 -heterogeneous catalysis. A. Nilsson, L.G.M. Pettersson, and J.K. Nørskov, editors, *Chemical Bonding at Surfaces and Interfaces.* pages 255 – 321. Elsevier, 2008.

[21] J. K. Nørskov, F. Abild-Pedersen, F. Studt, and T. Bligaard. *Density functional theory in surface chemistry and catalysis.* Proceedings of National Academy of Science, 108:937, 2011.

[22] Y. Zhang, G. Jacobs, D. E. Sparks, M. E. Dry, and B. H. Davis. *CO and CO_2 hydrogenation study on supported cobalt Fischer-Tropsch synthesis catalysts.* Catalysis Today, 71:411, 2002.

[23] G. A. Somorjai. *Introduction to Surface Chemistry and Catalysis.* Wiley, New York, 1994.

[24] T. Zubkov, G.A. Morgan, Jr., and J. T. Yates, Jr. *Spectroscopic detection of CO dissociation on defect sites on Ru(109): implications for Fischer-Tropsch catalytic chemistry.* Chemical Physics Letters, 362:181, 2002.

[25] J. C. Campuzano and edited by D. A. King and D. P. Woodruff. *The Chemical Physics of Solid Surfaces and Heterogeneous Catalysis.* Elsevier, New York, 3:389, 1990.

[26] M. Mavrikakis, M. Baumer, H.-J. Freund, and J. K. Nørskov. *Structure sensitivity of CO dissociation on Rh surfaces.* Catalysis Letters, 81:153, 2002.

[27] M. Rebholz, R. Prins, and N. Kruse. *Adsorption and dissociation of CO on Rh (210).* Surface Science, 259:L797, 1991.

[28] F. B. de Mongeot, A. Toma, A. Molle, S. Lizzit, L. Petaccia, and A. Baraldi. *Carbon Monoxide Dissociation on Rh Nanopyramids.* Physical Review Letters, 97:056103, 2006.

[29] M. Frank, S. Andersson, J. Libuda, S. Stempel, A. Sandell, B. Brena, A. Giertz, P. A. Brühwiler, M. Bäiumer, N. Mårtensson, H.-J. Freund. *CO dissociation characteristics on size-distributed rhodium islands on alumina model substrates.* Chemical Physics Letters, 279:92-99, 1997.

[30] C. R. Henry. *Morphology of supported nanoparticles.* Progress in Surface Science, 80:92, 2005.

[31] C. Binns. *Nanoclusters deposited on surfaces.* Surface Science Reports, 44:1, 2001.

[32] T. Wen, and S.A. Majetich. *Ultra-large-area self-assembled monolayers of nanoparticles.* ACS Nano, 5:8868, 2011.

[33] J.V. Barth, G. Costantini, and K. Kern. *Engineering atomic and molecular nanostructures at surfaces.* Nature, 437:671, 2001.

[34] A. T. N'Diaye, S. Bleikamp, P. J. Feibelman, and T. Michely. *Two-dimensional Ir cluster lattice on a graphene moiré on Ir(111).* Physical Review Letters, 97:215501, 2006.

[35] A.T. N'Diaye, T. Gerber, C. Busse, J. Mysliveček, J. Coraux, and T. Michely. *A versatile fabrication method for cluster superlattices.* New Journal of Physics, 11:103045, 2009.

[36] A. Cavallin, M. Pozzo, C. Africh, A. Baraldi, E. Vesselli, C. Dri, G. Comelli, R. Larciprete, P. Lacovig, S. Lizzit, and D. Alfè. *Local electronic structure and density of edge and facet atoms at Rh nano-clusters self-assembled on a graphene template.* ACS Nano, 6:3034, 2012.

[37] P. Yi, M. Gao, L. Huang, F. Liu, and H. J. Gao. *Directed self-assembly of monodispersed platinum nanoclusters on graphene moiré template.* Applied Physics Letters, 95:093106, 2009.

[38] F. Presel, N. Jabeen, M. Pozzo, D. Curcio, L. Omiciuolo, P. Lacovig, S. Lizzit, D. Alfé, and A. Baraldi.*Unravelling the roles of surface chemical composition and geometry for the graphene–metal interaction through C1s core-level spectroscopy.* Carbon, 93:187–198, 2015.

[39] A. B. Preobrajenski, M. L. Ng, A. S. Vinogradov, and N. Mårtensson. *Controlling graphene corrugation on lattice-mismatched substrates.* Physical Review B, 78:073401, 2008.

[40] G. Wulff. Zur Frage der Geschwindigkeit des Wachsthums und der Auflosung der Krystallflachen. Zeitschrift für Krystallographie und Mineralogie, 34:449, 1901.

[41] A. Beutler, E. Lundgren, R. Nyholm, J. N. Andersen, B. Setlik, and D. Heskett. *On the adsorption sites for CO on the Rh(111) single crystal surface.* Surface Science, 371:381, 1997.

[42] A. Beutler, E. Lundgren, R. Nyholm, J. N. Andersen, B.J. Setlik, and D. Heskett. *Coverage- and temperature-dependent site occupancy of carbon monoxide on Rh(111) studied by high-resolution core-level photoemission.* Surface Science, 396:117, 1998.

[43] M. Smedh, A. Beutler, M. Borg, R. Nyholm, and J. N. Andersen. *Determination of the coverage dependent isosteric heat of adsorption of CO on Rh(111) by high resolution core level photoemission.* Surface Science, 491:115, 2001.

[44] A. Baraldi, L. Gregoratti, G. Comelli, V. R. Dhanak, M. Kiskinova, and R. Rosei. *CO adsorption and CO oxidation on Rh(100).* Applied Surface Science, 99:1, 1996.

[45] F. Strisland, A. Ramstad, T. Ramsvik, and A. Borg. *CO adsorption on the Rh(100) surface studied by high resolution photoelectron spectroscopy.* Surface Science, 415:L1020, 1998.

[46] G. A. Somorjai. *Modern Surface Science and Surface Technologies: An Introduction.* Chemical Reviews, 20;96(4):1223-1236, 1996.

[47] R. A. van Santen. *Molecular Heterogeneous Catalysis: A Conceptual and Computational Approach.* (Weinheim: Wiley-VCH), 2005.

[48] B. Hammer, L. B. Hansen, and J. K. Nørskov. *Improved adsorption energetics within density-functional theory using revised Perdew-Burke-Ernzerhof functionals.* Physical Review B, 59:7413 ,1999.

[49] P. J. Feibelman, B. Hammer, J. K. Nørskov, F. Wagner, M. Scheffler, R. Stumpf, R. Watwe, and J. Dumesic. *The CO/Pt(111) Puzzle.* Journal of Physical Chemistry B, 105(18):4018–4025, 2001.

[50] M. Gajdoš, A. Eichler, and J. Häfner. *CO adsorption on close-packed transition and noble metal surfaces: trends from ab initio calculations.* Journal of Physics: Condense Matter, 16:1141, 2004.

[51] A Stroppa, and G Kresse. *The shortcomings of semi-local and hybrid functionals: what we can learn from surface science studies.* New Journal of Physics, 10:063020, 2008.

[52] G. Blyholder. *Molecular Orbital View of Chemisorbed Carbon Monoxide.* Journal of Physical Chemistry, 68(10): 2772–2777, 1964.

[53] R. A. van Santen. *Symmetry rules in chemisorption.* Journal of Molecular Structure, 173:157-172, 1988.

[54] G. Kresse, A. Gil, and P. Sautet. *Significance of single-electron energies for the description of CO on Pt(111).* Physical Review B, 68:073401, 2003.

[55] S. E. Mason, I. Grinberg, and A. M. Rappe. *First-principles extrapolation method for accurate CO adsorption energies on metal surfaces.* Physical Review B, 69:161401, 2004.

Summary and outlook

We can conclude based on ample evidences from (both theoretical and experimental results) that the most suitable substrate giving us almost free standing Gr, is Gr/Ir(111) interface, to study the properties of metal or metal oxide clusters. Using this Gr/Ir(111) interface as a model system, we were able to grow Co-oxide and Ti-oxide nanoclusters for their possible application in photocatalysis. We successfully determined the surface chemical states (in both Co-oxide and Ti-oxide nanoclusters) using spectroscopic technique and microscopic technique (for Co-oxide nanoclusters) for morphology and cluster size determination. We performed a series of photocatalytic experiments on both these systems. We didn't get the desired results in case of Co-oxide nanoclusters and failure could be attributed to number of factors like the particle size and surface oxygen species which highly effects the catalytic activity of such systems. On other hand, we get very encouraging results for Ti-oxide nanoclusters where the titania-Gr interfaces are 20 times more active toward clean hydrogen production as compared to the ones without Gr and it is related to the fact that Gr is playing well its role as a buffer layer. Beside this, we also studied the dehydrogenation mechanism of large organic molecules like coronene on Ir(111) which could be translated to create new materials to get control over surface structure and chemical composition (conformationally controlled chemical reactions) for more efficient catalytic systems in nano-catalysis. Further, we have exploited the natural corrugation of Gr grown on Ir(111) for self assembly of Rh clusters. We found both theoretically and experimentally that at higher coverages of CO, the edges of Rh nanoclusters are the places where the adsorption of CO is preferred. The enhanced catalytic selectivity towards CO oxidation exhibited that these under coordinated atoms have displayed an important role in driving the chemical reactivity of supported nanoclusters. We hope that this study may help to improve the fundamental

properties of similar systems at nanoscale for their application in field of catalysis.

The work presented in this thesis illustrates well the capabilities of the synchrotron based technique for studying properties of different metal nanoclusters supported on Gr/Ir(111) interface and augmented further with DFT calculations. The present work may leave some open questions besides providing new insight into these materials. So the future prospectives in this regards (specially in case Ti-oxide nanoclusters) includes, firstly, to prepare same architectures and find the activity over the period of time and also compare it with other architecture and see how its effecting photocatalysis for comparison as in two cases the doping of Gr is different and secondly, extend the characterization to the cluster size, morphology and growth mechanism in order to better understand Ti-oxide cluster activity towards clean hydrogen production.

Publications

- F. Presel, **N. Jabeen**, M. Pozzo, D. Curcio, L. Omiciuolo, P. Lacovig, S. Lizzit, D. Alfè, and A. Baraldi. *Unravelling the roles of surface chemical composition and geometry for the graphene-metal interaction through C1s core-level spectroscopy.* Carbon 93:187, (2015).

- D. Curcio, L. Omiciuolo, M. Pozzo, P. Lacovig, S. Lizzit, **N. Jabeen**, L. Petaccia, D. Alfè, and A. Baraldi. *Molecular lifting, twisting, and curling during metal-assisted polycyclic hydrocarbon dehydrogenation.* Journal of the American Chemical Society, 138:3402, (2016).

Other Publications:

- D. Curcio, L. Omiciuolo, M. Pozzo, P. Lacovig, S. Lizzit, **N. Jabeen**, L. Petaccia, D. Alfè, and A. Baraldi. *Molecular lifting, twisting, and curling during metal-assisted polycyclic hydrocarbon dehydrogenation.* Elettra Highlights, 56-57, 2015-2016.

Acknowledgements

Finally, my PhD thesis comes to an end. It would never be possible without the support of number of people who have helped me out to achieve this goal.

First of all, I would like to pay my sincere gratitude to my supervisor Prof. Alessandro Baraldi. His unconditional support, guidance, encouragement and dedication to research work remained the key sources of inspiration throughout my research work. Initially, being a foreign student, it was difficult for me to synchronize myself with the area of research but your kind support and encouragement motivated me to continue it till completion.

I am thankful to Silvano Lizzit and Paolo Lacovig, for their support and help in the experimentation and data analysis at the SuperESCA beam line. I also want to thank Nanospectroscopy and BaDElPh beamline group for their support in the experiments. I am deeply thankful to Onur Menteş from the Nanospectroscopy beam line for all his valuable time spent discussing the data analysis and Dario Alfè at the UCL for his contributions with state-of-the-art DFT calculations.

I would like to thank all my colleagues working at Elettra and surface science laboratory, particularly: Crisitian, Davide, Dario, Elisabetta, Francesco, Harsh, Luca for interactive sharing of knowledge and technical skills.

The support of my family cannot be ignored at this moment specially my husband, daughter and parents. Without their cooperation in managing things, it would have been very difficult for me to complete my research work.

The research activity cannot be carried out without funding. I would like to appreciate the role of ICTP for providing scholarship to my research activities. I would also like to say special thanks to Prof. Lucia Pasquato for her kind support through out these three years and the graduate school of nanotechnology in fulfilling my dream of completing PhD at University of Trieste.